Flow boiling of CO$_2$ in porous structures

Sonja Haertlé

Flow boiling of CO$_2$
in porous structures

Zur Erlangung des akademischen Grades einer

Doktorin der Ingenieurwissenschaften (Dr.-Ing.)

von der KIT-Fakultät für Chemieingenieurwesen und Verfahrenstechnik des
Karlsruher Instituts für Technologie (KIT)

genehmigte

Dissertation

von

M. Sc. Sonja Maria Haertlé
geb. Weise

aus Füssen

Tag der mündlichen Prüfung: 22. September 2022
Erstgutachter: Prof. Dr.-Ing. Thomas Wetzel
Zweitgutachter: Prof. Dr. Klaus Spindler

Vorwort

Die nachfolgende Arbeit entstand im Rahmen meiner Tätigkeit als wissenschaftliche Mitarbeiterin am Institut für Thermische Verfahrenstechnik (TVT) des Karlsruher Instituts für Technologie (KIT).

Ein besonderer Dank gilt meinem Doktorvater, Prof. Dr.-Ing. Thomas Wetzel, für die Ermöglichung dieser Arbeit und der dazugehörigen Projekte, für sein Vertrauen in meine Arbeit sowie die stete inhaltliche und motivierende Unterstützung. Prof. Dr.-Ing. Klaus Spindler danke ich für die Übernahme des Korreferats, sein Interesse an meiner Arbeit auf zahlreichen Konferenzen und die akribische Durchsicht meiner Promotionsschrift. Dr.-Ing. Benjamin Dietrich möchte ich für die thematische Betreuung der Arbeit danken. Herrn Dr. Drögemüller von der Firma CALGAVIN Ltd. danke ich für die Überlassung der Drahtmatrixelemente sowie zahlreiche Diskussionen.

Danken möchte ich auch besonders meinen Bürokollegen für die schönen, lustigen, diskussionsintensiven Jahre und allen Kollegen für die schöne gemeinsame Zeit am TVT. Auch meinem Vorgänger und und meinem Nachfolger möchte ich besonders danken für die wertvollen Diskussionen und die Unterstützung auch über die Arbeitszeit hinaus. Allen, die die nachfolgende Arbeit Korrektur lasen und mit ihren wertvollen Anmerkungen zum Feinschliff beitrugen. Den Mitarbeitern der Werkstatt für die Unterstützung beim Umbau und zahlreichen Reparaturen der Versuchsanlage. Allen Mitarbeitenden in Sekretariat, Labor, technischem Büro sowie den Reinigungskräften für die Schaffung einer angenehmen Arbeitsatmosphäre und die Übernahme von administrativen Tätigkeiten. Meinen Masterarbeiter:innen, Bachelorarbeiter:innen, Praktikanten und Praktikantinnen, sowie wissenschaftlichen Hilfskräften für ihre Unterstützung, ihr großes Engagement und zahlreiche Diskussionen.

i

Mein ganz besonderer Dank gilt meiner Familie, die mir durch ihre Liebe und Unterstützung diese Promotion ermöglicht hat. Meine Eltern gaben mir das Selbstvertrauen, mein Mann den nötigen Rückhalt und die Zeit und meine Kinder den Blick fürs Wesentliche.

Eppelheim, November 2022

Sonja Haertlé

Kurzfassung

Um die Vorteile der Integration poröser Strukturen in Verdampferrohre zu bewerten und somit effiziente Wärmeübertrager zu entwerfen, sind zuverlässige Vorhersagemodelle für Wärmeübergang und Druckverlust erforderlich. Angesichts der großen Zahl und Komplexität möglicher Einsätze ist eine Vorhersage auf Basis eines universellen Modells, welches auf nicht experimentell untersuchte Einsätze übertragen werden kann, von großem Wert. Lediglich Modelle, die auf etablierten Beziehungen beruhen und keine Anpassungsparameter benötigen, können aufgrund der bislang kleinen Datenbasis für Strömungssieden in Rohren mit Einsätzen dieses Kriterium erfüllen. Ziel dieser Arbeit war es daher, die folgende Hypothese zu verifizieren oder zu falsifizieren:

Der Wärmeübergang und der Druckverlust beim Strömungssieden in einem horizontalen Rohr mit porösen Einbauten können durch physikalisch sinnvolle Kombination von etablierten Modellen aus den Bereichen „Einphasenströmung" und „Sieden in Leerrohren" beschrieben werden - ohne die Verwendung von Anpassungsparametern.

Daher wurden Druckverlust- und Wärmeübertragungsversuche mit drei verschiedenen porösen Einsätzen an der Strömungssiedeversuchsanlage des Instituts für Thermische Verfahrenstechnik (Karlsruher Institut für Technologie, KIT) unter Verwendung einer neu konstruierten Versuchsstrecke durchgeführt. Die horizontale Versuchsstrecke (Innendurchmesser 14 mm) misst den umfangsaufgelösten Wärmeübergangskoeffizienten bei konstanter Wandtemperatur. Ein Schauglas kombiniert mit einer Hochgeschwindigkeitskamera ermöglicht die Beobachtung der Phasenverteilung der untersuchten Zweiphasenströmung. Untersucht wurden zwei Schwammeinsätze (auch offenzellige Schäume genannt) mit unterschiedlichen Zellgrößen sowie ein Drahtmatrixelement. Die realisierten Betriebsbedingungen umfassen Sättigungsdrücke von 1,2 MPa bis 2,65 MPa (entsprechend Sättigungstemperaturen zwischen -35 °C und -10 °C und reduzierten Drücken zwischen 0,16 und 0,36), Massenströme von 25 kg m^{-2} s^{-1} bis 200 kg m^{-2} s^{-1}, Strömungsdampfgehalten von 5% bis 98% und einer Wandüberhitzung von bis zu 7 K. Als Versuchsflüssigkeit wurde CO_2 gewählt.

Der Druckverlust der Zweiphasenströmung in einem Rohr mit porösen Einsätzen wurde unter adiabatischen und diabatischen Bedingungen untersucht. Bei hohen Massenstromdichten konnte ein Modell entwickelt werden, welches auf einer Anpassung des quadratischen Forchheimer-Terms an eine Zweiphasenströmung nach dem homogenen Modellansatz beruht. Hiermit lassen sich mehr als 88% aller experimentellen Daten für einen bestimmten Einsatz mit einem absoluten prozentualen Fehler von weniger als 30% beschreiben. Für diabatische Bedingungen unterschätzt das homogene Leerrohrmodell die auf Beheizung zurückzuführende Komponente des Druckverlustes. Je größer der adiabate Druckverlust, desto höher ist auch dieser zusätzliche Druckverlust aufgrund einer Beheizung der Teststrecke.

Der Wärmeübergangskoeffizient wurde lokal ausgewertet und mit dem Wärmeübergangskoeffizient in leeren Rohren sowie etablierten Modellen und Konzepten (unter anderem aus Kattan et al. [1], Weise et al. [2] und Lu und Zhao [3]) verglichen. Während die Einsätze den Beitrag des Blasensiedens zum Wärmeübergang beim Strömungssieden kaum zu beeinflussen scheinen, erhöhen sie den Beitrag des konvektiven Siedens. Daher ist eine Beschreibung des Blasensieden-Anteils mittels des auch fürs Leerrohr geeigneten Modells möglich. Im konkreten Fall ist dies die Gleichung von Cooper [4], wie Weise et al. [2] zeigten. Den konvektiven Beitrag beschreiben an die Zweiphasenströmung angepasste Modelle des einphasigen Wärmeübergangs an einer Rohrwand mit den jeweiligen Einbauten. Bei Schwammeinbauten ist dies beispielsweise das Modell von Bianchi et al. [5] kombiniert mit einer Zweiphasen-Reynoldszahl. Auf der Grundlage dieser Beobachtungen wurde ein Modell entwickelt, das mehr als 90% aller Daten mit einem Fehler von weniger als 30% beschreibt. Für dieses Modell ist kein Anpassungsfaktor erforderlich.

Die Hypothese kann folglich für die Modellierung des adiabaten Druckverlusts bei hohen Massenstromdichten sowie für die Modellierung des Wärmeübergangskoeffizienten im untersuchten Parameterbereich verifiziert werden. Da die entwickelten Modelle auf etablierten Konzepten beruhen und auf die Verwendung von Anpassungsparametern verzichten, kann eine Übertragbarkeit auf andere poröse Strukturen, Rohrdurchmesser, Kältemittel und Betriebsbedingungen erwartet werden.

Abstract

To evaluate the advantages of integrating porous structures into evaporator tubes and thus design efficient heat exchangers, reliable predictive models for heat transfer and pressure drop are required. Given the large number and complexity of possible inserts, a prediction based on a universal model that can be applied to inserts, which were not investigated experimentally, is of great value. Most of the models suggested in literature require fitting parameters to adapt them to measurement data. Only models that rely on established relationships and do not need fitting parameters can fulfill this criterion due to the small data base to date. Consequently, the aim of this thesis was to verify or falsify the following hypothesis:

The heat transfer and pressure drop of flow boiling in a horizontal tube with porous inserts can be described by physically reasonable combination of established models from the fields of "single-phase flow" and "boiling in empty tubes" - without using fitting parameters.

Consequently, pressure drop and heat transfer tests with three different porous inserts were carried out at the flow boiling test facility at the Institute of Thermal Process Engineering (Karlsruhe Institute of Technology, KIT) using a newly designed test section. The horizontal test section (inner diameter 14 mm) measures the circumferentially resolved heat transfer coefficient at constant wall temperature. A sight glass combined with a high-speed camera enables the observation of the phase distribution of the investigated two-phase flow. Two sponge inserts (also called open-cell foam inserts) with different cell sizes and a wire matrix element were investigated. The realized operating conditions include saturation pressures from 1.2 MPa to 2.65 MPa (corresponding to saturation temperatures between -35 °C and -10 °C and to reduced pressures between 0.16 and 0.36), mass fluxes from 25 kg m^{-2} s^{-1} to 200 kg m^{-2} s^{-1}, vapor qualities from 5% to 98%, and a wall superheat of up to 7 K. CO_2 was chosen as the experimental fluid.

The pressure drop of the two-phase flow in a tube with porous inserts was investigated under adiabatic and diabatic conditions. At high mass fluxes, it was possible to develop a model based on an adaption of the quadratic Forchheimer term to two-phase flow using the homogeneous model approach. This allows more than 88% of all experimental data for a specific insert to be described with an absolute percentage error of less than 30%. For diabatic conditions, however, the homogeneous empty tube model underestimates the component of pressure drop due to heating. The larger the adiabatic pressure drop, the higher is this additional pressure drop due to heating of the test section.

The heat transfer coefficient was evaluated locally and compared to the heat transfer coefficient in empty tubes as well as established models (among others, from Kattan et al. [1], Weise et al. [2] and Lu and Zhao [3]). While inserts barely seem to influence the nucleate boiling contribution of the flow boiling heat transfer of completely wetted segments, they enhance the convective boiling contribution. Therefore, a description of the nucleate boiling contribution is possible using the model which is also suitable for the empty tube. In the specific case, this is Cooper's equation [4], as shown by Weise et al. [2]. The convective contribution is described by models adapted to the two-phase flow, which describe the single-phase heat transfer at the tube wall with the respective inserts. For sponge inserts, for example, this is the model of Bianchi et al. [5] combined with a two-phase Reynolds number. Based on these observations, a model was developed that describes more than 90% of all data with an error of less than 30%. No fitting parameter is required for this model.

Consequently, the hypothesis can be verified for the modeling of the adiabatic pressure drop at high mass fluxes as well as for the modeling of the heat transfer coefficient in the investigated parameter range. Since the developed models are based on established concepts and do not use fitting parameters, transferability to other porous structures, tube diameters, cooling media and operating conditions can be expected.

Contents

List of abbreviations and symbols

Latin symbols

A	area	m^2
$a_0, a_1, a_2,$	coefficients	
C	coefficient	
C_0	distribution parameter (Rouhani drift-flux model)	
c	speed of sound	m s^{-1}
c_F	form drag coefficient	
c_p	specific heat capacity at constant pressure	J kg^{-1} K^{-1}
c_v	specific heat capacity at constant volume	J kg^{-1} K^{-1}
D_i	tube inner diameter	m
d	characteristic diameter (of porous structure)	m
d_c	cell diameter	m
d_h	hydraulic diameter	m
d_s	strut diameter	m
d_w	window diameter	m
f_{dry}	dry fraction	
f	Fanning friction factor	
f	function	
g	gravitational acceleration	m s^{-2}
h	specific enthalpy	J kg^{-1}
i	index variable for measurement plane	
j	index variable for segment	
K_{diss}	power dissipation factor	

List of abbreviations and symbols

K	Darcy permeability	m^2
k	coverage factor	
kA	thermal transmittance	$W\ K^{-1}$
L	characteristic length	m
L_h	heated length of the test section	m
L_p	distance between the pressure taps	m
$\dot{M}$	mass flow rate	$kg\ s^{-1}$
$\widetilde{M}$	molar mass	$kg\ mol^{-1}$
m	exponent, parameter	
$\dot{m}$	mass flux related to the cross section occupied by liquid and vapor (interstitial mass flux)	$kg\ m^{-2}\ s^{-1}$
$\dot{m}_0$	mass flux with respect to the cross-sectional area of the tube (superficial mass flux)	$kg\ m^{-2}\ s^{-1}$
n	parameter	
n	number of frames	
P	power	W
P	pixel	
$\bar{P}$	arithmetic mean of pixels with respect to time	
p	pressure	Pa
p_r	reduced pressure	
$\dot{Q}$	heat transfer rate	W
$\dot{q}$	heat flux	$W\ m^{-2}$
$\dot{q}^*$	average heat flux related to tube surface area between pressure taps	$W\ m^{-2}$
R_A	mean arithmetic surface roughness	m
S_v	(geometric) specific surface area	m^{-1}
s_x	standard deviation	
s	standard deviation of the mean	

T	temperature	K
t	time	s
u	velocity	m s^{-1}
u_{Vm}	drift-flux velocity of the vapor phase	m s^{-1}
V	volume	m^3
x	coordinate	
$\dot{x}$	vapor quality	%
Y_1	abbreviation for $Nu_{\mathrm{cb,exp}} \cdot Pr^{-0.4}$	
y	coordinate	
z	axial direction of tube	

Greek symbols

α	heat transfer coefficient	W m^{-2} K^{-1}
β	Forchheimer coefficient	m^{-1}
Δh_{LV}	specific enthalpy of vaporization	J kg^{-1}
Δp	pressure difference	Pa
δ	film thickness	m
ε	void fraction	
γ	isentropic expansion factor, c_p/c_v	
θ_j	angle of one segment (60° for the test section used)	rad, °
θ_{dry}	dry angle of tube perimeter	rad, °
$\theta_{\mathrm{dry,s}}$	dry angle of equivalent stratified flow	rad, °
ϑ	temperature	°C
κ	thermal diffusivity	m^2 s^{-1}
λ	thermal conductivity	W m^{-1} K^{-1}
μ	dynamic viscosity	Pa s

$\bar{\mu}$	homogeneous dynamic viscosity	Pa s
ν	kinematic viscosity	$m^2\,s^{-1}$
ξ	friction factor for turbulent flow in tubes	
ρ	density	$kg\,m^{-3}$
$\bar{\rho}$	homogeneous density	$kg\,m^{-3}$
ρ_m	momentum density	$kg\,m^{-3}$
σ	standard deviation	
σ	surface tension	$N\,m^{-1}$
τ_W	wall shear stress	$N\,m^{-1}$
τ	tortuosity, geometric factor	
Φ	two-phase multiplier	
φ	angle describing the azimuthal position of the thermo-couple tips	°
ψ	porosity	%
ψ_o	open porosity (accessible to a fluid flow)	%
Ω	correction function for pressure drop	

Subscripts, superscripts and abbreviations

APE	absolute percentage error
a	annular
acc	acceleration
bc	boundary condition
calc	calculated
cb	convective boiling
CO_2	carbon dioxide
Cu	copper

cw	completely wetted
D-F	Darcy-Forchheimer
DNB	departure from nucleate boiling
d	dryout
dry	dry perimeter
δ	film thickness
e	entrance
el	electric
eq	equilibrium
et	empty tube
exp	experimental, fitted to experiments
F	Forchheimer
fr	frictional
h	heated region, related to heat transfer measurement
hom	homogeneous
i	index variable for measurement plane
i	intermittent (slug/plug)
in	instationary
in	at the entrance, inner
ins	insulation
j	index variable for segment
L	liquid phase
La	liquid-all (as if the total flow is liquid)
L-M	Lockhart-Martinelli
Lo	liquid-only (as if the liquid fraction would flow alone)
LV	vaporization
L+V	liquid and vapor phase

L,V	at the interface of liquid and vapor
MAPE	mean absolute percentage error
MPE	mean percentage error
m	pseudo single fluid (drift-flux model)
m	mist
min	minimal
mp	measurement plane
nb	nucleate boiling
ONB	onset of nucleate boiling
o	open
out	at the outlet, outer
P	parasitic
p	related to pressure measurement
pe	pre-evaporator
pm	porous medium
ppi	pores per inch
pred	predicted
pw	partially wetted
st	strut
s	stratified
s*	distracted stratified flow
sep	separated
sp	single-phase flow
st	stationary
tc	thermocouple
tp	two-phase
ts	test section

V	vapor phase
Va	vapor-all (as if the total flow is vaporous)
Vo	vapor-only (as if the vapor fraction would flow alone)
W	wall
w	window
w	(stratified) wavy
wme	wire matrix element

Dimensionless numbers

Fo	Forchheimer number; $Fo = \sqrt{K} \cdot c_\mathrm{F} \cdot \dot{m}_0 \cdot \mu^{-1}$
Ma	Mach number; $Ma = u \cdot c^{-1} = \dot{m} \cdot \rho^{-1} \cdot c^{-1}$
Nu	Nusselt number; $Nu = \alpha \cdot L \cdot \lambda^{-1}$
Pe	Péclet number; $Pe = Re \cdot Pr$
Pr	Prandtl number; $Pr = c_p \cdot \mu \cdot \lambda^{-1}$
Re	Reynolds number; various definitions

1   Introduction

Problem definition

Optimized heat transfer and pressure drop results in more compact and cost-effective heat exchangers, including evaporators, or reduced operating costs [6]. The integration of porous structures into horizontal evaporator tubes can help to enhance the efficiency of the evaporation process. Several researchers have reported an increased heat transfer in evaporator tubes with porous inserts, such as sponges (open-cell foams) or wire matrix elements, compared to empty tubes [7–13]. However, porous inserts also increase the pressure drop. Therefore, reliable predictive models for both heat transfer and pressure drop are required to evaluate the benefits of integrating porous structures into evaporator tubes and to design efficient heat exchangers.

So far, some geometry-specific models have been suggested in the literature to describe the heat transfer [3,14–17] and the pressure drop [15,18–23] in evaporator tubes with porous inserts. Most of these models require fitting parameters to adapt them to measurement data [14–17,20–22]. However, only models that rely on established relationships and do not need fitting parameters can be transferred to inserts or operating conditions other than experimentally tested. In view of the large number of possible inserts, a prediction based on such a universal model is of great value.

Hypothesis

Consequently, the aim of this thesis is to test the following hypothesis:

The heat transfer and pressure drop of flow boiling in a horizontal tube with porous inserts can be described by physically reasonable combination of established models from the fields of "single-phase flow" and "boiling in empty tubes" - without using fitting parameters.

The hypothesis is accepted if the proposed models can describe more than 80% of the experimental data with an absolute percentage error of less than 30% and can additionally explain observed trends and influencing mechanisms. The acceptance criterion is chosen because empty-tube data from the same test facility [24] can at best be described with this quality using a correlation known to date that has not been explicitly fitted to the data [2,24].

Approach

First, laws describing the heat transfer and pressure drop of single-phase flow in porous media and two-phase flow in empty tubes are assessed regarding their use in model combinations for which no fitting parameters are necessary. Then, the state of the art of modeling flow boiling heat transfer and pressure drop in horizontal tubes with porous inserts is presented. In this regard, possible factors influencing heat transfer and pressure drop of two-phase flow in porous media are examined.
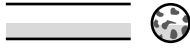
Subsequently, experiments are designed to provide insight into the physical relations during flow boiling. For this purpose, a special test section is developed and tests with three different inserts are carried out.

Based on the investigation of the influencing factors, models are derived that meet the criteria of the hypothesis. These models are compared with the experimental results to determine the limits of the prediction and develop suggestions for improvement.

2 State-of-the-art

The modeling of heat transfer and pressure drop of two-phase flow in horizontal tubes with porous inserts contains some levels of complexity. Possible concepts of such modeling are summarized in Table 2.1. The laws of two-phase flow in tubes with porous inserts can have similarities with single-phase flow in a tube with porous inserts but also with single- or two-phase flow in empty tubes. The understanding of these relatively well investigated, yet complex subjects is of great importance for gaining systematic insight into two-phase flow in tubes with porous inserts. Thus, the relevant findings of two-phase flow in empty tubes and single-phase flow in tubes with porous inserts are explained first in the following. Subsequently, the two-phase flow in tubes with porous inserts will be discussed.

Table 2.1: Overview of topics for modeling two-phase flow in tubes with porous inserts. The chapters in which the individual topics are explained in detail are indicated in parentheses.

	single-phase flow (sp)	two-phase flow (tp)
empty tube (et)	 • pressure drop • heat transfer	 • homogeneous model versus separated flow models (2.2) • pressure drop (2.3.2) • flow pattern (2.4.1) • flow boiling heat transfer (2.5.1)
tube with porous inserts (pm)	 • insert type and definition of geometry (2.1) • inserts versus fins (2.1) • superficial versus phase velocity (2.1) • pressure drop (2.3.1) • heat transfer (especially at wall) (2.5.2)	 • pressure drop (2.3.3) • flow pattern (2.4.2) • flow boiling heat transfer (2.5.3)

2.1 Porous inserts

Wire matrix elements and sponges are **porous structures** that are proposed to improve the efficiency of single-phase and multi-phase flow in tubes [7–11]. In this thesis, flow boiling in two types of solid sponges and a wire matrix element is investigated. These structures share a continuous solid phase and a continuous void phase. Both phases are regularly or irregularly spaced over the entire tube cross section. Twisted tapes and wire coils have structural similarities to these porous structures, but are not comparably spaced over the tube cross section. However, observations and concepts developed for twisted tapes and wire coils are potentially transferable and are thus included in the literature review if applicable. Figure 2.1 illustrates the different types of inserts.
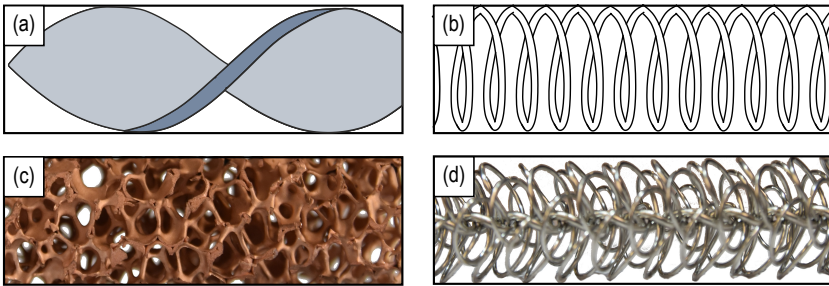
Figure 2.1: Different insert types for multi-phase flow in tubes: (a) twisted tapes, (b) wire coils, (c) sponges, and (d) wire matrix elements.

Twisted tapes, wire coils, and wire matrix elements are usually not bonded to the inner tube walls of heat exchangers. Contrary, some authors report of sponges that are soldered to the tube wall. For differentiation, porous structures that are bonded to the tube wall are referred to as **'porous fins'** in this thesis. Structures that are inserted loosely or with force fit are called **'porous inserts'**. Fins can provide an additional heat transfer path – heat conduction through the solid. For the pressure drop under adiabatic condition, it is irrelevant whether the structure is bonded to the wall or not in case the gap between the tube wall and the insert is small compared to a characteristic structural part of the insert adjacent to the wall. Thus, concepts and model approaches can be transferred

from fins to inserts after the evaluation of the influence of a substance-to-substance bond.

Solid sponges (also called open-cell foams) consist of a continuous, irregular network of struts and nodes. These struts and nodes form windows that enclose individual cells of the sponge (see Figure 2.2 (a)). Solid sponges can be made from metal or ceramics by various methods [25,26]. The manufacturing method influences the strut geometry. Struts of sponges produced by means of replication techniques are hollow (see micrograph Figure 2.2 (b)). In contrast, the struts of sponges fabricated by investment casting or additive manufacturing are filled to only a few voids, e.g., casting defects (see micrograph Figure 2.2 (c)). The geometry of a sponge is typically characterized by its porosity and cell density. Especially for sponges made by replication techniques, one should distinguish between total porosity, ψ, and open porosity, ψ_o. In contrast to the open porosity, the total porosity also includes small pores in the struts that are not accessible to a fluid flowing through the sponge [27–29]. In this work, the cell density is determined according to ASTM D3576 [30], counting the number of pores per inch (ppi). No distinction is made between cell windows and complete cells. Thus, this measure should not be used in correlations. More precise alternatives to the cell density are the cell diameter, d_c, the window diameter, d_w, the strut diameter, d_{st} (see Figure 2.2 (a)).
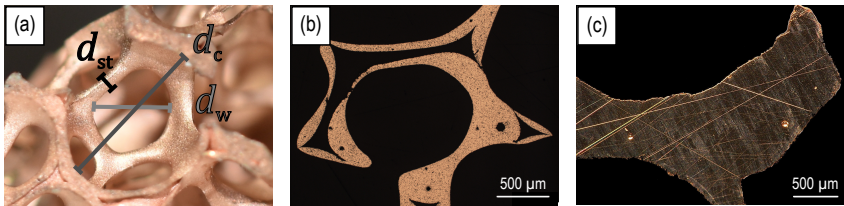
Figure 2.2: (a) Microscopic photograph of a sponge cell. The cell diameter, d_c, the window diameter, d_w, and the strut diameter, d_{st}, are displayed. (b) Micrograph of a sponge made by replication technique [31]. (c) Micrograph of a sponge strut made by investment casting [32].

Wire matrix elements consist of twisted wires in the core with loops inserted at equidistant windings [9]. Due to the springiness of these loops, the diameter of the wire matrix element in the uninstalled state is slightly larger than the

inner diameter of the tube. This ensures that the loops touch the wall [9]. The wire matrix elements can be made from most materials in which wire is available, typically stainless steel [33]. The number of loops per unit length [9], wire diameter [9], loop angle [9], and tube diameter for which the wire matrix element is designed [33] can be varied during the manufacturing process.

2.2 Basics of two-phase flow

For modeling the transport properties of two-phase flows, three fundamentally different approaches can be distinguished (compare Figure 2.3). The models differ in the assumption of the phase distribution and thus in the description of the velocity, the pressure, the density, and the shear stress at the wall or, if applicable, at the liquid-vapor interface.

The **homogeneous approach** assumes that the velocity of the gas phase corresponds to the velocity of the liquid phase and that liquid and gas phase have mixing properties. In contrast, separated models, such as the drift-flux model and the two-fluid model, account for different transport and state properties for the fluid phases. The **drift-flux model** considers the vapor and liquid phases as a pseudo-single fluid, but permits a slip between the two phases. The slip and the phase distribution over the cross section are modeled by empirical equations [34]. In the **two-fluid model**, both phases flow with different velocities in their respective cross sections. The pressure and the temperature of the respective phases may differ; however, the temperature is often considered to be constant within the tube cross section (thermodynamic equilibrium). Empirical models are used to model the shear stresses at the wall and at the interface [35].

| homogeneous model | drift-flux model | two-fluid model |
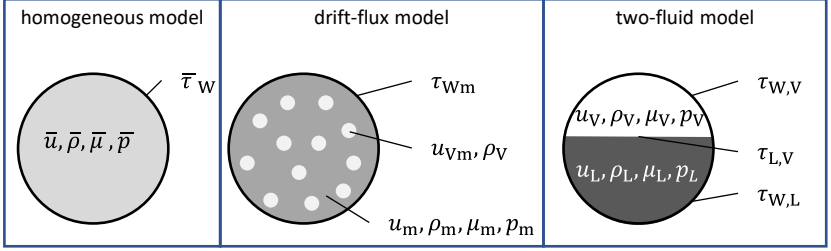
Figure 2.3: Illustration of two-phase flow model approaches exemplified for the continuity and momentum equation. p: pressure; u: velocity; μ: viscosity; ρ: density; τ: shear stress; $^-$: homogeneous; L: liquid; m: pseudo single fluid; V: vapor, W: wall.

Important transport and state properties of a two-phase flow through porous media are defined below. The **total mass flux, $\dot{m}$**, equals the mass flow rate of the liquid and the vapor, $\dot{M}$, related to the cross section occupied by liquid and vapor, A_{L+V}, see Eq. (2.1). In porous media, this corresponds to the average intrinsic mass flux. In tubes with inserts, in accordance with the concept of superficial velocity, the total mass flow rate, $\dot{M}$, is often related to the cross-sectional area of the tube, A, resulting in the measure $\dot{m}_0$. In empty tubes, these two measures are equivalent due to the porosity, $\psi_o = 1$.

$$\dot{m} = \frac{\dot{M}}{A_{L+V}} = \frac{\dot{M}}{\psi_0 \cdot A} = \frac{\dot{m}_0}{\psi_o} \tag{2.1}$$

The average **void fraction**, ε, is defined by Eq. (2.2) as the time-averaged cross-sectional area occupied by vapor divided by the cross-sectional area occupied by vapor and liquid [36].

$$\varepsilon = \frac{A_V}{A_{L+V}} \tag{2.2}$$

The **vapor quality**, $\dot{x}$, is the local vapor mass flow rate, $\dot{M}_V$, divided by the local total mass flow rate [36], $\dot{M}$, see Eq. (2.3). In contrast to the void fraction, the vapor quality can be determined experimentally by means of an enthalpy balance.

$$\dot{x} = \frac{\dot{M}_V}{\dot{M}} \tag{2.3}$$

The **relation between the vapor quality and the void fraction** is of main importance for many models describing the pressure drop, the flow pattern, and the heat transfer coefficient. In the literature a plethora of correlations are proposed for this relation. Overviews of these and comparisons with experimental data have been given by Woldesemayat and Ghajar [37] and by Cioncolini and Thome [38], among others. Two models, i.e., the homogeneous model and the Rouhani drift-flux model, used within the scope of this work are presented here.

Assuming **homogeneous flow**, the vapor quality and the void fraction are related by Eq. (2.4) [36]. The mean density, also called homogeneous density, $\bar{\rho}$, is calculated by Eq. (2.5) [36].

$$\varepsilon = \dot{x} \cdot \frac{\bar{\rho}}{\rho_{\mathrm{V}}} \qquad (2.4)$$

$$\bar{\rho} = \varepsilon \cdot \rho_{\mathrm{V}} + (1 - \varepsilon) \cdot \rho_{\mathrm{L}} = \left(\frac{\dot{x}}{\rho_{\mathrm{V}}} + \frac{1 - \dot{x}}{\rho_{\mathrm{L}}} \right)^{-1} \qquad (2.5)$$

Steiner [39] proposed to use the **Rouhani drift-flux model** ([40] apud [39]) defined by Eq. (2.6), which is based on work by Zuber and Findlay [41].

$$\varepsilon = \frac{\dot{x}}{\rho_{\mathrm{V}}} \left[C_0 \cdot \bar{\rho} + \frac{(1 - \dot{x})}{\dot{m}} \cdot \frac{\langle \varepsilon\, u_{\mathrm{Vm}} \rangle}{\langle \varepsilon \rangle} \right]^{-1} \text{ with} \qquad (2.6)$$

$$C_0 = [1 + 0.12 \cdot (1 - \dot{x})];$$

$$\frac{\langle \varepsilon\, u_{\mathrm{Vm}} \rangle}{\langle \varepsilon \rangle} = \frac{1.18 \cdot [\sigma \cdot g(\rho_{\mathrm{L}} - \rho_{\mathrm{V}})]^{0.25}}{\rho_{\mathrm{L}}^{0.5}}$$

The distribution parameter C_0 considers the distribution of the void fraction and the average velocity over the tube cross section. If the local void fraction in the tube center is larger than at the tube wall, then $C_0 > 1$. The model used for the drift-flux velocity, u_{Vm}, in $\langle \varepsilon\, u_{\mathrm{Vm}} \rangle / \langle \varepsilon \rangle$ is the terminal velocity of a bubble rising in an infinite turbulent medium [41]. Nevertheless, the Rouhani drift-flux model is often used in heat transfer models for horizontal smooth

tubes [1,42] as well as for heat transfer and pressure drop models in tubes with inserts [43,44] regardless of the flow pattern.

Figure 2.4 compares the homogeneous void fraction model and the Rouhani drift-flux model exemplified at two different saturation pressures for the refrigerant CO_2. The void fraction calculated by Rouhani's model is smaller than the void fraction determined by the homogeneous model because the vapor phase tends to be faster than the liquid phase in separated flow. Moreover, the void fraction depends on the mass flux if the Rouhani model is used. The sensitivity of the model towards a change in mass flux is the more pronounced the lower the mass flux is.
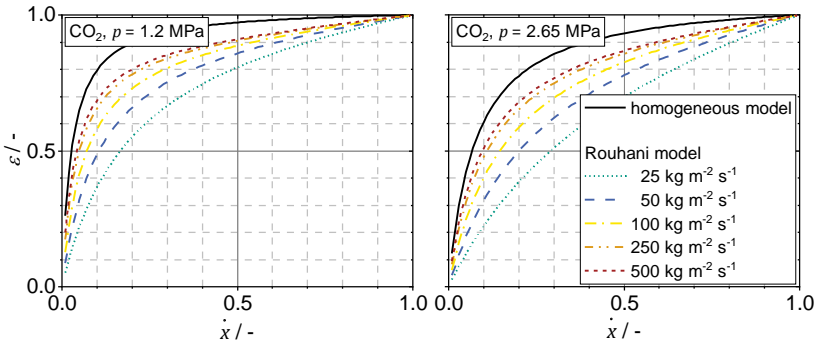
Figure 2.4: Comparison of the homogeneous void fraction model according to Eq. (2.4) and the Rouhani void fraction model [40] according to Eq. (2.6) as a function of saturation pressure and (intrinsic) mass flux, $\dot{m}$, for CO_2 at saturation conditions.

2.3   Pressure gradient

Here, the term pressure gradient refers as short version to the gradient of the scalar static pressure field. This quantity cannot be measured directly, but can only be approximated by the pressure drop, i.e. the difference between the static pressure at two different tube cross sections. [45]

There are two approaches to understanding the pressure gradient of two-phase flows in porous inserts: Either one thinks of a two-phase flow in an empty tube and superimposes the effect of the inserts or one starts with a single-phase flow in porous inserts and superimposes the effects of the two-phase flow. Consequently, the basics of two-phase flow in empty tubes and single-phase flow in inserts are briefly discussed before summarizing the literature on two-phase flow in tubes with porous inserts. These topics were discussed in detail in a previous paper [23] and are summarized below. Figure 2.5 concludes by summarizing the model approaches and dependencies for the frictional component of the two-phase pressure gradient in tubes with porous inserts.

2.3.1 Single-phase pressure gradient in tubes with porous inserts

The pressure gradient in tubes with porous inserts is increased compared to the empty tube due an increased surface area, i.e., an increased skin friction resistance, and an additional form resistance.

To model the single-phase pressure gradient in tubes with inserts, two different approaches are conceivable: a) the multiplication of the empty-tube pressure gradient correlation with a penalty factor, which depends on geometric properties, fluid properties, and operating conditions [46], and b) the use of a model developed explicitly for porous inserts [47] (compare Figure 2.5). Both concepts can be combined with the use of a hydraulic diameter. However, the use of the so-called hydraulic diameter concept alone, just like for tubes with other geometries is not generally applicable because it does not account for obstacles and the increased effective flow length.

While approach a) is commonly used for twisted-tape inserts [46] and coiled-wire inserts [48], Nield and Bejan [47] recommend Eq. (2.7) to describe the single-phase (sp) pressure gradient of a stationary, incompressible flow through a homogeneous and isotropic porous medium (pm). Strictly speaking, in contrast to a porous insert, a porous medium is not confined by a tube wall. The influence of a confining tube wall is therefore discussed below. Eq. (2.7) is commonly referred to as the Darcy-Forchheimer equation. For this work, it

is adapted to the usual notation for two-phase flows, i.e., the mass flux, $\dot{m}_0$, is used instead of the superficial velocity.

$$-\left(\frac{\mathrm{d}p}{\mathrm{d}z}\right)_{\text{pm,sp}} = \frac{\nu}{K} \cdot \dot{m}_0 + \beta \cdot \frac{1}{\rho}\,\dot{m}_0^2 \qquad (2.7)$$

Besides the mass flux, $\dot{m}$, the pressure gradient depends on the Darcy permeability, K, the Forchheimer coefficient, β, the fluid viscosity, ν, and the fluid density, ρ. The first term in Eq. (2.7) can be derived by formal volume averaging for incompressible fluids [49]. Since information is lost during the volume averaging process, the additional form drag due to solid obstacles is taken into account by adding the quadratic term [50].

According to Auriault [51], Eq. (2.7) is appropriate for describing flow not only in porous media, but also in porous inserts if the characteristic pore size is considerably smaller than the tube diameter, D. This is usually not the case for applications in the field of flow boiling, so that a tube wall confining the porous structure could influence the total pressure gradient. This influence could be taken into account either by including an additional term in Eq. (2.7) [52] or by multiplying the Forchheimer coefficient by an attenuation factor [53]. However, the magnitude of the influence of a confining wall has not yet been clarified and therefore the manipulation of the Darcy-Forchheimer equation is controversial. In a previous work, no evidence of such wall influence was found for the two-phase flow in tubes with porous sponge inserts (compare Weise et al. [23]). Consequently, the influence of a confining wall is not considered in this thesis.

As outlined in the review articles by of Edouard et al. [54] and Kumar and Topin [55,56], there are numerous suggestions to predict the Darcy permeability and the Forchheimer coefficient on the basis of geometric properties. The contributions of Woudberg and Du Plessis [57], Inayat et al. [58], as well as Dietrich et al. [59] stand out from other correlations because of their physically stringent derivation and validation with a large database [23]. The main equations of these models are summarized in Table 2.2. Comparison of the models with two-phase experiments in a previous paper [23] suggests that the models by Woudberg and Du Plessis [57] or Inayat et al. [58], combined with a specific

surface measured by µCT scanning, best describe the Forchheimer coefficient, β, encountered in solid sponges.

Table 2.2:   Comparison of models predicting the Darcy permeability and the Forchheimer coefficient in analogy to a previous work [23].

	Dietrich et al. [59]	Woudberg et al. [57]	Inayat et al. [58]
Darcy permeability, K^{-1}	$\dfrac{110}{16} \cdot \dfrac{S_v^2}{\psi^3}$	$\dfrac{\tau^3}{(\tau - 1)} \cdot \dfrac{S_v^2}{\psi_0^3}$	$2 \cdot \tau^2 \cdot \dfrac{S_v^2}{\psi_0^3}$
Forchheimer coefficient, β	$1.45 \cdot \dfrac{S_v}{4 \cdot \psi^3}$	$\dfrac{\tau^2 \cdot c_d}{3} \cdot \dfrac{S_v}{4 \cdot \psi_0^3}$	$\dfrac{\tau^3}{2} \cdot \dfrac{S_v}{4 \cdot \psi_0^3}$
tortuosity / geometric factor, τ	constant	$2 + 2\cos\left[\dfrac{4\pi}{3} + \dfrac{1}{3}\cos^{-1}(2\psi_0 - 1)\right]$	$1 + \dfrac{d_w \cdot S_v}{4 \cdot \psi_0}$

2.3.2   Two-phase pressure gradient in empty tubes

The pressure gradient of a two-phase flow in a horizontal empty tube (et) is commonly approximated by its axial component assuming constant pressure over the tube cross section. The one-dimensional, first-order Taylor series approximation of the conservation of mass and momentum for steady-state flow conditions can be written as Eq. (2.8) using the momentum density, ρ_{m}, according to Eq. (2.9). [45].

$$-\left(\frac{\mathrm{d}p}{\mathrm{d}z}\right)_{\mathrm{tp,et}} = \frac{4\tau_{\mathrm{w}}}{D_{\mathrm{i}}} + \dot{m}^2 \frac{\mathrm{d}}{\mathrm{d}z}\left(\frac{1}{\rho_{\mathrm{m}}}\right) \tag{2.8}$$

$$\rho_{\mathrm{m}} = \left[\frac{\dot{x}^2}{\rho_{\mathrm{V}} \cdot \varepsilon} + \frac{(1 - \dot{x})^2}{\rho_{\mathrm{L}} \cdot (1 - \varepsilon)}\right]^{-1} \tag{2.9}$$

The first term on the right-hand side of Eq. (2.8) describes the **frictional component**, i.e. the fluid-wall interaction [45] as a function of the wall shear stress, τ_{w}, and the characteristic tube diameter, here the tube inner diameter, D_{i}. The dependence of the frictional component on the operating conditions was examined by Storek and Brauer [60] and are summarized in Figure 2.5 (upper right box). Most of the correlations suggested for the calculation of the fric-

tional component of the pressure gradient can be assigned to one of the following categories: 1) homogeneous models, 2) (semi-)empirical models with a two-phase multiplier and 3) (semi-)empirical models that superimpose single-phase liquid and single-phase vapor pressure drop (see upper two boxes in Figure 2.5). These three modeling approaches are briefly explained below.

In the **homogeneous modeling approach (1)** the frictional component is predicted according to Eq. (2.10) analogous to the single-phase correlation, but using the homogeneous density (Eq. (2.5)), a homogeneous viscosity, $\bar{\mu}$, and a two-phase Fanning friction factor, f_{tp}, instead of their single-phase equivalents. [45]

$$\left(\frac{\mathrm{d}p}{\mathrm{d}z}\right)_{tp,et,fr} = 2 \cdot \frac{f_{tp} \cdot \dot{m}^2}{\bar{\rho} \cdot D_i} \qquad (2.10)$$

Typical models for the two-phase Fanning friction factor, f_{tp}, are based on models for single-phase flow. For laminar flow, the model of Hagen-Poiseuille is adapted to two-phase flow. In the turbulent flow regime, the models of Blasius [61] or Konakov [62] serve as basis. The crucial point in evaluating these models for two-phase flow in empty tubes is the model to be chosen for the homogeneous viscosity. Various approaches have been proposed in the literature, see Thome and Cioncolini [45]. Choosing the model of McAdams [63] and the Blasius equation, Eq. (2.10) can be rearranged to express the two-phase pressure drop as a multiple of the single-phase pressure drop that would be predicted if the total flow was all liquid (La), see Eq. (2.11). The expression for the two-phase multiplier, Φ_{La}, can be derived directly from the models mentioned.

$$\left(\frac{\mathrm{d}p}{\mathrm{d}z}\right)_{tp,et,fr} = -\left(\frac{\mathrm{d}p}{\mathrm{d}z}\right)_{La,fr} \cdot \Phi_{La}^2 \qquad (2.11)$$

To account for the interfacial deformation turbulence due to different velocities of vapor and liquid phase, Storek and Brauer [60] multiplied a homogeneous model according to Eq. (2.10) with a correction function that depends, among other parameters, on the vapor quality.

To consider the different average velocities of the two phases, the frictional component can be modeled as a **multiple of the single-phase pressure gradient.** In contrast to the homogeneous model, the two-phase multiplier is expressed by empirical or semi-empirical correlations **(modeling approach 2)**. Either the liquid-all single-phase pressure gradient according to Eq. (2.11) or the liquid-only single-phase pressure gradient is used. Liquid-only (Lo) means the single-phase pressure gradient that would be predicted if the liquid portion of the total flow flows alone in the tube (compare also Table 2.5). Frequently applied models of this category are the model of Lockhart and Martinelli [64] and of Friedel [65]. [45,66]

Another possibility to consider the effects not covered by the homogeneous model is to model the frictional component by an **empirically based superposition** of the single-phase liquid and the single-phase vapor pressure drop or another reference pressure drop **(modeling approach 3)**. One of the most frequently used representatives of this category is the model of Müller-Steinhagen and Heck [67].

The second term of Eq. (2.8), the **acceleration component**, accounts for variations of the momentum density, ρ_m, and thus of the vapor quality (e.g. due to evaporation), the void fraction (e.g. due to a change of the phase distribution), or the vapor density (e.g. due to a pressure gradient in case of a compressible fluid) along the tube [45]. The acceleration component of the pressure drop is either calculated by integrating the second term of Eq. (2.8) between the inlet and outlet of the tube section under consideration **(separated model)** or by simplification to the homogeneous model. In the latter case, the acceleration component can be written as Eq. (2.12), since the momentum density coincides with the homogeneous density in the **homogeneous model** [45].

$$-\left(\frac{\mathrm{d}p}{\mathrm{d}z}\right)_{\text{tp,et,acc}} = \dot{m}^2 \frac{\mathrm{d}}{\mathrm{d}z}\left(\frac{1}{\bar{\rho}}\right) = \dot{m}^2 \frac{\mathrm{d}}{\mathrm{d}z}\left(\frac{\dot{x}}{\rho_{\text{V}}} + \frac{1-\dot{x}}{\rho_{\text{L}}}\right)$$

$$= \dot{m}^2 \dot{x} \frac{\mathrm{d}}{\mathrm{d}z}\left(\frac{1}{\rho_{\text{V}}}\right) + \dot{m}^2 \left(\frac{1}{\rho_{\text{V}}} - \frac{1}{\rho_{\text{L}}}\right)\frac{\mathrm{d}\dot{x}}{\mathrm{d}z} \qquad \textbf{(2.12)}$$

The acceleration component in the homogeneous model accounts for the compressibility of the vapor phase (first term) and the change of vapor quality (second term), e.g., due to evaporation. The compressibility of the gas phase may be neglected if Eq. (2.13) is valid [68]. Assuming an ideal gas, this condition can be also expressed in terms of Mach number, Ma. This condition is commonly fulfilled for flow conditions during flow boiling in horizontal tubes [60].

$$\left| \dot{m}^2 \cdot \dot{x} \cdot \frac{\mathrm{d}}{\mathrm{d}p}\left(\frac{1}{\rho_{\mathrm{V}}}\right) \right| = \dot{x} \cdot Ma^2 \ll 1 \qquad (2.13)$$

Assuming an incompressible vapor phase, the pressure gradient due to a change in vapor quality due to evaporation can be expressed by Eq. (2.14). Δh_{LV} is the enthalpy of vaporization. Thus, the acceleration component of the pressure gradient is proportional to the average heat flux related to the total tube surface area between the pressure taps, $\dot{q}^*$. The porosity, ψ_{o}, being 1 for empty tubes, is included to point out a possible adaption of Eq. (2.14) to flow through porous inserts.

$$-\left(\frac{\mathrm{d}p}{\mathrm{d}z}\right)_{\mathrm{tp,et,acc}} = \frac{\dot{m}}{\psi_{\mathrm{o}}} \cdot \left(\frac{1}{\rho_{\mathrm{L}}} - \frac{1}{\rho_{\mathrm{V}}}\right) \cdot \frac{4\,\dot{q}^*}{\Delta h_{\mathrm{LV}} \cdot D_{\mathrm{i}}} \qquad (2.14)$$

Since the acceleration component is mainly due to evaporation, the frictional component of the pressure gradient is conventionally approximated experimentally by measuring the pressure drop under adiabatic conditions. This adiabatic pressure drop is investigated in Section 4.1.2. The dependence of the pressure drop on the heat flux and the comparison to the acceleration component described in Eq. (2.14) is examined in Section 4.1.3.

2.3.3 Two-phase pressure gradient in porous inserts

There are numerous approaches for describing viscous and capillary flows through porous media. However, the mass flux typically encountered during flow boiling exceeds the scope of these models. For high mass fluxes, the literature agrees on the basic dependence on operating conditions, but no model concept is available to satisfactorily describe the two-phase pressure gradient in tubes with porous inserts [23].

The pressure gradient of two-phase flow in tubes with porous inserts generally shows the same dependence on operating conditions as the two-phase pressure gradient in empty tubes and the single-phase pressure gradient in tubes with inserts. Only the decrease of the pressure gradient with increasing vapor quality at high vapor qualities typical for two-phase flow in empty tubes is not (yet) observed for tubes with porous inserts. In addition, porous inserts can change the flow pattern [8,11,69], which can affect the pressure gradient of two-phase flow [68]. Figure 2.5 summarizes the key dependencies observed in literature.
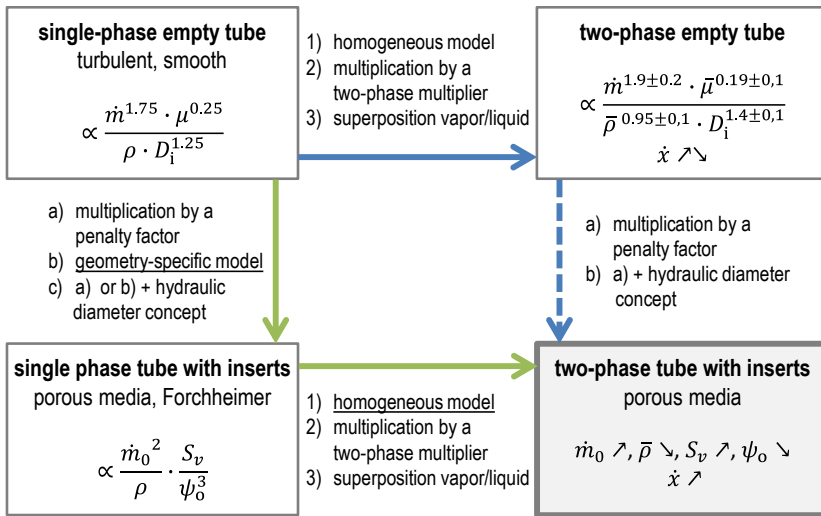
Figure 2.5: Dependence of the pressure drop on operating conditions, fluid properties, and geometrical characteristics according to Blasius [61], Storek and Brauer [60], Müller-Steinhagen and Heck [67], Forchheimer [70] and Weise et al. [23] as well as modeling concepts for the two-phase pressure drop in tubes with inserts.

Table 2.3 reviews the models proposed for the frictional component of the pressure gradient [15,18–22] of two-phase flow in tubes with sponge inserts.

Table 2.3: Pressure drop models proposed for two-phase flow through tubes with sponge inserts. D-F: Darcy-Forchheimer, exp.: fitted to experiments, F: Forchheimer, L-M: Lockhart-Martinelli [64].

authors	two-phase pressure drop approach	single-phase pressure drop	review
Madani et al. [18]	homogeneous	D-F (exp.)	use of Blasius equation [61] for derivation of two-phase multiplier invalid
Topin et al. [19]	homogeneous	D-F (exp. Tadrist et al. [71])	use of Blasius equation [61] for derivation of two-phase multiplier invalid
Ji and Xu [20]	adapted L-M	adapted D-F (exp. Ji and Xu [20])	single-phase correlation relies on empirical exponents
Hu et al. [21]	adapted L-M	D-F (Inayat et al. [72])	adaption of 5 fitting factors to relatively small database
Hu et al. [22]	adapted L-M	D-F (Inayat et al. [72])	adaption of 8 fitting factors to relatively small database, use of ppi number
Bamorovat Abadi et al. [15]	homogeneous, adapted L-M	empty tube: Blasius [61], Hagen-Poiseuille	mixing of the concepts two-phase multiplier and penalty factor, use of the homogeneous model for empty tube, use of ppi number
previous work, Weise et al. [23]	homogeneous	F (Woudberg and Du Plessis [57] or Inayat et al. [58])	only valid for vapor qualities < 50%

The authors chose either a homogeneous approach or an adapted Lockhart-Martinelli model. Commonly, the single-phase pressure gradient is predicted by a model aimed to describe the pressure drop in porous structures. Starting from this, the two-phase pressure drop is usually calculated by multiplication with a two-phase multiplier whose structure is based on the empty tube models. Table 2.3 reveals that all approaches proposed so far for two-phase flow through porous inserts are either based on invalid physical concepts, require fitting factors, or are only valid in a limited parameter range. In contrast to the concepts proposed for porous inserts, the pressure drop in tubes with twisted-tape inserts is calculated by multiplying the two-phase empty-tube correlation by a twisted-tape penalty factor [17,46,73,74], sometimes additionally using

the hydraulic diameter concept [46,74]. Besides geometric properties specific to twisted-tapes, these approaches also use fitting factors.

The most promising of the approaches presented here is that presented in a previous work (compare a previous work, Weise et al. [23]) since it does neither rely on invalid physical concepts nor needs a fitting factor. Moreover, inserts may reduce the slip between liquid and vapor phase. This would justify a homogeneous approach. Moreover, it was shown in a previous work that the homogeneous model could describe own [75] and comparable literature data of the pressure drop in tubes with sponge inserts best [23]. This homogeneous model considers the mass flux, $\dot{m}$, the homogeneous density, $\bar{\rho}$, and the structure of the sponge via the Forchheimer coefficient, β, according to Eq. (2.15). The homogeneous density is calculated according to. Eq. (2.5) and accounts for the vapor quality and the fluid properties, thus indirectly for the system pressure.

$$-\left(\frac{\mathrm{d}p}{\mathrm{d}z}\right)_{\mathrm{tp}} = \beta \cdot \frac{1}{\bar{\rho}} \, \dot{m}_0{}^2 \qquad (2.15)$$

A previous work suggests that the Forchheimer coefficient predicted with the models developed for single-phase flow by Woudberg and Du Plessis [57] or by Inayat [58] reach the order of magnitude of those determined experimentally [23]. To predict the Forchheimer coefficient the exact knowledge of the hydrodynamic porosity and the specific surface area of the structure is necessary. A precise determination of these quantities is difficult. The following criteria must be met for the model to be applicable [23]:

- the vapor quality is less than 50%
- the Darcy term is negligible, i.e., $Fo \approx \frac{0.14\,\sqrt{K}\cdot\dot{m}_0}{\psi^{1.5}\cdot\mu_{\mathrm{L}}} > 10$
- the vapor phase can be considered incompressible,
  i.e., $Ma_{\mathrm{V}} = \frac{\dot{m}}{\sqrt{\gamma p \rho_{\mathrm{V}}}} < 0.1$
- the heat flux is so small that the expected contribution of pressure drop caused by evaporation is negligible
- the influence of a confining wall is negligible,
  i.e., $\varepsilon \approx \frac{d_{\mathrm{w}}}{D_{\mathrm{i}}} < 0.12$ or $\psi(Pr_{\mathrm{L}})^2 \frac{K}{D_{\mathrm{i}}^2} \ll 0.019$

Most authors measured the pressure drop only under diabatic conditions. They neglect the **acceleration component** of the pressure drop or consider it by the separated model (second term of Eq. (2.9)) using the void fraction model by Rouhani [40] (apud [39]) for empty tubes. In contrast, data used for the previous work [23] and this work were measured both under adiabatic and diabatic conditions. This allows to investigate the influence of heating on the pressure drop.
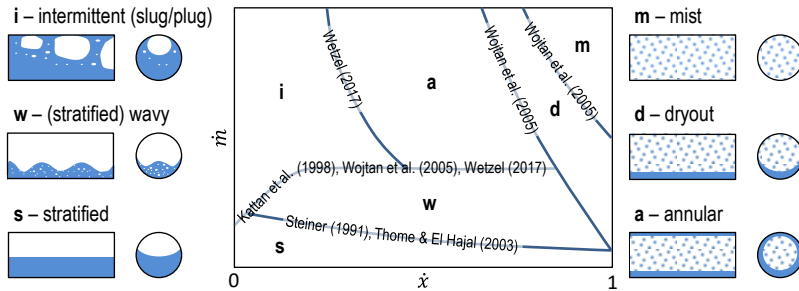
2.4   Flow pattern

In two phase flows, different phase distributions are classified into flow patterns. The flow pattern can influence the pressure drop [68]. Certainly, it has an effect on the heat transfer coefficient in horizontal tubes, since the local heat transfer depends on whether a tube segment is wetted or not [1]. In the following, the theory of flow patterns in empty tubes is explained. Based on this, the findings in the literature on flow patterns in tubes with inserts are reviewed.

2.4.1   Flow pattern in empty tubes

The predominant flow pattern of co-current flow in empty tubes depends on the mass flux, the vapor quality, the heat flux (and its direction), the fluid properties and the tube inclination [68,76]. Dominant physical mechanisms are different for macrochannels and mini/microchannels. During flow boiling in mini/microchannels, bubbles tend to be quickly confined and elongated in the channel even at very low vapor qualities [77]. In macrochannels, gravity plays an important role in the formation of the flow pattern. The diameter of the test section used in this work is large enough to be a macrochannel according to numerous criteria proposed in literature (Kandlikar and Grande [78], Li and Wu [79] or Harirchian and Garimella [80]). A recent review on flow patterns in horizontal macrochannels is given by Cheng et al. [81].

Alves [82 apud 68] defined the generally accepted flow patterns for horizontal tubes. Taitel and Dukler [83] developed transition criteria based on physical concepts and created a graphical representation for them in a flow pattern map

in dimensionless form for adiabatic flow. This map is valid for all fluid types and saturation pressures. Several authors published updates of the Taitel and Dukler map, adding flow patterns and modifying the calculation of the transition curves. Kattan et al. [84] transformed the dimensionless form of the flow pattern map to a more easily accessible form, displaying the transition curves as a function of the vapor quality and the mass flux. Such kind of map is only valid for one fluid type at a given saturation pressure, but the dependence on heat flux, i.e. a dryout region, can be incorporated [76,81,84–86]. This type of representation was chosen in Figure 2.6. There the flow patterns and the corresponding transition curves are shown schematically. In an initial work, it was investigated which flow pattern transition models are best suited to describe the heat transfer during the flow boiling of CO_2 in horizontal smooth tubes [2]. These transition models are included in Figure 2.6. Since the transition curves proposed so far are often close to each other, the transition is continuous, and the database was not sufficiently large in some areas, no single favorite could be determined for the transition from stratified flow to wavy flow and for wavy flow to intermittent/annular flow.

Figure 2.6: Schematic representation of a flow pattern map and the characteristic features of the individual patterns for diabatic two-phase flows in horizontal smooth tubes. The authors displayed on the transition curves published the correlations recommended in an initial work [2] for flow boiling of CO_2 in horizontal tubes. In detail these are Steiner [39], Thome and El Hajal [85], Kattan et al. [84], Wojtan et al. [76] and Wetzel [66].

2.4.2 Flow pattern in tubes with porous inserts

Observing flow patterns via a sight glass in tubes with porous inserts can be more difficult than in empty tubes because of the obstructed view. Nevertheless, this method is often used with highly porous inserts, for example by Bamorovat Abadi et al. [87] and Drögemüller and Gough [88]. Figure 2.7 (a) illustrates an intermittent as well as an annular flow observed during flow boiling of pure R245fa in a 20 ppi sponge. Figure 2.7 (b) shows a stratified-wavy flow of a water-air mixture in a horizontal tube with a wire matrix insert. In contrast, Zhao and Lu [44] as well as Zhu et al. [89] suggest to derive the flow patterns in tubes with sponges from the amplitude of the wall temperatures and the relative temperature difference at different positions along the tube perimeter (bottom, middle, top) at constant heat flux.
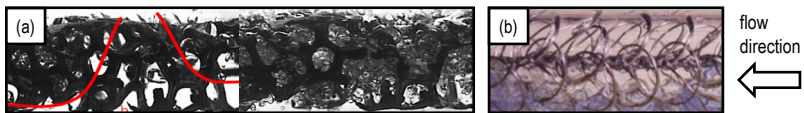

Figure 2.7: (a) Intermittent (left) and annular flow patterns (right) in a tube with sponge insert, reprinted from Bamorovat Abadi et al. [87], with permission from Elsevier.
(b) Stratified-wavy flow in tube with hiTRAN® wire matrix insert, reprinted from Drögemüller and Gough [88].

Figure 2.7 illustrates that inserting porous structures into a tube alters the flow pattern. Eventually, classifications other than used for horizontal empty tubes may be necessary and transition criteria need to be adapted. For sponges, Lu and Zhao [3], Zhu et al. [89], and Bamorovat Abadi et al. [87] propose to categorize the flow pattern according to the categories of horizontal flow in empty tubes. The structure of their flow pattern maps resembles the flow pattern maps of empty tubes. Lu and Zhao [3] and Zhu et al. [89] suggest one flow pattern map for all investigated sponge types and tube diameters (compare Figure 2.8 and Figure 2.9). In comparison to empty tubes, the transition from wavy to annular occurs at lower mass fluxes [44,90]. So far, no general modeling approach for the transition curves of flow patterns in horizontal tubes filled with sponges has been published.
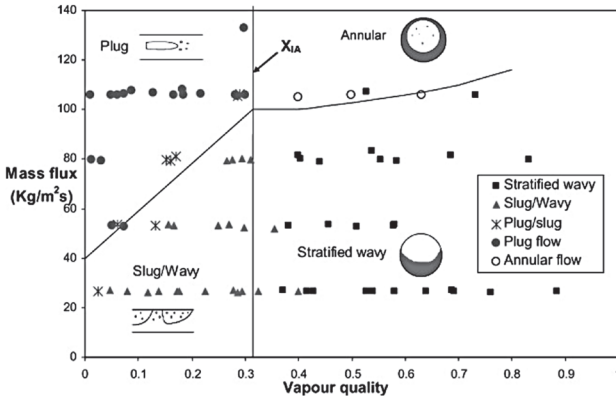
Figure 2.8: Flow pattern map for tube with inserts, reprinted from Lu and Zhao [3], with permission from John Wiley and Sons, fluid: R134a, reduced pressure $p_r \in \{0.09; 0.15\}$, 20 ppi and 40 ppi sponges, tube diameter: 26 mm, heated.
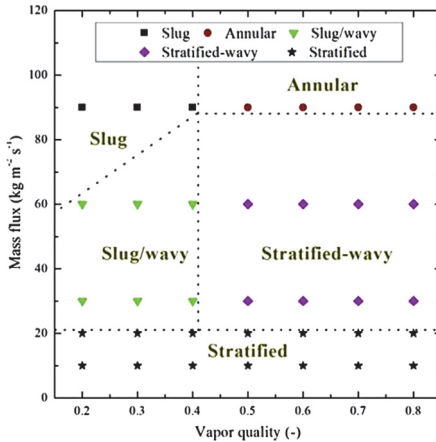
Figure 2.9: Flow pattern map for tube with inserts, reprinted from Zhu et al. [14], with permission from Elsevier, fluid: R410A, reduced pressure $p_r = 0.20$, tube diameter: 13.8 mm and 23.4 mm, sponge: 5 ppi – 10 ppi, heated.

A categorization for tubes with twisted-tape inserts differing from the classic empty tube categorization is given by Kanizawa and Ribatski [43]. They include stagnant flow and annular-stratified flow as shown in Table 2.4.

Table 2.4:   Flow patterns of two-phase flow in horizontal tubes with twisted-tape inserts accord-ing to Kanizawa and Ribatski [43]. The figures are reprinted from Kanizawa and Ribatski [43] with slight adaptions but without changes in content, with permission from Elsevier.

| schematic representation	description
stratified Liquid film	liquid in the bottom tube region and vapor in the upper part
stagnant Stationary liquid film Liquid droplets Vapor bubbles Liquid slugs	liquid slugs with low frequency between liquid slugs: stationary thick liquid film in the lower region of the tube
intermittent Noninterrupt liquid flow Liquid slugs Liquid droplets Vapor bubbles	liquid slugs with high amplitude and velocity blocking the tube section intermittently. between liquid slugs: non-stationary liquid film at the tube bottom and close to the tape edge
annular-stratified Liquid film Thicker film close to the lateral tape edges	non-uniform liquid film along the tube perimeter liquid film thicker close to the tape edge. small perturbations in the liquid vapor interface, perturbations unable blocking the tube cross section
annular	apparent uniform liquid film on the tube perimeter and relatively small interfacial perturbations

2.5   Heat transfer

Flow boiling is the evaporation of a fluid flowing through a tube by heat input from the environment [91]. Due to a lack of a coherent theory, numerous model approaches are known for heat transport during flow boiling in empty horizontal tubes. For tubes with inserts, only few model approaches have been suggested. Since the hypothesis is to be tested whether flow boiling in tubes with porous inserts can be described using the model equations for heat transfer in flow boiling in empty tubes and single-phase heat transfer in tubes with porous inserts, these two topics are addressed first. A model is presented that describes the experimental data obtained in the flow boiling test facility for empty tubes well. Then, the literature on flow boiling in tubes with inserts is reviewed.

2.5.1   Flow boiling heat transfer in empty tubes

This chapter focusses on the description of heat transfer during **saturated flow boiling** in horizontal macrochannels. Boiling of a saturated liquid implies that the average temperature of the liquid is equal to the equilibrium temperature corresponding to the system pressure [91]. This condition is approximately fulfilled for flow boiling with the exception of very small and very large vapor qualities. The assumption of thermodynamic equilibrium allows the calculation of the vapor quality from an enthalpy balance according to Eq. (2.16) [91].

$$\dot{x} = \dot{x}_{\text{eq}} = \frac{h - h_{\text{L}}}{\Delta h_{\text{LV}}} \qquad \textbf{(2.16)}$$

The predominant heat transfer mechanisms in saturated flow boiling depend on the operating conditions ($\dot{x}, \dot{m}, \dot{q}$) and fluid properties ($\rho_{\text{L}}, \rho_{\text{V}}, \sigma, T_{\text{LV}}, \Delta h_{\text{LV}}$). Consequently, flow boiling is classified into different regions. Figure 2.10 outlines these regions as a function of heat flux and vapor quality. Also illustrated is the heat transfer coefficient curve at constant heat flux (blue) and constant vapor quality (red). The individual regions and the transition curves are explained below.
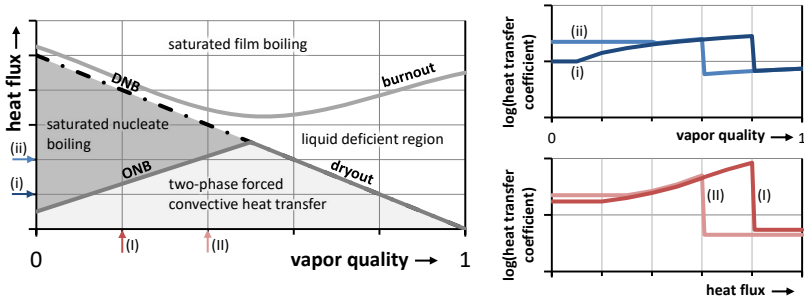
Figure 2.10: Qualitative classification of saturated flow boiling as a function of vapor quality and heat flux as well as dependence of the heat transfer coefficient on vapor quality and heat flux. Illustration is a combination of illustrations from Collier and Thome [68] and Baehr and Stephan [92]. Curves of the heat transfer coefficient are shown for constant heat flux (i and ii, blue) and constant vapor quality (I and II, red).

Two-phase forced convective boiling occurs at heat fluxes below the onset of nucleate boiling (ONB) or dryout. Heat is transferred by conduction and convection through the liquid and vapor is continuously generated at the phase interface [68]. The heat transfer coefficient increases with vapor quality and mass flux, independent of heat flux [68,93]. **Dryout** occurs after a critical heat flux is reached and the liquid film on the wall is completely evaporated. It is characterized by a sharp decline of the heat transfer coefficient (compare Figure 2.10, curve i and ii in blue). In the **liquid deficient regime** droplets and rivulets still cool the wall more efficiently than vapor alone would [68].

At heat fluxes higher than the **onset of nucleate boiling (ONB)**, the boundary layer is superheated sufficiently to allow the formation of stable bubbles by heterogeneous nucleation at nucleation sites at the tube wall. The corresponding heat flux, $\dot{q}_{ONB}$, depends on fluid properties and flow conditions (effective convective boiling reduces the superheat in boundary layer at tube wall). **Saturated nucleate boiling** thus superimposes the convective heat transfer and the heat transfer by bubbles departing from the wall. The heat transfer coefficient is almost independent of vapor quality and mass flux and increases with increasing heat flux as smaller bubbles are stable, i.e. more bubbles can be formed [68]. At even higher heat fluxes, the bubbles coalesce to a vapor film, called **departure from nucleate boiling (DNB)** [68].

Numerous **models** have been proposed for heat transfer in the forced convective boiling range and in the saturated nucleate boiling range. For boiling in horizontal tubes, the influence of wetting additionally superimposes these mechanisms. Therefore, models are preferred which first calculate the wetted perimeter of the tube wall as a function of the predicted flow pattern and subsequently compute the heat transfer coefficient in the wetted and dry regions of the tube separately. In addition, the boundary condition at the tube wall must be considered for flow boiling in horizontal tubes. The tube wall can be heated either with heat flux uniformly distributed over the circumference or at a constant wall temperature. The latter can result in non-uniform heating of the tube wall in case of asymmetrical flow distribution.

The well-established flow pattern-based models by Thome's group [1,42,94,95], developed for horizontal circular tubes heated at a constant heat flux, could not describe satisfactorily the experimental data of CO_2 at a constant wall temperature [24,66]. Thus, in an initial work (compare Weise et al. [2]) the flow pattern-based models proposed by Thome's group to the constant wall temperature condition are adapted. For this purpose, experimental data by Schael [24], Wetzel [66] and own data [96] are used. The model thus derived can predict more than 80% of all data within an error interval of $\pm 30\%$ and reproduces observed trends well [2]. Figure 2.12 illustrates the structure of this model for calculating the local heat transfer coefficient in a segment j, $\alpha_{\mathrm{tp},j}$. Based on the void fraction, ε, the dry angle of a hypothetical stratified flow, $\theta_{\mathrm{dry,s}}$, is calculated. Using this angle, the fluid properties, and the heat flux, the transition curves of the flow patterns are determined. According to the particular flow pattern, the dry angle, θ_{dry}, and thus the dry fraction of each segment, $f_{\mathrm{dry},i}$, can be computed. Along the unwetted arc of the tube, the vapor heat transfer coefficient, α_{V}, is calculated by adapting the Dittus and Boelter single-phase heat transfer correlation [97] to the two-phase flow. The heat transfer coefficient of the wetted arc is calculated by a cubic superposition (first suggested by Steiner and Taborek [98]) of the nucleate boiling heat transfer coefficient, α_{nb}, and a convective boiling heat transfer coefficient, α_{cb}. The nucleate boiling heat transfer coefficient, α_{nb}, is modeled according to Cooper's pool boiling model [4], as given in Eq. (2.17). The equation is based

on the reduced pressure, p_r, the molar mass, $\widetilde{M}$, and the local heat flux, $\dot{q}_j$. This widely used form of Cooper's equation assumes a surface roughness of 1 µm and applies to most tube material. Cooper suggests a constant of 95 instead of 55 when the tube material is copper [99 apud 4]. In the analysis in the initial work [2], 55 was used for both copper and brass tubes, since no difference was observed between the two test section materials (compare also Section 3.5) and and thus the model is consistent with the models from Thome's group.

$$\frac{\alpha_{\text{nb},j}}{\text{W m}^{-2}\text{K}^{-1}} = 55 \cdot p_r^{0.12} \cdot [-\log_{10} p_r]^{-0.55} \cdot \left(\frac{\widetilde{M}}{\text{g mol}^{-1}}\right)^{-0.5} \cdot \left(\frac{\dot{q}_j}{\text{W m}^{-2}}\right)^{0.67} \quad \textbf{(2.17)}$$

The calculation procedure of α_{cb} was determined by Kattan et al. [1] by comparing their model with experimental flow boiling data (Figure 2.11).
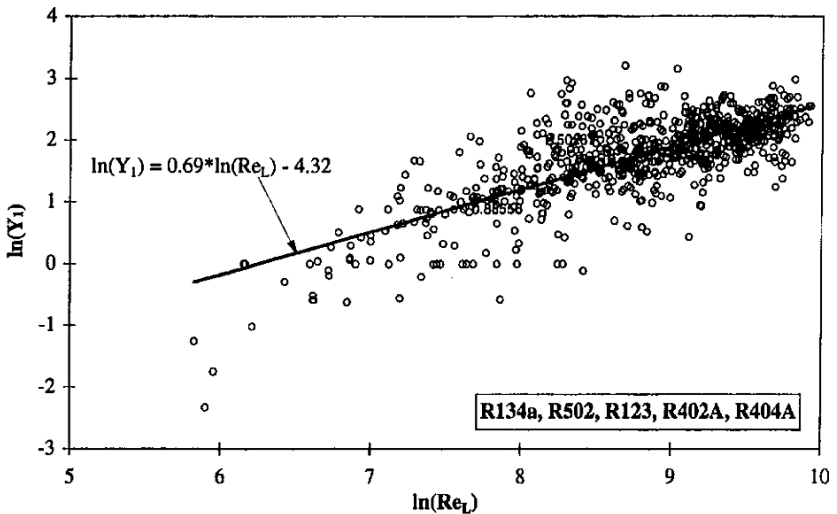
Figure 2.11: Development of convective boiling heat transfer correlation according to Kattan et al. [1]. $Y_1 = Nu_{\text{cb,exp}} \cdot Pr^{-0.4}$ with $Nu_{\text{cb,exp}}$ based on the film thickness, δ. Re_L corresponds to $Re_{L,\delta}$ according to Eq. (2.22). Figure is reprinted from Kattan et al. [1], with permission from ASME.

27
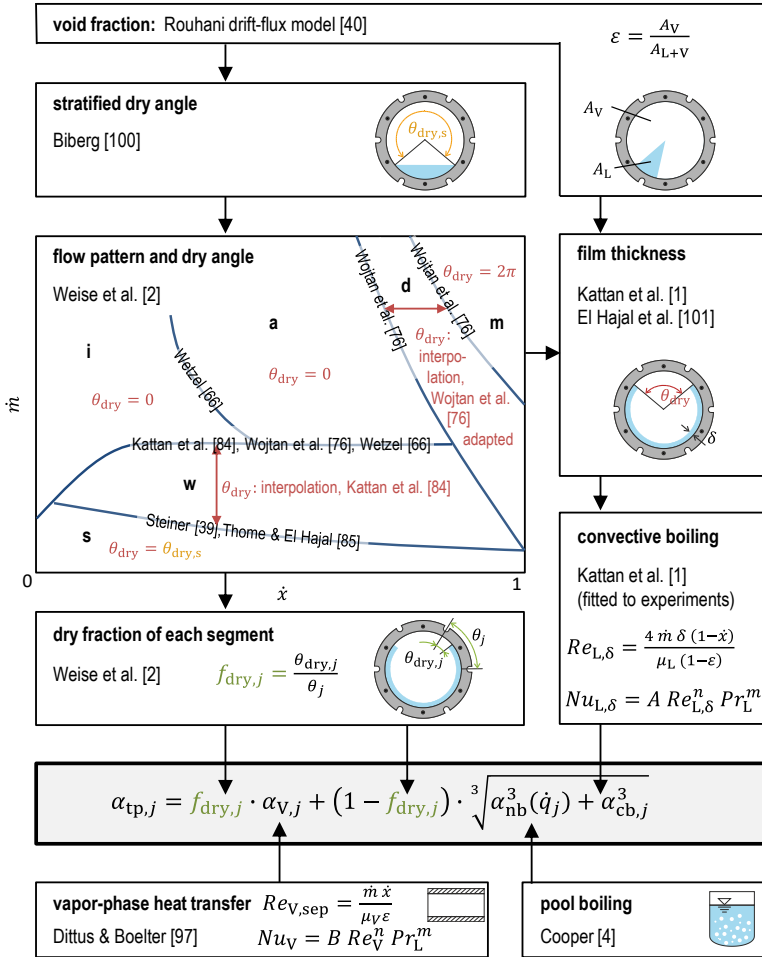
Figure 2.12: Overview of the recommended structure of a flow pattern-based model for predicting the local heat transfer coefficient for non-uniformly heated empty evaporator tubes [1,2,4,39,40,66,76,84,85,97,100,101] according to an initial work (Weise et al. [2]). If two or more models are proposed for the same step, the database was not sufficient enough for an unambiguous decision. The flow patterns are explained in Figure 2.6. All equations are listed in the initial publication [2].

An important aspect of modeling flow boiling is the adaptation of the single-phase heat transfer correlations to the two-phase flow. This is done by using a two-phase Reynolds number, for which there are several different definitional approaches. Table 2.5 illustrates five of these approaches using the liquid phase as an example. The Reynolds number of the vapor phase is defined analogously. In the model suggested in an initial publication (Weise et al. [2]) for empty tubes, the separated Reynolds number, $Re_{V,sep}$, is used for the vapor phase while the film Reynolds number, $Re_{L,\delta}$, is used for the liquid phase. For the adaption of the single-phase heat transfer correlations of tubes with inserts, the choice of the Reynolds number will play an important role.

Table 2.5: Overview of definitions for two-phase Reynolds numbers for heat transfer in the liquid phase.

model	concept	equation	
liquid-only	liquid portion of the total flow assumed to flow alone in the tube	$Re_{Lo} = \dfrac{\dot{m} \cdot (1 - \dot{x}) \cdot D_i}{\mu_L}$	**(2.18)**
liquid-all	total flow assumed to be liquid	$Re_{La} = \dfrac{\dot{m} \cdot D_i}{\mu_L}$	**(2.19)**
homogeneous	total flow assumed to be homogeneous mixture, liquid film at the wall	$Re_{L,hom} = \dfrac{\dot{m} \cdot D_i}{\bar{\rho} \cdot v_L}$	**(2.20)**
separated	liquid portion of total flow assumed to flow in cross section occupied by liquid	$Re_{L,sep} = \dfrac{\dot{m} \cdot (1 - \dot{x}) \cdot D_i}{\mu_L (1 - \varepsilon)}$	**(2.21)**
film	liquid portion of total flow assumed to flow in film distributed at tube wall	$Re_{L,\delta} = \dfrac{4 \cdot \dot{m} \cdot (1 - \dot{x}) \cdot \delta}{\mu_L \cdot (1 - \varepsilon)}$	**(2.22)**

2.5.2   Heat transfer in tubes with porous inserts

In the modeling approach for empty tubes presented in Section 2.5.1, the corresponding single-phase heat transfer model is used to describe the heat transfer coefficient in unwetted tube segments during flow boiling. This indicates that this approach could be transferable to the description of the vapor heat transfer coefficient in tubes with inserts. Due to the better mixing of the two phases by the inserts compared to empty tubes, the convective part of the flow boiling in the wetted region of tubes with inserts could possibly also be de-

scribed by appropriate single-phase heat transfer models. Correlations describing the single-phase heat transfer at the wall would be predestined. As these correlations were and still are scarce, some authors also approximated the heat transfer coefficient at the wall by correlations for the heat transfer coefficient inside porous structures. Consequently, both correlations for the heat transfer inside porous structures and for heat transfer at a wall adjacent to a porous structure are reviewed in the following.

This latter approach was pursued e.g. by Lu and Zhao [3]. They suggested using the single-phase correlation by Žukauskas [102] to calculate the vapor heat transfer in the sponge structure and at the tube wall. Žukauskas [102] investigated the heat transfer in staggered arrangements of tubes. Their frequently cited correlation (Eq. (2.23)) was fitted to their experimental data of the heat transfer coefficient at the first row in such an arrangement. The characteristic diameter, d, is calculated by Lu and Zhao [3], similar to Calmidi and Mahajan, by accounting for the strut shape of sponges. For $40 \leq Re \leq 1000$, the exponent m is 0.5 and the constant $C = 0.51$. Žukauskas defines the Reynolds number, Re, with respect to the superficial velocity.

$$\alpha_V = C\,Re^m Pr^{0.37} \frac{\lambda_V}{d} \qquad \textbf{(2.23)}$$

Calmidi and Mahajan [103] compared the correlation of Žukauskas [102] to their experimental data for the heat transfer in sponges in a porosity range of $\psi = 0.89 - 0.97$ and found the same Reynolds characteristic. From their data, Calmidi and Mahajan could conclude that $C > 0.52$ for $40 \leq Re \leq 1000$ although their correlation is frequently cited with $C = 0.52$.

Meinicke [104] conducted a numerical study of the heat transfer coefficient in precisely reconstructed sponge samples, among others of the 10 ppi and the 20 ppi sample used for this thesis. He proposed to model the heat transfer coefficient of air ($Pr_V = 0.7$) flowing through sponge samples by Eq. (2.24). Fitting the correlation to numerical results for $0.1 < Re < 100$ yielded $c = 0.39$ and $Nu_{min}^3 = 0.71$. Assuming the same dependence of Nu on Pr as Žukauskas [102] results in $C = 0.45$.

$$Nu_V = \frac{\alpha_V d_s}{\lambda_V} = \sqrt[3]{Nu_{min}^3 + (C \cdot Re^{0.5})^3} \qquad \textbf{(2.24)}$$

The heat transfer coefficients numerically determined by Meinicke are approximately 13% lower than the model of Žukauskas [102].

To describe the single-phase heat transfer coefficient at a tube wall with adjacent sponge inserts, only the correlations by Bianchi et al. [5] are available. They derived correlations depending on the gap width between the tube wall and the inserted sponge structure. Eq. (2.25) describes the Nusselt number, Nu, for a gap of 100 µm and constant wall temperature. The Péclet number, $Pe = Re \cdot Pr$, is related to the window diameter, d_w and the intrinsic velocity, $u = \dot{m} \cdot \rho^{-1}$.

$$Nu = \frac{\alpha \, d_w}{\lambda} = 1.97 + 0.09 \, Pe^{0.73} \; ; 2 < Pe < 64000 \qquad \textbf{(2.25)}$$

For wire matrix elements, there is no known general relationship in the literature for calculating single-phase heat transfer at the tube wall. For the specific hiTRAN® wire matrix element used in this work, a confidential single-phase heat transfer correlation by CALGAVIN Ltd. [33] based on Reynolds number and Prandtl number is available.

2.5.3 Flow boiling heat transfer in tubes with porous inserts

In the following, relevant experimental studies, prevailing mechanisms, and modeling approaches for flow boiling heat transfer in tubes with porous inserts are summarized. Where relevant, porous fins are also considered.
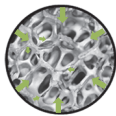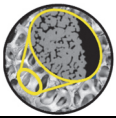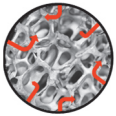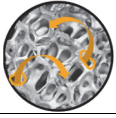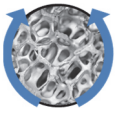
While there are several **studies** on heat transfer during flow boiling in horizontal tubes with twisted-tape and wire-coil inserts [16,17,105–113], only publications on flow boiling in vertical channels are known for sponge inserts or wire matrix elements. Furthermore, there are investigations on flow boiling in horizontal tubes with sponges soldered to the tube wall.

Madani et al. [18] studied the boiling of n-pentane in a vertical rectangular channel with sponge inserts. Comparing their experimental results with the heat transfer in an empty channel based on a correlation for flow boiling of water, they state that the insertion of sponges increases the heat transfer coefficient. Compared to experimental results with sponges soldered to the channel wall, the heat transfer coefficient was slightly smaller for inserted sponges. Drögemüller [9] suggests the use of hiTRAN® wire matrix elements for falling film evaporators with viscous mixtures, as the elements disturb the laminar sublayer, resulting in a better mixing and thus a larger driving temperature difference for a mixture of fluids with different saturation temperatures. In addition, the distribution of the liquid film is improved. Hammerschmidt and Scholl [114] investigated the use of a hiTRAN® wire matrix element in a natural circulation evaporator with water or water-glycerol mixtures. Compared to the empty tube, the inserts increase the heat transfer coefficient during evaporation. The research groups Lu/Zhao [3,44,90], Zhu/Hu [13,14,89,115,116] and Bamorovat Abadi/Kim [15,87,117] studied flow boiling in horizontal tubes with sponges soldered to the tube wall (porous fins). They investigated sponges made from copper (porosity between 85% and 96%, 5 ppi to 40 ppi). They used R134a, R410A, and R245fa as a working fluid. The tube diameter varied from 4 mm (Bamorovat Abadi/Kim) to 26 mm (Lu/Zhao). Common to these investigations is that an increased heat transfer coefficient by up to a factor of three was found compared to the empty tube. Zhu et al. [14] state that especially the convective heat transfer coefficient is enhanced, thus the relative increase compared to an empty tube is high for high vapor quality and mass flux. At low mass fluxes, the structure scarcely influences the flow [14].

To summarize, the heat transfer during flow boiling is increased both for vertical channels with inserts and for horizontal channels with porous fins. However, there is disagreement about the **prevailing mechanisms** that lead to the observed improvement and thus the transferability of the results to flow boiling in horizontal tubes with porous inserts. Table 2.6 lists and categorizes mechanism discussed in the literature and specifies the conditions under which these mechanisms might come into play. For classification purposes, it is necessary to distinguish between fins and inserts (compare Section 2.1). With favorable material and geometric properties, fins can provide an additional path for heat

transfer from the tube wall to the fluid, namely through the solid structure. In inserts, heat conduction in the solid structure is negligible due to the large contact resistance between the structure and the tube wall; therefore, heat transfer to the fluid is dominated by heat transfer to the tube wall. However, like fins, inserts may influence the flow characteristics, such as the flow pattern or the velocity gradient adjacent to the wall, thus affecting the heat transfer at the tube wall.

Table 2.6: Suggested mechanism by which porous fins and inserts can influence the heat transfer coefficient during flow boiling. The mechanisms specific to porous fins are additionally listed to show the differences. Notes in italic are own conclusions.

fins		in case of high thermal conductivity of continuous structure [19], low contact resistance [14], high heat transfer area [8,14,19], *heat transfer coefficient dominated by convection* → additional heat transfer through structure (fin effect) [14,19,118–120] → *enhancement especially of vapor heat transfer coefficient*
		in case of heat transfer through structure, high surface roughness → additional nucleation sites [8,11,14] / promotion of bubble incipience [121] → *increase of nucleate boiling contribution*
fins and inserts		in case of small channels and struts adjacent to the wall → steeper local velocity gradients, steeper temperature gradients, disturbance of thermal boundary layer [12], restrained bubble growth and departure [8,14] → increase of convective boiling contribution [8,21,119,122], decrease of nucleate boiling contribution [14]
		in case of statistic obstructions [19], tortuous fluid path [8], or centrifugal convection [11,119] → better mixing [8,9,14,19,44,119,122] → increase convective boiling contribution [8,14,119]
		in case structure acting as climbing aid or centrifugal forces → better wetting of tube wall [3,9,14,17,21,43,87] → increase average heat transfer coefficient in original wavy or intermittent flow regime [14], *postpone dryout, improve heat transfer coefficient in mist flow*

Lu and Zhao [3] presented a flow pattern-based **model** for the heat transfer coefficient during flow boiling in uniformly heated horizontal tubes with soldered sponges (see Figure 2.13), i.e. porous fins. Similar to the flow pattern-based empty tube model by Kattan et al. [1] (compare Figure 2.12), the void fraction and the stratified dry angle are calculated according to Rouhani [40]

and Biberg [100]. Based on an experimentally determined transition curve from wavy-to-intermittent/annular flow, the dry angle is identified. For linear interpolation in the wavy flow region, Lu and Zhao assumed that the transition from stratified flow to wavy flow occurs at very low mass flux and thus set the transition to $0 \text{ kg m}^{-2} \text{ s}^{-1}$. The film thickness is calculated according to the empty tube correlation by Kattan et al. [1]. The heat transfer through the sponge structure is considered by numerically solving a homogeneous energy equation. The heat transfer coefficient at the solid-fluid interface is calculated in the vapor phase according to a model of Žukauskas [102] for staggered cylinders and in the liquid phase according to the Cooper equation (pool boiling) [4]. Due to its modular design, this model can be adapted to a flow through a tube with inserts. In this case, the high contact resistance at the wall prevents relevant heat transfer in the structure and thus between the structure and the fluid. For this purpose, only the heat transfer coefficient at the tube wall is considered.

Zhu et al. [14], Bamorovat Abadi et al [15], Agrawal and Varma [16], and Akhavan-Behabadi [17] pursued another approach for **porous fins and twisted-tape inserts**. They calculated the boiling heat transfer coefficient in an empty tube at the same operating conditions and multiplied it by an impact factor fitted to experimental data. This impact factor differs in the influencing factors considered.
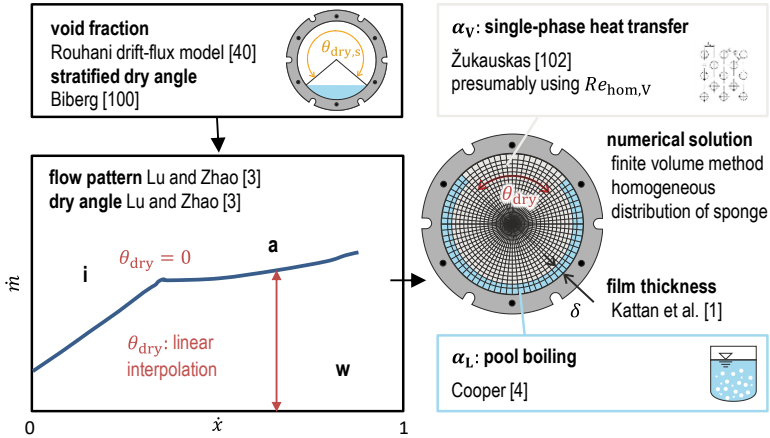
Figure 2.13: Flow pattern-based model for the heat transfer coefficient during flow boiling in uniformly heated horizontal tubes with soldered sponges according to Lu and Zhao [3].

2.6   Interim conclusion

Sections 2.3.3, 2.4.2 and 2.5.3 support the problem formulated in the introduction that there is a lack of models without fitting parameters necessary for the optimization of flow boiling heat transfer in horizontal tubes with porous inserts. For the pressure drop, all proposed models rely on invalid concepts, require fitting parameters, or are valid only in a limited parameter range. For the flow pattern, there is no general model approach yet. For the heat transfer coefficient in tubes with porous inserts, no model is known so far either. Whether the model concepts of porous fins can be transferred to porous inserts is questionable, since there is disagreement in the literature about the prevailing mechanisms.

However, promising model approaches and the necessary established laws could be identified for both the pressure drop and the heat transfer coefficient. In detail, these are the homogeneous model approach (see Section 2.3.2) combined with suitable single-phase correlations (see Section 2.3.1) for the pressure drop, as suggested in a previous paper [23], and a model approach based on the empty tube concept by Kattan et al. [1] (see Section 2.5.1) combined

with single-phase correlations for porous inserts (see Section 2.5.2) for the heat transfer coefficient.

This allows the assumption that the hypothesis stated in the introduction can be confirmed at least in part. For a verification or falsification of the hypothesis, the test section presented in the next chapter allows the simultaneous measurement of the pressure drop, the heat transfer as well as the flow pattern. A special feature of this test section is the measurement of the spatially resolved heat transfer in the circumferential direction as well as the determination of the flow pattern via various methods. This allows an in-depth insight into the mechanisms of flow boiling, so that an evaluation of physical concepts is possible.

3 Experimental setup and data evaluation

The experiments were carried out on the flow boiling test facility at the Institute of Thermal Process Engineering (TVT) of the Karlsruhe Institute of Technology (KIT). The test facility consists of a test loop in which liquid CO_2 can be pre-evaporated to achieve a desired vapor quality in the test section. Thus, the test section is representing a short section of a horizontal evaporator tube. CO_2 was chosen as working fluid because it is considered a sustainable medium for refrigeration and also has suitable physical properties in the context of testing the hypothesis.

To investigate the influence of porous inserts on flow boiling in a horizontal tube, a new empty tube test section was designed to meet the requirements of high-resolution temperature measurement. The inner diameter of this test section corresponds exactly to the inner diameter of a former empty tube test section, so that validation is possible. The former empty tube test section was designed by Niederkrüger [123] and used by Schael [24] and Wetzel [66] for CO_2 flow boiling experiments.

The condenser necessary for condensation of the working fluid and the subsequent sub-cooler are cooled by two brine circuits, which are fed from a brine buffer tank. This tank is, in turn, cooled by a vapor-compression refrigeration system. The brine circuits and the vapor-compression refrigeration system were recently revised by Wetzel [68], who describes this part of the test facility in detail in his work. Therefore, Section 3.1 concentrates on the description of the test loop, mainly on the test section. After validating the new empty tube test section used in this work, two different types of sponges and a wire matrix element were inserted into the test section. The relevant properties and the position of the inserts are discussed in Section 3.3. The experimental procedure, the operating conditions, and the derivation of heat flux, the vapor quality, the pressure drop and the heat transfer coefficient from the measured quantities are described in Section 3.4.

Parts of the following sections were adapted from the publications of the experimental data, compare Weise et al. [75,96].

3.1 Test circuit

Figure 3.1 illustrates the test circuit of the flow boiling test facility. The following explanation starts with the centrifugal pump of the test circuit (bottom left) and follows the path of the CO_2 in the measuring mode. This hermetic refrigerant pump (TH. WITT Kältemaschinenfabrik GmbH) delivers pure subcooled CO_2 (purity grade 4.5) into the test circuit as well as into a bypass. The bypass is required for the minimum volume flow necessary for cooling the pump. Through the interaction of the orifice plate installed in the bypass and an electronic control valve in the test circuit, the mass flow rate in the test circuit can be adjusted. A Coriolis mass flow meter (Promass F 60 by Endress+Hauser AG) measures the mass flow rate shortly after the bypass is branched off. Directly thereafter, the temperature and pressure of the subcooled liquid is measured (platinum resistance temperature sensor Pt100 and burster 8103-50 by burster Präzisionsmesstechnik GmbH & Co. KG respectively). On the one hand, these values are used in the enthalpy balance to determine the vapor quality in the measuring section (see Section 3.4.4), and on the other hand, it can be ensured that the liquid is actually subcooled at this point. A particle filter (depth filter) is used to remove any corrosion particles from the circuit. Subsequently, three pre-evaporators partially evaporate the CO_2. These are electrically heated at the bottom of the tube. The pre-evaporator directly upstream of the test section has the same internal diameter as the latter in order to avoid entrance effects and, if necessary, also to be filled with inserts. The electrically heated test section is equipped with sensors for determining the wall temperature (thermocouple type E), saturation pressure (burster 8103-50 by burster Präzisionsmesstechnik GmbH & Co. KG), differential pressure (Rosemount 3051C by Emerson Electric Co.) and electrical power (WT 1030 by Yokogawa Deutschland GmbH). The test section is discussed in detail in Section 3.2). Downstream of the test section, the flow can be observed via a sight glass. A high-speed camera (Motion Corder Analyzer by Kodak, frame

rate: 500 fps) records the observations. Further downstream, the vapor is rel-iquefied in a shell and tube condenser using a secondary brine cooling circuit. The pressure in the test section depends on the saturation pressure in the condenser. This saturation pressure in turn is adjusted by controlling the temperature of the brine at the condenser outlet. The CO_2 returns to the centrifugal pump via a storage tank and a sub-cooler (double tube heat exchanger), which is also cooled by the secondary brine cooling circuit. The sub-cooler prevents cavitation in the centrifugal pump. The complete test circuit is insulated with ArmaFlex® or - in the vicinity of the pre-evaporators - with aluminum foil-laminated rock wool.
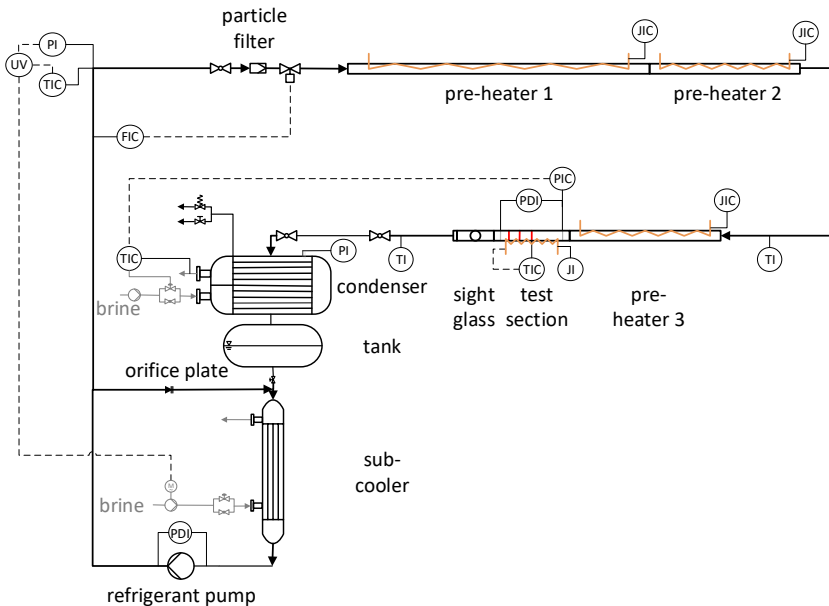
Figure 3.1: Process flow diagram of the flow boiling test facility. Figure adapted from the publication of the experimental data, compare Weise et al. [96].

The standard uncertainties of the instruments are specified in Table 3.1. These uncertainties are included in the analysis of the measurement uncertainty of the operating and result variables as presented in Section 3.4.

Table 3.1: Instrument standard uncertainties ($k = 1$) according to the publication of the experimental data, compare Weise et al. [96].

instrument	$\sigma\ (k = 1)$	notes
digital power meter	±0.05% of reading	according to calibration
thermocouple type E (test section)	±0.14 K	mainly due to geometrical imperfection of the test section and irregular heat transfer, determined by numerical simulation
thermocouple type E (insulation test section)	±0.02 K	with external cold junction, calibrated, uncertainty of calibration standard and calibration procedure
thermocouple type K (insulation)	< ±0.4 K	with internal cold junction, IEC-60584-1 [9], checked by comparison to calibration standard
resistance thermometer (Pt100)	±0.02 K	uncertainty of calibration standard and calibration procedure
pressure transducer	0.0018 MPa ±0.008% of reading	uncertainty of calibration standard and calibration procedure
differential pressure transducer	±40 Pa	uncertainty of calibration standard and calibration procedure
mass flow meter	±0.15% of reading; : ±0.02% of range	manufacturer's specification

3.2   Test section

The test section was especially designed for measuring the heat transfer coefficient and the pressure drop of flow boiling in tubes with inserts. It resembles formerly used smooth tube test sections [24,66,123], but bears more thermocouples and has a different heating concept beside being able to host various inserts.

Figure 3.2 illustrates the axial view of the test section, combined with the adjoining sight glass. Table 3.2 lists relevant specifications of the test section.
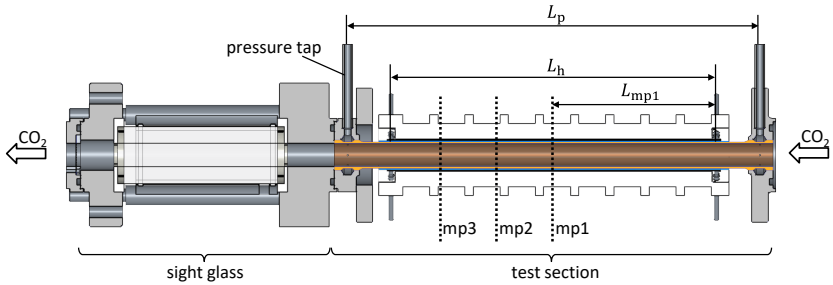
Figure 3.2: Axial view of test section and sight glass. The position of the three measurement planes (mp), the heated length, L_h, and the distance between the pressure taps, L_p, are illustrated.

The pressure is measured via six holes distributed around the circumference at the inlet and six holes at the outlet of the tube. These holes connect the tube to two annular chambers integrated in the inlet and outlet flange. The annular chambers ensure the correct determination of an average static pressure of the two-phase flow, independent of the flow pattern. The annular chamber at the inlet of the tube is connected to a pressure transducer (burster 8103-50). Both annular chambers are connected to a differential pressure transducer (Rosemount 3051C).

The wall temperature is measured in three measurement planes (mp1, mp2, mp3). The tips of up to 6 type E thermocouples (304 stainless steel sheath, grounded junction) are located in these planes of measurement. The thermocouples are soldered into axial grooves in the tube wall. To obtain a uniform temperature distribution, thermocouple dummies are soldered into all grooves without thermocouples. Figure 3.3 shows the location of the thermocouples. The reference junctions of the thermocouples are electrically isolated by small glass tubes filled with silicon oil and tempered in a copper block immersed in a thermostat. The temperature of the reference junction is measured by a platinum resistance temperature sensor (Pt100). The temperature of the thermostat is set to 40 °C.

41
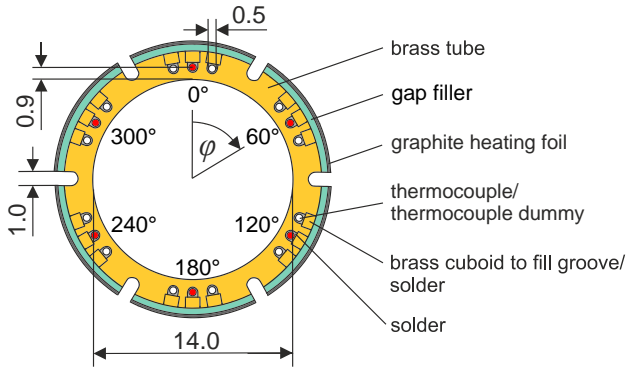
Figure 3.3: Cross-sectional view of test section in the heated zone. The thermocouples tips (marked in red) in mp1 are located at angles $\varphi = 0°$; 60°; 120°; 180°; 240°; 300°. Figure adapted from the publication of the experimental data, compare Weise et al. [96].

The heated zone of the pipe is divided by grooves into six circumferential segments. Graphite heating foils heat each segment independently. The heating foil is electrically separated from the test section by a gap filler. The tube material and the depth of the grooves was optimized by numerical simulation to achieve a compromise between azimuthal heat conduction and temperature homogeneity at the inner tube wall (see Appendix B.3). Three polyoxymethylene shells and staggered hose clamps fix the heating foil and the gap filler. This arrangement allows the segments to be heated as evenly as possible and reduces the contact resistance between the outer tube wall and the heating foil. The graphite heating foils are electrically contacted with high current test probes. The power input is measured by two digital power meters (WT1030 by Yokogawa Deutschland GmbH). Table 3.2 specifies the geometrical and thermal characteristics of the test section as well as exact designation of the components and directly installed sensors.

Table 3.2:   Specification of the test section.

|		
tube material	brass, CuZn39Pb3	
inner diameter	14.00 mm $\pm$ 0.01 mm	
distance between pressure taps, L_p	247 mm $\pm$ 0.7 mm	
heated length, L_h	195 mm $\pm$ 5 mm	
distance between beginning of the heating zone and the planes of measurement, $L_{mp1}, L_{mp2}, L_{mp3}$	mp1 mp2 mp3	97.5 mm $\pm$ 3.5 mm 130.5 mm $\pm$ 3.5 mm 163.5 mm $\pm$ 3.5 mm
distance between the thermocouple tip and the inner surface of the tube wall	mp1 mp2 mp3	0.91$\pm$0.10 mm 0.89$\pm$0.10 mm 0.88$\pm$0.10 mm
mean arithmetic surface roughness, R_A	0.8 · 10^{-6} m	
thermal conductivity of brass, λ_{ts}	116 $\pm$ 8 W m-1 K-1 @ -10 °C 118 $\pm$ 8 W m-1 K-1 @ -40 °C	
thermocouples type E	AET 05/200/2E TAT25/2m/ZEH/MFM.E by ES Electronic Sensor GmbH	
graphite heating foil	SIGRAFLEX® F02012TH by SGL Carbon SE	
high current test probes	HSS-120 305 300 S 30 02 M by INGUN Prüfmittelbau GmbH	
gap filler	TGF-R0500-SI by HALA Contec GmbH & Co. KG	

3.3   Tube inserts

Since most of the pressure drop and heat transfer models for porous inserts have been proposed for sponges so far (compare Section 2.3.3 and Section 2.5.3), two different kinds of metal sponges are chosen as exemplary inserts. Due to their potential for use in technical heat exchangers, hiTRAN® wire matrix elements are also being investigated. The inserts and the position in the test section during the tests are explained in the following subsections.

3.3.1   Metal sponges

A 10 ppi and a 20 ppi copper sponge were introduced into the test section and the adjacent sight glass. The copper sponges were purchased from the Fraunhofer Institute for Manufacturing Technology and Advanced Materials

(IFAM) in Dresden. Cylinders (Figure 3.4 (a)) were cut from several blocks produced using replication technology [124]. Due to manufacturing constraints, a sponge consists of several pieces of approx. 50 mm length. The struts are triangular (Figure 3.4 (b)) and contain large pores due to the template and small pores due to the sintering process (Figure 3.4 (c)).

(a)   (b)   (c)
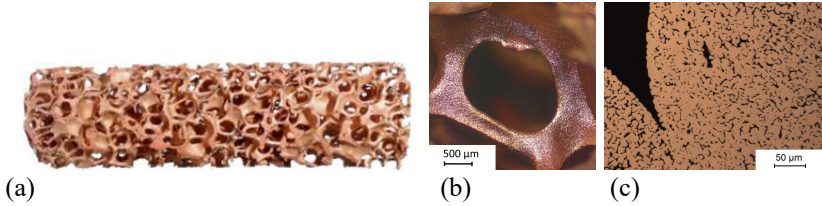
**Figure 3.4:** (a) sponge sample; (b) micrograph of window; (c) microsection of strut.

Table 3.3 lists the average properties of the sponges. A more detailed description of the properties and the measurement methods can be found in a publication of the experimental data, compare Weise et al. [96].

A coarse sieve adjacent to the sight glass fixes the sponges, which lie in the test section with a clearance fit of <70 µm. Figure 3.5 and Figure 3.6 illustrate the positions of the individual sponges.

In case of the 10 ppi sponge, the copper sponge was framed by a transparent plastic sponge to observe the flow pattern in the sight glass and to guarantee a developed flow pattern in the planes of measurement (total length of copper sponge samples, $L_{Cu} = 200.2$ mm). The plastic sponge was created by 3D printing using a model similar to the 10 ppi copper sponge. In case of the 20 ppi sponge, the sight glass and the inlet of the test section were filled with metal sponges since the manufacture of transparent plastic sponges with that pore density was not possible at that time. To exclude the influence of entrance effects on the pressure drop and heat transfer measurement, two different entrance lengths are investigated for each sponge type (see Table 3.4).

Table 3.3: Geometric properties of sponge samples in test section. The averaged value, the maximum deviation of the average of different samples ($^+_-$), the uncertainty of the method, 2σ, the standard deviation s, and the standard deviation of the mean, s_x, where applicable.

	10 ppi	20 ppi
	13.96 $^{+0.02}_{-0.03}$ mm	13.97 $^{+0.02}_{-0.02}$ mm
	$2\sigma =0.05$ mm	$2\sigma =0.05$ mm
total porosity, ψ	90.7 $^{+0.4}_{-0.3}$ %	89.7 $^{+0.8}_{-0.4}$ %
	$2\sigma =0.07\%$	$2\sigma = 0.07\%$
open porosity, ψ_o (gas pycnometry)	87.6 $^{+0.2}_{-0.2}$ %	86.8 $^{+0.2}_{-0.2}$%
	$2\sigma =0.41\%$	$2\sigma =0.41\%$
open porosity, ψ_o (μCT reconstruction)	85.5%	84.5%
secondary porosity ($V_{secondary\ pores}/V_{st}$)	8.4%	8.4%
	$2\sigma =3.4\%$	$2\sigma =3.4\%$
mean strut diameter, d_{st}	450μm	275 μm
	$s_x =16$ μm; $s =103$ μm	$s_x = 14$ μm;$s = 72$ μm
mean window diameter, d_w	1561 μm	1027 μm
	$s_x = 63$ μm; $s = 332$ μm	$s_x = 53$ μm; $s = 238$ μm
specific surface area, $S_v = \dfrac{A}{V_{cylinder}}$	sample V: 952 m^{-1}	sample X: 1375 m^{-1}
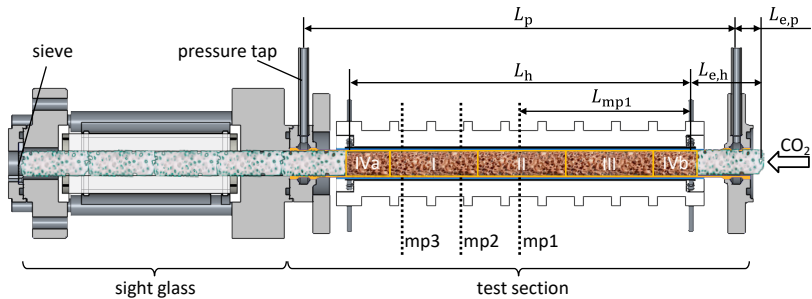
Figure 3.5: Positions of the sponge pieces in case of the 10 ppi sponge. More plastic sponges were inserted upstream to evaluate entrance effects. Relevant lengths are specified in Table 3.4.
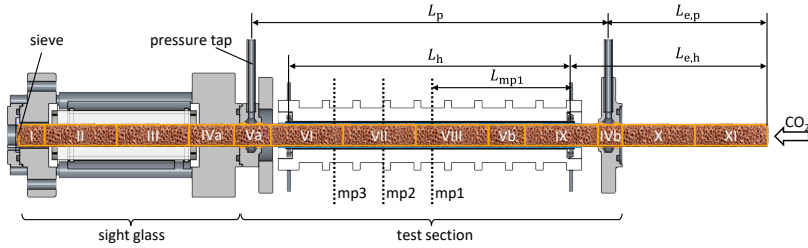
Figure 3.6: Positions of the sponge pieces in case of the 20 ppi sponge. Sponge sample X and XI were inserted to evaluate entrance effects. Relevant lengths are specified in Table 3.4.

Table 3.4: Sponge samples integrated into the test section and entrance length with respect to the measurement plane 1 ($L_{e,h} + L_{mp1}$) and the inlet pressure tap ($L_{e,p}$).

sponge type and measurement mode	sponge samples (copper)	length upstream of mp1 ($L_{e,h} + L_{mp1}$) / mm	length upstream of entrance pressure tap ($L_{e,p}$) / mm
10 ppi, shortened	I-IV	136	12
10 ppi, basis	I-IV	333	209
20 ppi, shortened	I-IVb	133	9
20 ppi, basis	I-XI	233	109

3.3.2   Wire matrix inserts

The hiTRAN® wire matrix element investigated was provided by CALGAVIN Ltd. [33]. It consists of stainless-steel wire windings interwoven in two twisted wires. The diameter of the twisted wire is 1.2 mm, the diameter of the wire used for the windings is 0.6 mm. The porosity of this element is 93.9%, and the specific surface area is approximately 400 m^{-1}. Owing to the manufacturing process, the windings of the element are folded in one direction so that the elements can be drawn into the test section and the pre-evaporator. Due to the spring effect of the wire windings, the wire matrix element is force-locked to the wall. After installation, the hiTRAN® wire matrix element completely fills the heated zone of the test section and the sight glass and 60 cm upstream of the inlet pressure tap. Figure 3.7 shows a photo of the hiTRAN® wire matrix element used and the flow direction of CO_2.

Figure 3.7: Image of the hiTRAN® wire matrix element applied in the test section. The flow direction against the inclined windings is indicated by the arrow.

3.4 Experimental procedure and evaluation

The target values for the assessment of flow boiling in porous structures are the adiabatic and diabatic pressure drop per unit length, the heat transfer coefficient and the flow pattern. For comparison with empty tube data, the following operating conditions must also be specified: mass flux, vapor quality, saturation pressure/saturation temperature and heat flux. The Sections 3.4.1 to 3.4.8 focus on the derivation of these quantities from the raw data (temperatures, pressures, mass flow, power). The raw data acquisition is performed with a LabVIEW routine in steady state. Within 50 s, 40 data points are recorded from which the average value and standard deviation are calculated. Steady state was ensured by a start-up time of 40 minutes and a waiting time of at least 3 minutes after small changes. Furthermore, all operating conditions averaged over 10 s had to be constant within 3 minutes within a specified range in order to account for strongly fluctuating flow ($\Delta \dot{m}_0 < 1$ kg m^{-2} s^{-1}, $\Delta p_{LV} < 0.02$ MPa, $\Delta \dot{x} < 0.01$, $\Delta \Delta p < 0.1$ kPa (10 ppi) or < 0.7 kPa (20 ppi)). To check the validity of these conditions, a repeat measurement was performed after 5 minutes.

Table 3.5 summarizes the range of operating conditions investigated and discussed in this thesis. Experimental results and the measurement uncertainty determined according to the "Guide to the expression of uncertainty in measurement (GUM)" [125] for sponges are reported in the publication of the experimental data, compare Weise et al. [75,96] in an open-source database. "The standard uncertainties of the measurands […] are estimated by means of a type

B evaluation. The individual evaluation is based on the manufacturer's specifications of the measurement device (compare Table 3.1) or calibration device, on preliminary tests, or – for the temperature distribution in the test section – on numerical calculations (see Appendix B.3). A similar procedure is applied to estimate the standard uncertainty of geometrical and material properties such as the thermal conductivity of the tube wall, the thermal transmittance of the insulation or the dimension of the test section. […] The expanded combined standard uncertainty with a coverage factor of $k = 2$ describing a confidence level of 95% is calculated from these basic standard uncertainties by error propagation" [96]

Table 3.5: Overview of the operating conditions of two-phase pressure drop heat transfer measurements studied and discussed in this work.

structure	type of measure- ment	saturation pressure / MPa	reduced pressure	superficial mass flux / kg m^{-2} s^{-1}	vapor quality /%	averaged heat flux / kW m^{-2}
sponge, 20 ppi	pressure drop, flow pattern	1.2; 2.65	0.16; 0.36	25 - 150	0.07 - 0.98	< 0.7
sponge, 20 ppi	flow boiling heat transfer	1.2; 1.9; 2.65	0.16; 0.26; 0.36	25 - 125	0.10 - 0.98	5.3 - 51
sponge, 10 ppi	pressure drop, flow pattern	1.2; 2.65	0.16; 0.36	25 - 150	0.05 - 0.98	< 0.7
sponge, 10 ppi	flow boiling heat transfer	1.2; 1.9; 2.65	0.16; 0.26; 0.36	25 - 125	0.03 - 0.96	3.5 - 65
hiTRAN® wme	pressure drop, flow pattern	1.2; 2.65	0.16; 0.36	25 - 200	0.06 - 0.98	< 0.7
hiTRAN® wme	flow boiling heat transfer	1.2; 2.65	0.16; 0.36	25 - 190	0.10 - 0.92	5.3 - 49

3.4.1 Mass flux

As defined in Section 2.2 , Eq. (2.1), the (superficial) mass flux, $\dot{m}_0$, is calculated from the mass flow rate, $\dot{M}$, and the cross-sectional area, A, of the empty tube. The (interstitial) mass flux in the inserts, $\dot{m}$, is related to the cross-sectional area of vapor and liquid. The mass flow rate is measured in the super-cooled flow immediately after the bypass branch by a Coriolis mass flow meter (Promass F 60 by Endress+Hauser AG).

The superficial mass flux allows both the agreement with single-phase pressure drop correlations used to calculate the two-phase pressure drop (compare Section 2.3.1 and 2.3.3) and the comparison of the heat transfer coefficient in different structures at the same mass flow rate. The interstitial mass flux ensures conformity with the void fraction correlations (see Section 2.2) and the single-phase heat transfer correlation by Bianchi et al. (see Section 2.5.2).

The measurement uncertainty (k=2) of the superficial mass flux is 0.4 kg m^{-2} s^{-1} for a mass flux of 25 kg m^{-2} s^{-1} and 1.1 kg m^{-2} s^{-1} for 200 kg m^{-2} s^{-1}. It is influenced by the uncertainty of the mass flow rate measurement, i.e., the uncertainty of the mass flow meter (compare Table 3.1), and the uncertainty of the tube diameter determined by an internal micrometer with a standard uncertainty of $\pm 0{,}01$ mm.
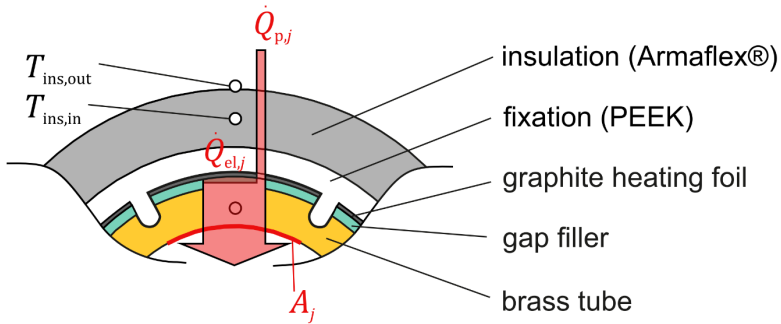
3.4.2 Heat flux

The segmentation of the test section allows to set two different thermal boundary conditions. Firstly, the power of the individual segments can be controlled so that the wall temperature is the same in all segments ("constant wall temperature"). Secondly, the same heat flux can be set in all segments ("constant heat flux"). In both cases, the local heat transfer coefficient, $\alpha_{i,j}$, i.e., the heat transfer coefficient in measurement plane i at segment j, is comparable for the same local heat flux, $\dot{q}_j$. A stratified flow pattern causes the local heat transfer coefficients to vary considerably along the tube circumference. In this case, a constant heat flux boundary condition induces high temperature differences in the tube wall along the tube circumference. This leads to azimuthal heat flux,

which complicates the accurate determination of the local heat transfer coefficient. Consequently, a constant wall temperature boundary condition is set in the experiments.

Figure 3.8 illustrates the calculation of the local heat flux in one segment j. The total heat transferred is composed of the electrical power converted in the heating foil, $\dot{Q}_{el,j}$, and the heat introduced from the environment, $\dot{Q}_{P,j}$. The electrical power is calculated taking into account the power dissipation in the connection lines by the factor K_{diss}. The heat transfer from the environment is estimated by means of the thermal transmittance, kA, and the temperatures measured in the insulation, $T_{ins,in}$ and $T_{ins,out}$. The thermal transmittance has been determined under vacuum conditions and validated using single-phase measurements (see Section 3.5). The heat transfer area of segment j is one-sixth of the tube's inner surface in the heated section. It is calculated the tube's inner diameter, D_i, and the heated length, L_h.

Figure 3.8: Detail of the cross-sectional view of the test section to illustrate the calculation of the heat flux in segment j. The representation of the fixation and the insulation is not true to scale.

Thus, Eq. (3.1) determining the local heat flux is derived from the measured quantities.

$$\dot{q}_j = \frac{\dot{Q}_{el,j} + \frac{1}{6}\dot{Q}_P}{A_j} = \frac{K_{diss}\,P_{el,j} + \frac{1}{6}kA\big(T_{ins,out} - T_{ins,in}\big)}{\frac{\pi}{6} \cdot D_i \cdot L_h} \tag{3.1}$$

The average heat flux, $\dot{q}$, is calculated by averaging the local heat flux. Due to different flow patterns and thus different local heat transfer coefficients, flow boiling tests with the boundary condition "constant temperature" are not comparable for the same average heat flux. Furthermore, it should be noted that the local heat flux, $\dot{q}_j$, is neither a valid comparative value for the pressure drop, since the distance between the pressure taps does not correspond to the heated length, L_{h}.

The measurement uncertainty of the heat flux is mainly influenced by the uncertainty of the transmittance of the test section insulation and by the uncertainty of the factor K_{diss}. The uncertainty of the transmittance influences the measurement uncertainty particularly at low heat fluxes, the uncertainty of the factor K_{diss} at high heat fluxes. In summary, the relative measurement uncertainty ($k = 2$) of the local heat flux is less than 20% for heated segments.

3.4.3   Saturation pressure and saturation temperature

To calculate the saturation pressure in the respective measurement plane, the course of the pressure between the pressure taps at the inlet and at the outlet needs to be approximated. At constant total mass flux, the pressure course depends mainly on the vapor quality, which changes linearly in the test section. It will be shown in Section 4.1 that the pressure drop in tubes with porous inserts is a quadratic function of the vapor quality. However, the second derivative of this function is small. Moreover, the vapor quality changes little in the test section ($\Delta \dot{x} < 35\%$ for a mass flux of 25 kg m^{-2} s^{-1} and $\Delta \dot{x} < 10\%$ for mass fluxes ≥ 125 kg m^{-2} s^{-1}). These two facts justify a linear interpolation of the saturation pressure between the pressure taps. Therefore, the saturation pressure, $p_{\mathrm{LV},i}$, in the respective measurement plane i is calculated by Eq. (3.2).

$$p_{\mathrm{LV},i} = p_{\mathrm{LV,ts,in}} + \frac{L_i}{L_{\mathrm{p}}} \Delta p \qquad \text{(3.2)}$$

$p_{\mathrm{LV,ts,in}}$ is the static pressure measured at the inlet of the test section (ts), L_i is the distance between the inlet pressure tap and the measurement plane i, L_{p} is

the distance between the two pressure taps and Δp is the measured pressure difference (compare Figure 3.2).

The saturation temperature, $T_{LV,i}$, is calculated from the respective saturation pressure, $p_{LV,i}$, using the equation of state of CO_2 according to Span and Wagner [126].

3.4.4 Vapor quality

The vapor quality, $\dot{x}_i$, in the respective measurement plane i is determined by means of an enthalpy balance, assuming a thermodynamic equilibrium. As explained in Section 2.5.1, this assumption is valid for a wide vapor quality range. The control volume comprises the pre-evaporators and the test section up to the respective measurement plane as well as unheated, insulated tube sections (compare Figure 3.1).

The refrigerant enters the control volume sub-cooled, i.e., its specific enthalpy is a function of the pressure and temperature at this point, $h_{L,in} = f(T_{in}, p_{in})$. The liquid enthalpy and the enthalpy of vaporization in the measurement plane, $h_{L,i}$ and $\Delta h_{LV,i}$, depend exclusively on the saturation pressure in the respective plane, $p_{LV,i}$. The saturation pressure is determined by linear interpolation (compare Section 3.4.3). The heat supplied by the pre-evaporators and the respective part of the test section as well as the parasitic heat transfer from the environment through the insulation are considered, i.e., $\sum \dot{Q} = \sum \dot{Q}_{el} + \sum \dot{Q}_P$. Similar to the calculation of the heat flux in the test section (see Section 3.4.2), the power dissipation in the connection lines and the thermal transmittance of the insulation of the pre-evaporators are taken into account. Eq. (3.3) summarizes the enthalpy balance.

$$\dot{x}_i = \frac{\sum \dot{Q} - \left(h_{L,i} - h_{L,in}\right) \cdot \dot{M}}{\Delta h_{LV,i} \cdot \dot{M}} \tag{3.3}$$

A validation of the vapor quality was carried out on the basis of single-phase measurements, in which the enthalpy difference was calculated redundantly via the heat supplied and via the temperature differences at various points in

the test circuit. The results were included in the measurement uncertainty evaluation. The measurement uncertainty analysis of the vapor quality revealed a particularly large uncertainty for small mass flows, which is why measurements at the KIT/TVT flow boiling test facility with mass fluxes below 25 kg m^{-2} s^{-1} are subject to large uncertainties. The insulated, unheated tube sections contribute most to the measurement uncertainty, as their thermal transmittance is difficult to estimate. The relative measurement uncertainty ($k = 2$) at a mass flux of 25 kg m^{-2} s^{-1} and a saturation pressure of 1.2 MPa is 5%. At a mass flux of 150 kg m^{-2} s^{-1} and a saturation pressure of 2.65 MPa the relative uncertainty reduces to 1%.

3.4.5 Wall temperature

To calculate the heat transfer coefficient, knowledge of the temperature at the inner tube wall, T_W, is necessary. A direct measurement of this temperature is not possible at the current state of the art without influencing the fluid flow. Therefore, T_W is extrapolated from the temperature T_{tc}, which is measured by thermocouples (tc) soldered into the tube wall, using Eq. (3.4). This equation is based on the assumption of one-dimensional heat conduction in a cylindrical shell segment. This is done for each segment j in each measurement plane i.

$$T_{W,i,j} = T_{tc,i,j} - \frac{6 \cdot \dot{Q}_j \cdot \ln\left(\frac{D_{tc,i}}{D_i}\right)}{2\pi \cdot L_h \cdot \lambda_{ts}} \tag{3.4}$$

Eq. (3.4) takes into account the heat transferred through the respective segment, $\dot{Q}_j$, according to Section 3.4.2. The diameter $D_{tc,i}$ is related to the thermocouple tips in each measurement plane i. D_i is the inner diameter of the tube, L_h is the heated length and λ_{ts} corresponds to the thermal conductivity of the test section. The thermal conductivity of the test section material was determined experimentally, compare Appendix B.2.

In addition to the measurement uncertainty of the thermocouples, the inaccuracy due to the simplification of the complex test section geometry to a hollow cylinder is also taken into account. To estimate the deviation, the temperature

distribution in the test section was simulated with STAR-CCM+ under differ-ent boundary conditions, i.e., constant heat flux and heat flux varying for each segment. The inaccuracy due to simplification is considered in the measure-ment uncertainty with a standard deviation ($k = 1$) estimated to be 0.13 K (see Appendix B.3). This is the largest contribution to the overall measurement un-certainty of the wall temperature.

3.4.6   Pressure drop

The pressure drop per unit length corresponds to the measured pressure drop, Δp, related to the distance between the pressure taps, L_p.

The heat flux, $\dot{q}^*$, which is given for comparison purposes along with the pres-sure drop results, is calculated by dividing the total heat transferred in the test section by the inner surface of the tube between the pressure taps. Due to the test section layout, the heat flux related to the heated tube area, $\dot{q}$, would lead to wrong results if used in Eq. (2.14).

The measurement uncertainty ($k = 2$) of the pressure drop is 0.3 kPa m^{-1}, and thus the relative value is higher for low pressure drops. It is basically influ-enced by the uncertainty of the differential pressure measurement, the uncer-tainty of the distance between the pressure taps being negligible.

3.4.7   Flow pattern

The two-phase flow in the sight glass was observed by high-speed video re-cording (KODAK Motion Corder Analyzer, CCD b/w camera, 500 fps). Partly the videos were characterized by image analysis. MATLAB was used to cal-culate the standard deviation of each pixel of all frames of a high-speed video (see Figure 3.9). Since both liquid and gaseous CO_2 are transparent and only the phase boundary is clearly visible in the videos, the standard deviation is a qualitative measure for the fluctuation of the phase boundary. The standard deviation thus obtained is normalized to gray scale values between 0 and 1 and

saved as an image. White (1) corresponds to strong fluctuations of the phase boundary and black (0) indicates no fluctuation.

$$\sigma(x,y) = \sqrt{\frac{1}{n-1}\sum_{t=1}^{n}\left(P_t(x,y) - \bar{P}(x,y)\right)^2}$$
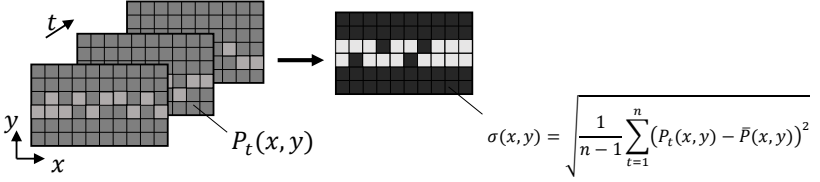
Figure 3.9: Schematic illustration of image processing to determine the position of the boundary layer according to a previous work, compare Weise et al. [127]. $P_t(x,y)$: pixel at the coordinates x, y of the frame captured at time t; $\sigma(x,y)$: standard deviation of the pixels at the coordinates x, y; $\bar{P}(x,y)$: arithmetic mean of all pixels at the coordinates x, y; n: number of frames.

Following the example of Kanizawa et al. [43] and Zhao et al. [44], the pressure and temperature fluctuations are evaluated in addition to the video image evaluation to judge the flow pattern. Moreover, the dependence of the local heat transfer coefficients on the heat flux and the relative magnitude of the local heat transfer coefficients are used to assess the wetting behavior.

3.4.8 Heat transfer

Eq. (3.5) is used to determine the local heat transfer coefficient, $\alpha_{\text{tp},i,j}$, of each segment j in measurement plane i. The heat flux in the segment, $\dot{q}_j$, (see Section 3.4.2), the temperature at the inner wall of the tube, $T_{\text{W},i,j}$, (see Section 3.4.5) and the saturation temperature of the respective measurement plane, $T_{\text{LV},i}$, (see Section 3.4.3) are included in the calculation.

$$\alpha_{\text{tp},i,j} = \frac{\dot{q}_j}{T_{\text{W},i,j} - T_{\text{LV},i}(p_{\text{LV},i})} \tag{3.5}$$

The circumferentially averaged heat transfer coefficient is determined in mp1 using Eq. (3.6).

$$\alpha_{\text{tp},1} = \frac{1}{6}\sum_{j}\alpha_{\text{tp},1,j} \tag{3.6}$$

To classify the relative measurement uncertainty ($k = 2$) of the local heat transfer coefficient, $u_{\alpha_{\text{tp},1,j}}/\alpha_{\text{tp},1,j}$, it is useful to categorize the operating conditions according to the heat flux and the temperature level, i.e., the saturation pressure. Table 3.6 lists for each category the result and the dominant contributions to the relative uncertainty. In view of these large values, it should be noted that the uncertainty presented refers to a comparison with another test section. However, if the measurement data are compared with measurement data obtained with the same test section but with a different or no insert, the uncertainties are significantly lower. This statement is plausible if one realizes that the main contributions to the uncertainty of the heat transfer coefficient are the uncertainty of the thermal transmittance of the insulation and the uncertainty of the power dissipation in the connection lines. Both the thermal transmittance and the power dissipation are constant for measurements with the same test section. Their contributions are therefore not relevant for a comparison of different measurements obtained with the same test section. Consequently, repeatability measurements (compare Section 3.5) are performed to determine the order of magnitude of the measurement uncertainty relevant for comparing different measurements obtained with the same test section.

Table 3.6: Classification of the relative measurement uncertainty ($k = 2$) of the local heat transfer coefficient ($u_{\alpha_{\text{tp},1,j}}/\alpha_{\text{tp},1,j}$).

	$p_{\text{LV}} \leq 1.2$ MPa	$p_{\text{LV}} \geq 1.9$ MPa
$\dot{q} < 15$ kW m^{-2}	$\frac{u_{\alpha_{\text{tp},1,j}}}{\alpha_{\text{tp},1,j}}$ exceeds 50% for several measurement points	$25\% < \frac{u_{\alpha_{\text{tp},1,j}}}{\alpha_{\text{tp},1,j}} < 50\%$
	Dominant contribution: uncertainty of the thermal transmittance of the insulation. A larger temperature difference between the fluid and the environment causes a larger relative uncertainty	
$\dot{q} > 15$ kW m^{-2}	$\frac{u_{\alpha_{\text{tp},1,j}}}{\alpha_{\text{tp},1,j}} < 25\%$ Dominant contribution: uncertainty of the power dissipation in the connection lines, described by K_{diss} Independent of $\dot{q}$, p_{LV} or other operating conditions ($\dot{m}, \dot{x}$).	

3.5   Validation and repeatability

For the validation of the new test section, both single-phase and two-phase tests were carried out before the porous structures were introduced. The results of the validation experiments were integrated into the measurement uncertainty evaluation.

To validate the heat transfer coefficient, the experimentally determined heat transfer coefficient of the single-phase flow is compared with established correlations according to chapter G1, VDI heat atlas [128]. Since the experimental Reynolds number, Re_{exp}, exceeds 4000 in all cases investigated, the corresponding local Nusselt numbers, Nu_{pred}, are calculated assuming turbulent flow (compare Gnielinski [129]). Eq. (3.7) and Eq. (3.8) give the equations for disambiguation using the inner tube diameter D_{i} and the heated length before measurement plane 1 including pre-evaporator 3, $L_{\mathrm{mp1}} + L_{\mathrm{pe3}}$.

$$Nu_{\mathrm{pred}} = \frac{(\xi/8) \cdot (Re_{\mathrm{exp}} - 1000) \cdot Pr_{\mathrm{exp}}}{1 + 12.7 \cdot \sqrt{\xi/8} \cdot (Pr_{\mathrm{exp}}^{2/3} - 1)} \left[1 + \frac{1}{3} \left(\frac{D_{\mathrm{i}}}{L_{\mathrm{mp1}} + L_{\mathrm{pe3}}} \right)^{2/3} \right] \qquad \textbf{(3.7)}$$

$$\xi = \left(1.8 \cdot \log_{10} Re_{\mathrm{exp}} - 1.5 \right)^{-2} \qquad \textbf{(3.8)}$$

Moreover, the experimental heat transfer coefficients and the corresponding experimental Nusselt numbers are determined according to two different methods. For method A, the heat flux is calculated according to Eq. (3.1). For method B, the heat flux is determined by means of an enthalpy balance between mp1 and mp2 using the wall temperature in the respective measurement plane. Method B is based on the assumption that the temperature difference in the wall corresponds to the temperature difference of the bulk flow. For both methods, the temperature of the bulk flow is estimated from the temperature measured upstream of pre-evaporator 3 and the heat input in pre-evaporator 3 and the test section. This leads to a relatively large measurement uncertainty of this evaluation. Figure 3.10 shows that the experimentally determined Nusselt number is nevertheless in good agreement with the established correlation. The larger variation of the experimental results calculated according to method B

is due to the temperature difference between mp1 and mp2 in the order of magnitude of 0.1 K, which is close to the measurement uncertainty.
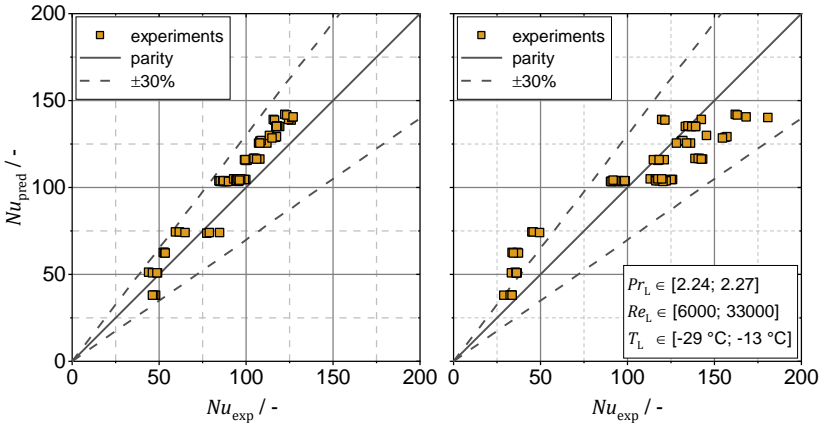

Figure 3.10: Comparison of experimentally determined heat transfer (here: Nusselt number) and heat transfer coefficient predicted by single phase heat transfer correlations. Left: experimental heat transfer based on heat input (method A), right: experimental heat transfer based on temperature difference between mp1 and mp2 (method B).

The repeatability of the heat transfer coefficient and the pressure drop measurements was verified by repeating the measurements under nominally identical operating conditions on different days within two years. The evaluation of the results in Figure 3.11 to Figure 3.14 for a mass flux of 150 kg m^{-2} s^{-1} and a vapor quality of 50% allows following two conclusions.

First, the repeatability is significantly better than the measurement uncertainty for these operating conditions. The result is transferable to other operating conditions and means that the comparison of two measurements with the same test section and test facility but different inserts is better than predicted by means of the GUM-determined measurement uncertainty.

Secondly, no clear trend in the change of the measurement results could be determined. For heat transfer measurements at 1.2 MPa (see Figure 3.11), no deviation between the measurement series can be observed. In contrary, for 2.65 MPa, heat transfer measurements in July 2018 are slightly lower than previous measurements (see Figure 3.12).
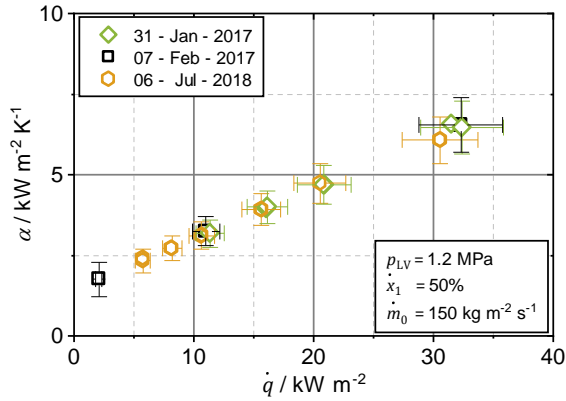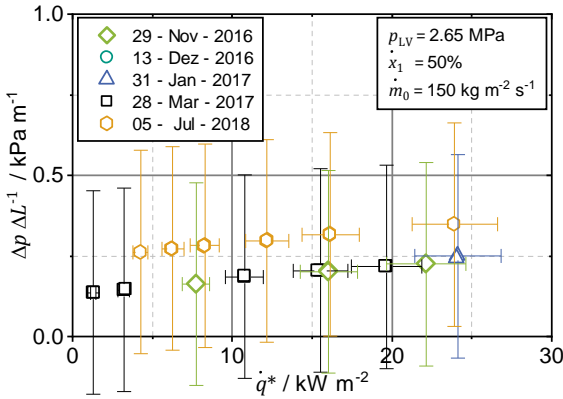
Figure 3.11: Averaged heat transfer coefficients of two-phase flow boiling in the empty test section under nominally identical operating conditions, measured on different days over a period of one year for a saturation pressure of 1.2 MPa.
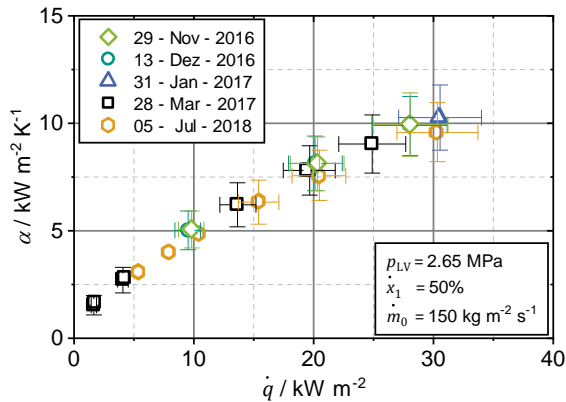

Figure 3.12: Averaged heat transfer coefficients of two-phase flow boiling in the empty test section under nominally identical operating conditions, measured on different days over a period of two years for a saturation pressure of 2.65 MPa.
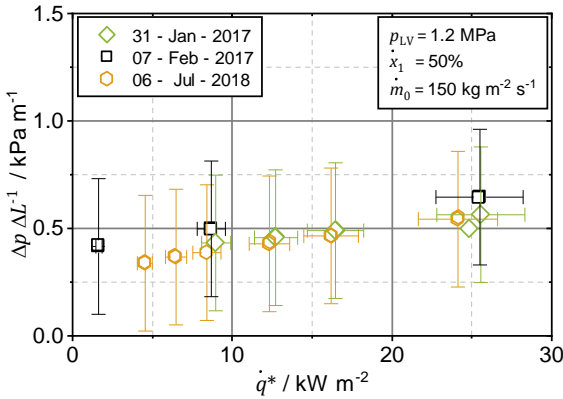
Figure 3.13: Pressure drop per unit length of two-phase flow in the test section under nominally identical operating conditions, measured on different days over a period of one year for a saturation pressure of 1.2 MPa.

Figure 3.14: Pressure drop per unit length of two-phase flow in the test section under nominally identical operating conditions, measured on different days over a period of two years for a saturation pressure of 2.65 MPa.

For pressure drop measurements at 1.2 MPa (see Figure 3.13), measurements in February 2017 are slightly higher than the other measurements, while at 2.65 MPa measurements in July 2018 are slightly increased (see Figure 3.14). Therefore, for both heat transfer and pressure drop measurements, a systematic

variation in the measurement results over time can be excluded, as it is only observed at one pressure level in each case. Consequently, a random measurement error can be assumed. For heat transfer measurements, the random measurement error can be attributed to operating parameters that cannot be repeated exactly (especially mass flux, vapor quality, and heat flux distribution). For pressure drop measurements in empty tubes, the measured values are very close to the lower range of the differential pressure transducer. Thus, the zeroing of the transducer before each measurement series may cause the observed fluctuations.

Figure 3.15 and Figure 3.16 show a comparison of the pressure drop and the average heat transfer coefficient determined with the new test section with data by Schael [24]. For heat fluxes below 30 kW m^{-2}, both data sets agree within the scope of the measurement uncertainty.
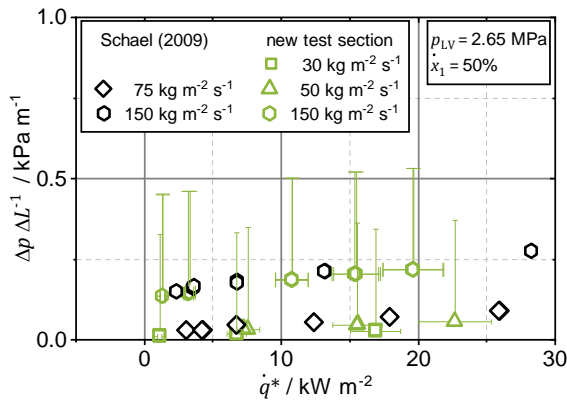
Figure 3.15: Comparison of the pressure drop per unit length measured with the new test section (without inserts) with data by Schael [24] at a saturation pressure of 2.65 MPa and a vapor quality of 50%. The mass flux was varied.
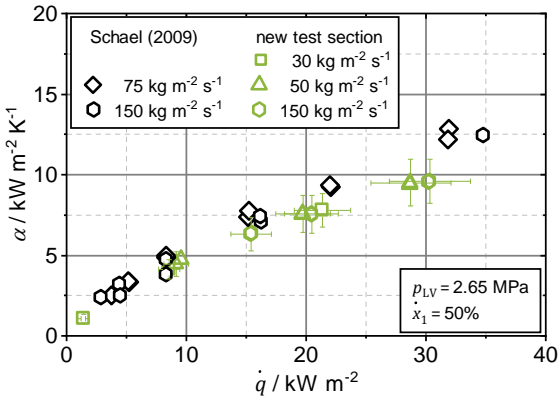
Figure 3.16: Comparison of the average heat transfer coefficient measured with the new test section (without inserts) with data by Schael [24] at a saturation pressure of 2.65 MPa and a vapor quality of 50%. The mass flux was varied.

In summary, the validity, repeatability and comparability of the test section to the test section by Schael [24] was demonstrated. Consequently, the test section can be used to test the hypothesis of this thesis.

4 Results and discussion

In the following the experimental results of two-phase flow in tubes with inserts regarding pressure drop, flow pattern, and heat transfer are discussed separately. The experimental data are published as open-source databases for sponge inserts [75,96]. The analysis of the experimental data uses own publications [2,23,127] as a starting point but goes beyond the findings there and focuses on testing the hypothesis of this work.

For reasons of clarity, only every second error bar is displayed in the diagrams. If not indicated otherwise, error bars correspond to the extended measurement uncertainty (k=2).

4.1 Pressure drop

Experimental results of both adiabatic and diabatic pressure drop measurements in porous inserts are discussed to identify promising model approaches. First, any influence of entrance effects on the experimental results is excluded. Afterwards, an adaption of the Forchheimer model to two-phase flow is sought. At last, the influence of heat input on the pressure drop is evaluated.

4.1.1 Entrance effects

Entrance effects - such as the formation of the flow pattern or stagnation point flow at the leading edge of the inserts - can influence the pressure drop. To exclude the influence of stagnation point flow, the inserts were filled into the test loop upstream of the test section. In order to ensure that the experimental results are not influenced by the formation of the flow pattern, the length of the inserts before the inlet pressure tap, $L_{e,p}$ (see Section 3.3), needs to be sufficiently large. In case of hiTRAN® wire matrix elements, this is ensured by an

extremely long entrance length (60 cm). Unlike the production of the hi-TRAN® wire matrix elements, the manufacturing of the sponge inserts is complex and expensive. Therefore, a shorter $L_{e,p}$ had to be realized (see Table 3.4). To ensure a sufficient length, $L_{e,p}$ was varied for the sponge inserts (basis and shortened) and the measurements were compared. Figure 4.1 shows the pressure drop for two different sponge lengths before the inlet pressure tap for the 20 ppi sponge.
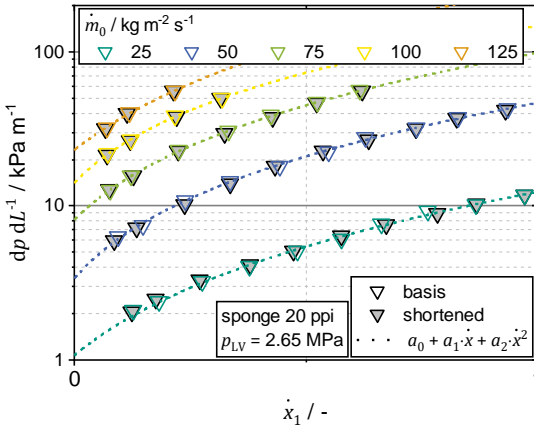
Figure 4.1: Adiabatic pressure drop per unit length as a function of the vapor quality in mp1, $\dot{x}_1$, for different lengths of sponge upstream of the inlet pressure tap, $L_{e,p}$. Polynomial fits (dotted lines) are applied to the basis measurement ($L_{e,p} = 109$ mm).

A direct comparison of the experimental results of the pressure drop of the basis and the shortened configuration is not possible because the vapor qualities vary slightly between the measurements and the pressure drop is strongly dependent on the vapor quality. Consequently, to interpret the data, the shortened configuration is indirectly compared with the bases case. For this purpose, the relative deviation of the measured data to 2nd order polynomial fits ($a_0 + a_1 \cdot \dot{x}_1 + a_2 \cdot \dot{x}_1^2$) of the basis case data are calculated. The polynomial fits are illustrated in Figure 4.1. The median, the 25th percentile, and the 75th percentile of this relative deviation are shown Figure 4.2 for both inlet lengths for the 20 ppi sponge and the 10 ppi sponge.
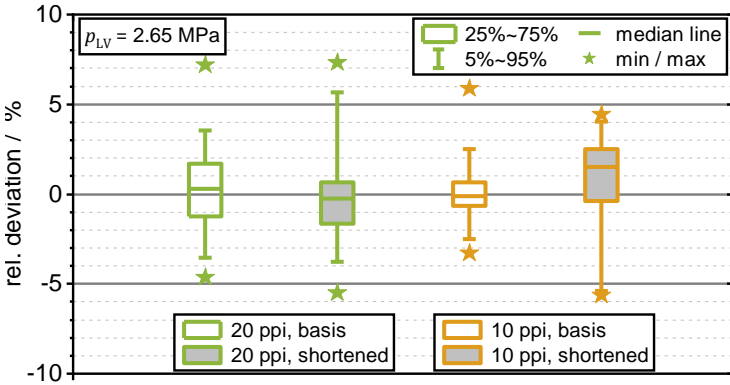
Figure 4.2: Statistics of the relative deviation of adiabatic pressure drop data from the polynomial fit of the basis data. For the polyn omial fit see Figure 4.1.

The statistical characteristics are almost identical for both inlet lengths. Consequently, the inlet length and thus the formation of the flow pattern has no influence on the measured pressure drop in the investigated parameter range.

4.1.2   Adiabatic pressure drop

To investigate the dependence of the pressure drop on mass flux, the influence of the vapor quality is eliminated by interpolating data points at the vapor qualities $\dot{x}_1 = 0.25$, $\dot{x}_1 = 0.5$, and $\dot{x}_1 = 0.75$ for each mass flux according to 2nd order polynomials. The 2nd order polynomials describe the data sufficiently well, since the relative absolute deviation of the measured data from the polynomials is less than 5% in 90% of all cases (compare Figure 4.2, reference case $L_{e,p} = 109$ mm). In Figure 4.3 the interpolated data points are shown together with two 2nd order polynomials ($b \cdot \dot{m}_0{}^2$ and $b_1 \cdot \dot{m}_0 + b_2 \cdot \dot{m}_0{}^2$), exemplary for a saturation pressure of 2.65 MPa and a vapor quality of 50%. The latter polynomial is consistent with the observation that pressure drop of single-phase flow through porous inserts is typically described by the Darcy-Forchheimer equation (see Eq. (2.7) in Section 2.3.1). The first polynomial resembles asymptote of the Darcy-Forchheimer equation for high mass fluxes, namely the Forchheimer term.
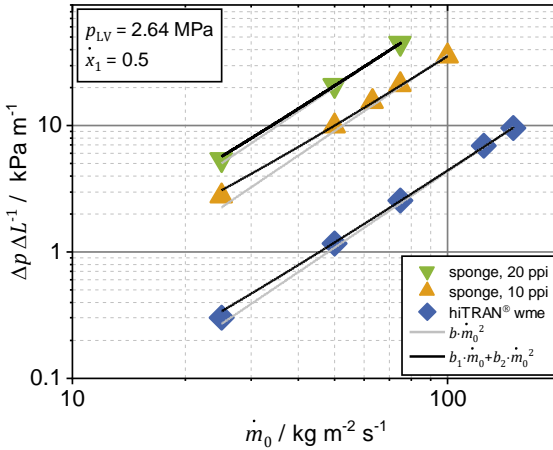
Figure 4.3: Adiabatic pressure drop per unit length as a function of mass flux for different inserts for a vapor quality of 50% and a saturation pressure of 2.65 MPa. Data points were calculated according to second-order polynomials.

The pressure drop dependency on the mass flux can be described well by a 2nd order polynomial ($b_1 \cdot \dot{m}_0 + b_2 \cdot \dot{m}_0{}^2$). The relative deviation of most data points (90%) is less than 3%. For low mass fluxes, the asymptote $b \cdot \dot{m}_0{}^2$ deviates significantly from the experimental results. However, for high mass fluxes ($\dot{m}_0 \geq 50$ kg m^{-2} s^{-1} for sponges and $\dot{m}_0 \geq 75$ kg m^{-2} s^{-1} for hiTRAN$^{®}$ wire matrix elements) the relative deviation of most data points (90%) from the asymptote $b \cdot \dot{m}_0{}^2$ is less than 5%.

The adaption of the Darcy-Forchheimer equation to a two-phase flow could reveal the dependence on the saturation pressure and the vapor quality, but is not trivial. The saturation pressure influences the fluid properties, i.e., the kinematic viscosity, ν, and the density, ρ.

The kinematic viscosity mainly influences the linear component of the Darcy-Forchheimer equation. There is disagreement in the literature especially about the modeling of the kinematic viscosity [45]. However, the flow velocities investigated in this thesis are too high to allow a reliable statement about the model to be used. This inadequacy would impair all further investigations. In

order to correctly identify the trends at least at high mass fluxes, the measurement data are thus limited to mass fluxes ≥ 50 kg m^{-2} s^{-1} (≥ 75 kg m^{-2} s^{-1} for hiTRAN® wire matrix elements) to keep the influence of the linear component as low as possible and still maintain enough measuring points for a meaningful analysis.

Based on this consideration the hypothesis whether the pressure gradient at high mass fluxes can be described by Eq. (4.1), an adaption of the Forchheimer equation to two-phase flow, shall be tested.

$$\frac{dp}{dL} = \beta \cdot f(\rho_{\mathrm{L}}, \rho_{\mathrm{V}}, \dot{x}) \cdot \dot{m}_0^2 \qquad \textbf{(4.1)}$$

Consequently, all relevant pressure drop data are divided by the square of the mass flux, $\dot{m}^2$, and the single-phase Forchheimer coefficient, β, determined experimentally for the 20 ppi sponge and the hiTRAN® wire matrix elements.

Figure 4.4 illustrates this quotient, i.e., $f(\rho_{\mathrm{L}}, \rho_{\mathrm{V}}, \dot{x})$, as a function of the vapor quality for 20 ppi sponge and hiTRAN® wire matrix elements. The form factor of the 10 ppi sponge is fitted accordingly (see Figure 4.5). For orientation, the reciprocal values of the liquid density and the vapor density are shown. The connecting line between these two values corresponds to the model of the homogeneous density. Five important results can be derived from these two figures.
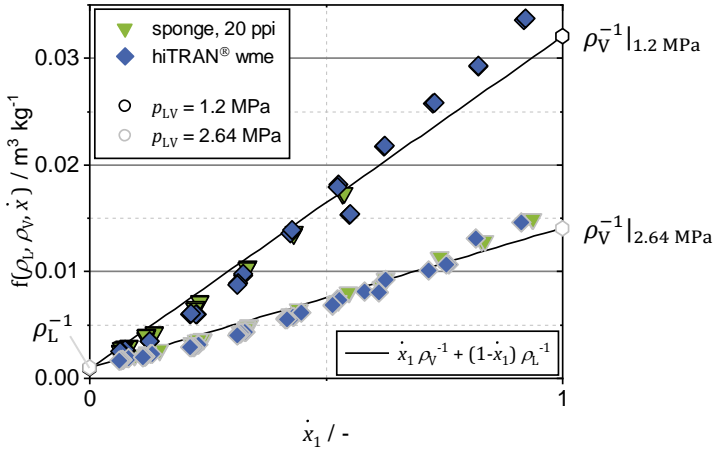
Figure 4.4: $f(\rho_L, \rho_V, \dot{x})$ as a function of the vapor quality for the 20 ppi sponge insert and the hiTRAN® wire matrix element and saturation pressures. The reciprocal values of the liquid and the vapor density and the homogeneous model serve for orientation.
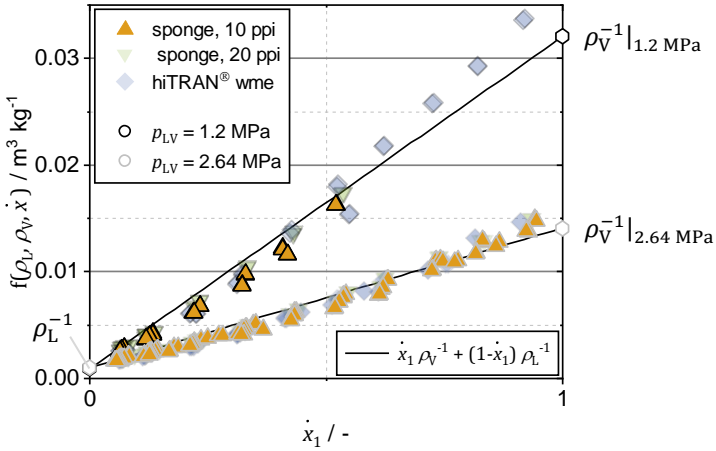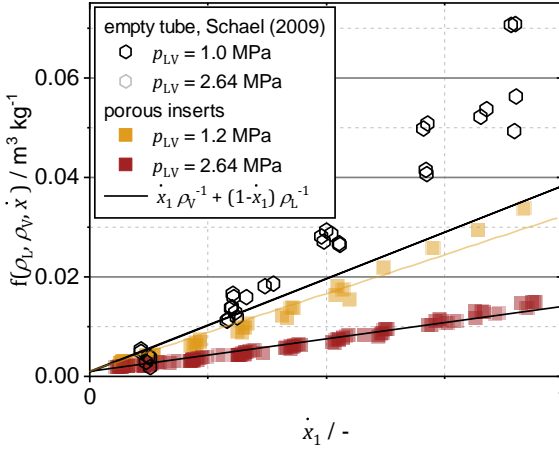

Figure 4.5: $f(\rho_L, \rho_V, \dot{x})$ as a function of the vapor quality for the 10 ppi sponge inserts and saturation pressures. The reciprocal values of the liquid and the vapor density and the homogeneous model serve for orientation. For reference, the experimental results of the other inserts are included.

First, the dependence of the pressure drop on vapor quality and saturation pressure is identical for the 20 ppi sponge and the hiTRAN® wire matrix element. These two inserts are fundamentally different in their characteristic dimensions. The data set of the 10 ppi sponge can also be brought into agreement with the other two data sets if the Forchheimer coefficient is selected accordingly (see Figure 4.5).

Secondly, the dependence of the pressure drop on the vapor quality up to a vapor quality of 0.9 can be described by a 2nd order polynomial. At low vapor qualities, i.e., $\dot{x} < 0.5$, $f(\rho_{L}, \rho_{V}, \dot{x})$ is smaller than the values according to the homogeneous model. No justification for this behavior could be found within the scope of this work. At high vapor qualities, i.e., $\dot{x} > 0.8$, this function exceeds the values according to the homogeneous model. Reasons for this excess may be the increasingly different velocities of the vapor and liquid phases and the resulting stronger interactions between the two phases [67] at high vapor qualities.

Thirdly, the observed behavior is similar to the behavior in the empty tube. However, in the empty tube a deviation from the linear behavior is more pronounced, especially at high vapor qualities. This can be judged by comparing Figure 4.4 and Figure 4.5 to Figure 4.6. The latter shows the function $f(\rho_{L}, \rho_{V}, \dot{x})$ for experimental data of the empty tube by Schael [24]. Presumably, the inserts prevent a large difference in velocity between the two phases.

Figure 4.6: $f(\rho_L, \rho_V, \dot{x})$ as a function of the vapor quality for the empty tube. The experimental data by Schael [24] are divided by $2 \cdot 0.079 \cdot Re^{-0.25} \cdot \dot{m}^2 \cdot D_i^{-1}$ with $Re = \dot{m} \cdot D_i \cdot \bar{\mu}^{-1}$. The homogeneous viscosity, $\bar{\mu}$, is calculated according to McAdams' model [63]. For comparison, experimental data of the porous inserts are included. In case of $p_{LV} = 1.2$ MPa, which differs from the system pressure of the empty tube data, an additional line for the homogeneous model $(\dot{x}_1\rho_V^{-1} + (1 - \dot{x}_1)\rho_L^{-1})$ is also included.

This leads to the fourth finding, namely that the Forchheimer equation, evaluated with the homogeneous model (compare Eq. (4.2)) can reproduce the measured data at high mass fluxes with an acceptable accuracy, overestimating most datapoints (compare Figure 4.7). The Forchheimer coefficient can be determined most exactly experimentally by single-phase measurements and estimated by appropriate models for single-phase flow. For solid sponge inserts, the use of the models by Woudberg and Du Plessis [57] or Inayat et al. [58] combined with a specific surface measured by µCT scanning (see Table 2.2) is proposed [23].

$$\frac{dp}{dL} \approx \frac{dp}{dL}\bigg|_{\text{hom}} = \beta \cdot \left(\frac{\dot{x}}{\rho_V} + \frac{1 - \dot{x}}{\rho_L}\right) \cdot \dot{m}_0^2 \tag{4.2}$$
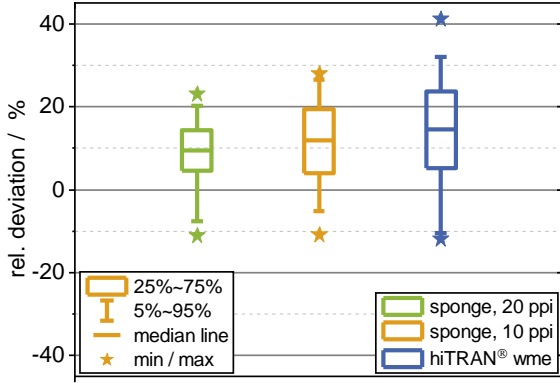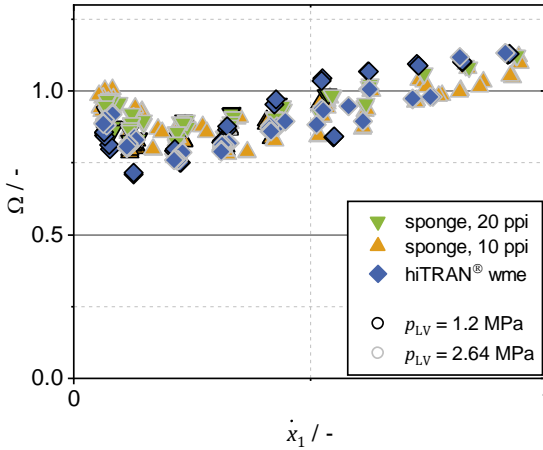
Figure 4.7: Box-plot of the relative deviation of data calculated by Eq. (4.2) from experimental pressure drop data (mass fluxes ≥ 50 kg m^{-2} s^{-1} for sponges and ≥ 75 kg m^{-2} s^{-1} for hiTRAN® wire matrix elements).

For a better description, a correction function, Ω, according to Eq. (4.3) can be applied. Such a procedure was proposed by Storek and Brauer [60] for empty tubes.

$$\frac{dp}{dL} = \Omega \cdot \frac{dp}{dL}\bigg|_{\text{hom}} \qquad (4.3)$$

To investigate the nature of this function, the experimental data are divided by the data predicted by the homogeneous model according to Eq. (4.2). Figure 4.8 illustrates that this correction function depends mainly on the vapor quality and shows no clear dependence from the saturation pressure and the insert type. Moreover, no dependence from the mass flux could be observed (data points with different mass fluxes are each summarized with a single symbol in Figure 4.8, here no scattering can be detected). Consequently, the value of the correction function, Ω, and the corresponding uncertainty can be estimated from Figure 4.8 for all investigated porous inserts and the investigated parameter range. For a generally valid mathematical description, a larger database should be considered.

Figure 4.8: Experimental pressure drop data (mass fluxes ≥ 50 kg m^{-2} s^{-1} for sponges and ≥ 75 kg m^{-2} s^{-1} for hiTRAN® wire matrix elements) divided by Eq. (4.2) to obtain a correction function, Ω. This function is displayed as a function of the vapor quality for all insert types and saturation pressures investigated.

And fifth, a universal correction function describes the pressure drop, although the flow pattern varies from stratified to annular (compare Section 4.3). Consequently, the flow pattern has no influence on the adiabatic pressure drop of porous inserts in the tested parameter range, indicating that the predominant mechanisms remain unaffected by the flow pattern.

In summary, the hypothesis of this thesis can be accepted for the adiabatic pressure drop, although an even better description can be obtained by multiplying the homogeneous model by a fitting function. To avoid the need for a fitting function, it is recommended to apply the homogeneous approach to the Forchheimer equation. This leads to Eq. (4.2) for describing the adiabatic pressure drop in porous structures at high mass fluxes. The Forchheimer coefficient, β, should be determined experimentally by single-phase measurements. If this is not possible, β may be estimated by models suitable for single-phase flow.

4.1.3 Dependence on heat input

To investigate the influence of heat input, the results of the diabatic pressure drop are compared with the corresponding adiabatic pressure drop. The latter is calculated according to 2nd order polynomials on the basis of a vapor quality profile in the test section because small, unavoidable changes of operating conditions (especially mass flux and vapor quality) overlay the effect of the heat input. Figure 4.1 exemplarily shows such 2nd order polynomials.

Figure 4.9 shows the additional pressure drop due to heat input as a function of the heat flux, which is related to the distance between the pressure taps, $\dot{q}^*$. For comparison, the results of the empty tube under the same operating conditions are shown (open symbols), together with the prediction of the acceleration pressure drop by the homogeneous model for constant fluid properties (see Eq. (2.14) in Section 2.3.2).
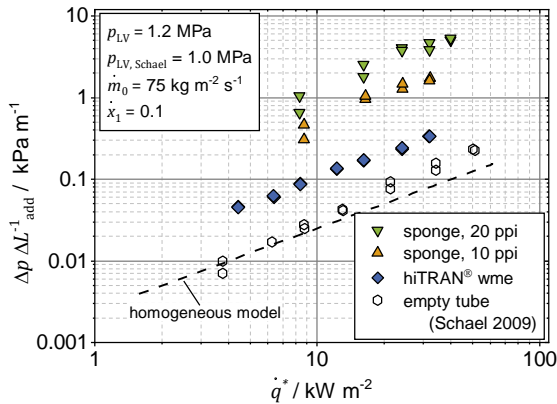
Figure 4.9: Additional pressure drop due to heating as a function of the heat flux related to the distance between the pressure taps. Empty tube data by Schael [24] was recorded at a saturation pressure of 1.0 MPa.

For the empty tube, the acceleration pressure drop calculated by the homogeneous model (Eq. (2.14)) describes the experimental data well. Contrary, the additional pressure drop in tube with inserts exceeds the acceleration pressure drop observed in the empty tube by orders of magnitude. In general, the higher the adiabatic pressure drop in a tube with insert (20 ppi sponge > 10 ppi sponge

> hiTRAN® wire matrix elements), the higher is the additional pressure drop due to heat input. The additional pressure drop in tubes with inserts is, similar to the acceleration pressure drop in the empty tube, proportional to the heat input. However, too less data and no physical concept is available to develop a statistically reliable model to describe the additional pressure drop due to heating.
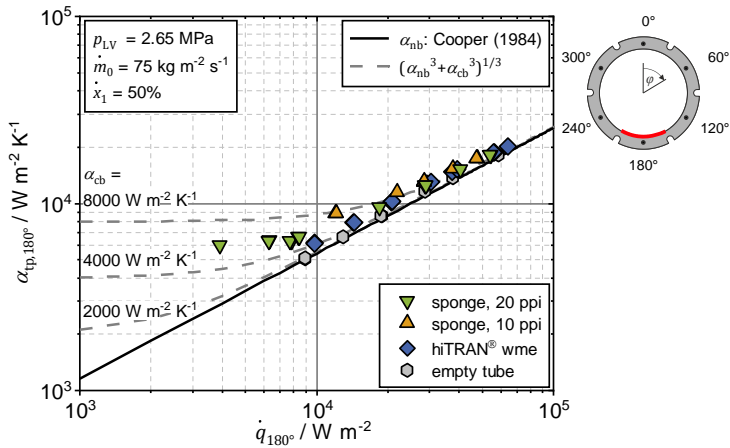
4.2   Heat transfer

In horizontal tubes, the heat transfer during flow boiling is directly related to the wetting behavior of the fluid flow. To assess the influence of the inserts which extends beyond a change in wetting, the heat transfer in completely wetted segments is analyzed first. The heat transfer in partially wetted segments is evaluated based on the results for completely wetted segments. The last section briefly discusses intermittently wetted segments.

4.2.1   Completely wetted segments

The bottom segment (thermocouple at 180°) and the adjacent segments (120°, 240°) are completely wetted for all conditions investigated, if no dryout occurs due to high vapor quality. The top segments (0°, 60°, 300°) are wetted for mass fluxes ≥ 75 kg m^{-2} s^{-1} (sponges) and ≥ 125 kg m^{-2} s^{-1} (hiTRAN® wire matrix elements) respectively.

Figure 4.10 and Figure 4.11 illustrate exemplarily for selected operating conditions the local heat transfer coefficient of the bottom segment in the first measurement plane for different inserts as well as - for comparison - for the empty tube. In addition, the nucleate boiling contribution, α_{nb}, according to Cooper [4], Eq. (2.17), and the superposition with a hypothetical convective boiling contribution, α_{cb}, of 2000 W m^{-2} K^{-1}, 4000 W m^{-2} K^{-1}, and 8000 W m^{-2} K^{-1} are shown for orientation. The data points shown are representative of all operating conditions studied.

Figure 4.10: Comparison of the local heat transfer coefficient of the bottom segment (180°) in tubes with inserts with the heat transfer coefficient in an empty tube at a saturation pressure of 2.65 MPa. The nucleate boiling contribution according to Cooper [4] and its superposition with a hypothetical convective contribution serve as orientation.
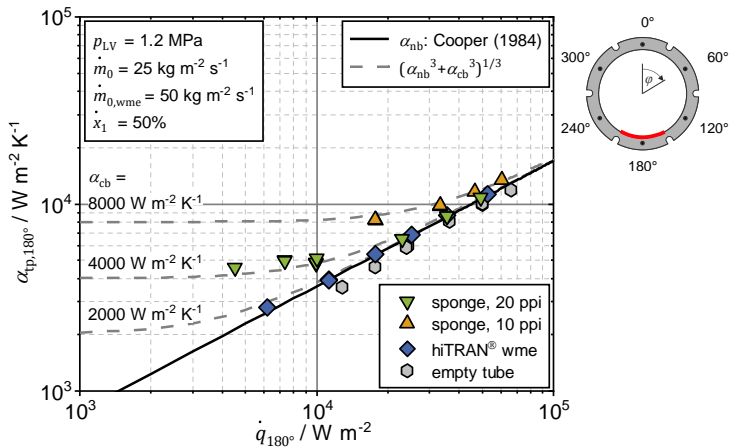
Figure 4.11: Comparison of the local heat transfer coefficient of the bottom segment (180°) in tubes with inserts with the heat transfer coefficient in an empty tube at a saturation pressure of 1.2 MPa. The nucleate boiling contribution according to Cooper [4] and its superposition with a hypothetical convective contribution serve as orientation.

For high heat fluxes, the local heat transfer coefficients of all structures in the fully wetted bottom segment (180°) asymptotically approach Cooper's prediction [4] of the nucleate boiling contribution, independent of the other operating conditions. In contrast, inserts, especially sponges, increase the local heat transfer coefficient at low heat fluxes compared to the empty tube. This can be explained by an enhanced convective heat transfer. Similar observations are made for all completely wetted segments. Consequently, the investigated inserts barely affect the nucleate boiling, but increase the convective heat transfer.

To investigate the convective heat transfer contribution in more detail, the nucleate boiling contribution is subtracted from the experimental results according to Eq. (4.4) for completely wetted segments. Such an approach was used by Kattan et al. [1] for determining the convective boiling contribution in empty tubes.

$$\alpha_{cb} = \sqrt[3]{\alpha_{exp}^3 - \alpha_{nb,Cooper}^3} \qquad (4.4)$$

In Figure 4.12 and Figure 4.13, the resulting Nusselt number, $Nu_{cb} = \alpha_{cb} \cdot L \cdot \lambda_L^{-1}$, are plotted as a function of the Reynolds number calculated using the separated approach, Eq. (2.21) for the bottom segments. The void fraction is computed by the Rouhani drift-flux model [40]. To exclude the possibility that a slightly incorrect calculation of the nucleate boiling contribution has a strong effect on the evaluation, only data points where the convective contribution according to Eq. (4.4) exceeds the nucleate boiling contribution are considered. The single-phase heat transfer correlations by Bianchi et al. [5], Eq. (2.25), for sponges and the correlation by CALGAVIN [33] for HiTRAN® wire matrix elements are displayed in Figure 4.12 and Figure 4.13 for comparison. The validity of the correlation of Bianchi et al. [5] for wall heat transfer of single-phase flow through the sponge structures could be ascertained by means of single-phase measurements of the heat transfer coefficient in the test section with 20 ppi sponge inserts (see Appendix C).
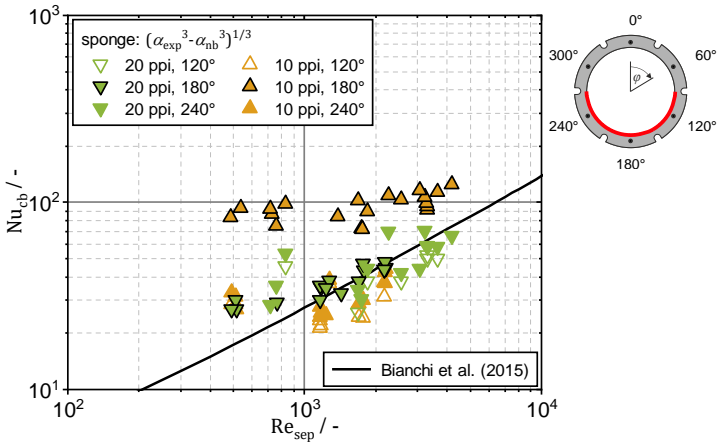
Figure 4.12: Comparison of the convective boiling contribution of wetted segments in the lower half of the tube in terms of Nusselt number, Nu_{cb}, as a function of the separated Reynolds number, Re_{sep}, for sponge inserts. The single-phase convection correlation by Bianchi et al. [5] is shown for comparison.
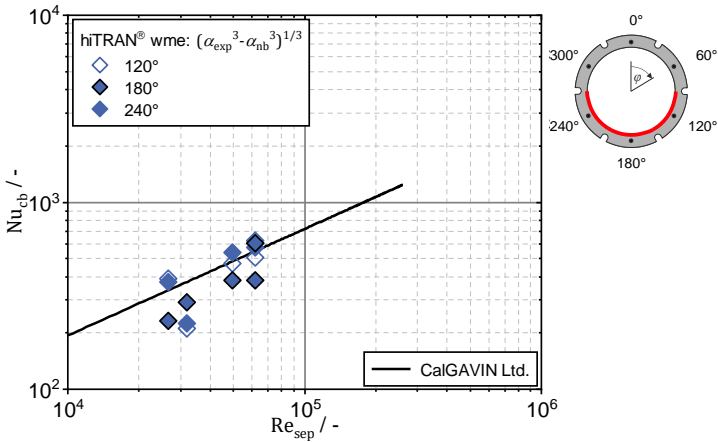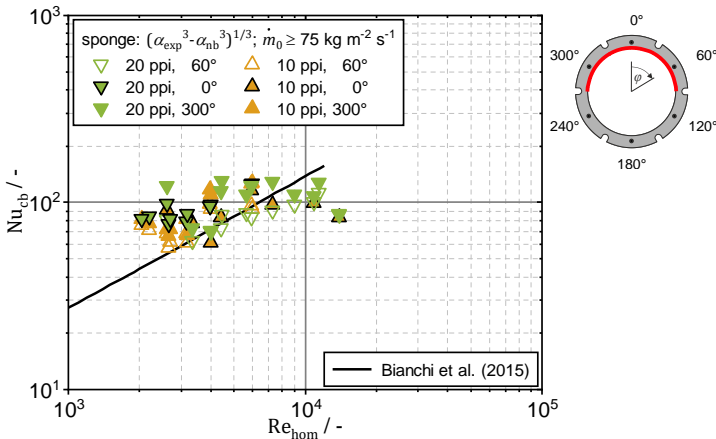

Figure 4.13: Comparison of the convective boiling contribution of wetted segments in the lower half of the tube in terms of Nusselt number, Nu_{cb}, as a function of the separated Reynolds number, Re_{sep}, for hiTRAN® wire matrix elements. The single-phase convection correlation by CALGAVIN Ltd. [33] is shown for comparison.

It follows that – except for the 10 ppi sponge in the bottom segment (180°) – the single-phase heat transfer correlations evaluated with the separated

Reynolds number are a good estimate for the order of magnitude and the dependence of the operating conditions. The scattering is by far less than observed for empty tubes (compare Figure 2.11 in Section 2.5.1). It can be seen that the convective boiling contribution depends slightly on the azimuthal location (see also the previous work, Weise et al. [127]). This effect is most pronounced for the 10 ppi sponge, where the heat transfer in the bottom segment significantly exceeds the heat transfer in the adjacent segments. High-speed recordings of the flow indicate variations in the frequency and size of larger bubbles passing near the respective segments. Presumably, mainly larger bubbles dispersed in the liquid phase flowing near the wall increase the convective heat transfer [127]. Lu and Zhao [3] reach a similar conclusion. They attribute the increased heat transfer to the breakup of large bubbles.

The same evaluation is performed for the top segments if completely wetted. In contrast to the bottom segments, the Nusselt number is plotted as a function of the homogeneous Reynolds number according to Eq. (2.20) in Figure 4.14 and Figure 4.15.

Figure 4.14: Comparison of the convective boiling contribution of wetted segments in the upper half of the tube in terms of Nusselt number, Nu_{cb}, as a function of the separated Reynolds number, Re_{sep}, for sponge inserts. The single-phase convection correlation by Bianchi et al. [5] is shown for comparison.
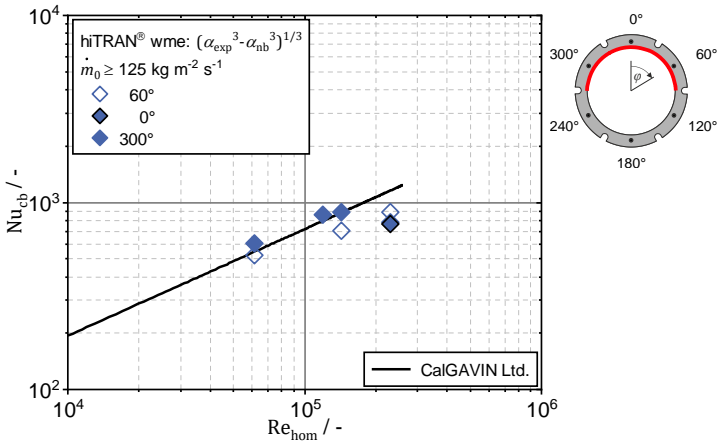
Figure 4.15: Comparison of the convective boiling contribution of wetted segments in the upper half of the tube in terms of Nusselt number, Nu_{cb}, as a function of the separated Reynolds number, Re_{sep}, for hiTRAN® wire matrix elements. The single-phase convection correlation by CALGAVIN Ltd. [33] is shown for comparison.

The results of this analysis regarding the order of magnitude, the scattering and the dependence on the operating conditions are similar to the results for the lower half of the tube. However, a homogeneous approach describes the heat transfer coefficient in the upper half of the tube better than a separated approach. This may be due to the distribution of vapor bubbles in the liquid flowing through the porous structures: The lower half of the tube is mostly wetted by liquid in which at most small bubbles are dispersed. In the upper half of the tube, the bubbles coalesce and form larger plugs. The average velocity in the lower half of the tube is therefore probably lower than in the upper half. This is represented by the separated model, while due to the good mixing with large bubbles the velocity in the upper part of the tube is high. This also reduces the slip between liquid and the vapor phase, which could explain the good accordance with the homogeneous model.

In summary, the inserts investigated have no significant influence on the contribution of nucleate boiling to the flow boiling heat transfer in fully wetted segments. Therefore, the same correlation as in the empty tube can be used for describing the nucleate boiling contribution, in this case Cooper's model (see Eq. (2.17)). However, the convective heat transfer is significantly increased

compared to the empty tube. Vapor quality, mass flux, and local flow pattern, i.e., the frequency and size of dispersed bubbles, can affect this convective contribution. In most cases, the convective contribution can be well described using appropriate single-phase correlations and a Reynolds number calculated according to the separated approach for the lower half of the tube and the homogeneous approach for the upper half of the tube can describe the convective contribution well. A suitable model for the convective heat transfer contribution in tubes with sponge inserts is the single-phase equation by Bianchi et al. [5], Eq. (2.25). For hiTRAN® wire matrix elements, the use of the CALGAVIN Ltd. confidential correlation is recommended. Consequently, established laws without fitting factors can well describe both magnitude and trend of the flow boiling heat transfer coefficient of completely wetted segments.

4.2.2   Partially wetted segments

To investigate the influence of wetting on the local heat transfer coefficient, heat transfer coefficients at the top segment (0°) and adjacent segments (60°, 300°) are compared at different operating conditions. Due to symmetry, only results for the 300° segment are presented in the following. First, the heat transfer coefficient of the 20 ppi sponge is characterized in more detail. Later, the characteristics of the 10 ppi sponge and the hiTRAN® wire matrix elements are studied comparatively.

In Figure 4.16 the local heat transfer coefficient of the top segment is shown at a vapor quality of approximately 15%, a saturation pressure of 2.65 MPa, and mass fluxes varying from 25 kg m^{-2} s^{-1} to 125 kg m^{-2} s^{-1}. The heat transfer coefficients at a mass flux of 100 kg m^{-2} s^{-1} and 125 kg m^{-2} s^{-1} differ only slightly at low heat fluxes and converge for high heat fluxes, indicating completely wetted segments (compare Section 4.2.1). The heat transfer coefficient at 75 kg m^{-2} s^{-1} also almost coincides with the heat transfer coefficients at higher mass fluxes. For lower mass fluxes, the heat transfer coefficients are shifted towards lower values, indicating a significant dewetting of the top segment. For a vapor quality of approximately 55% (Figure 4.17), this effect is more pronounced.
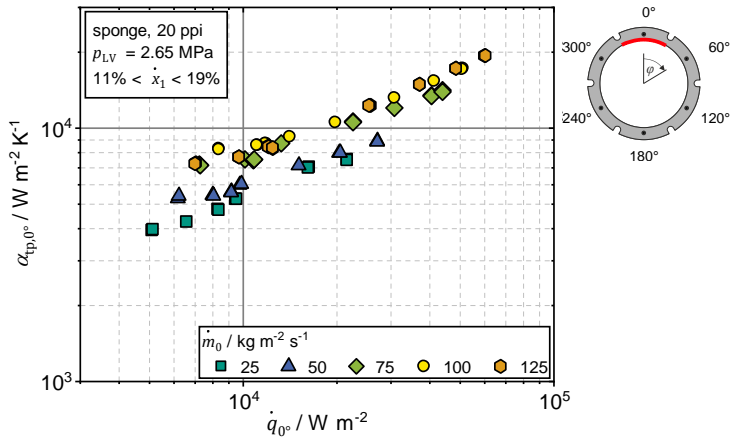
Figure 4.16: Comparison of the local heat transfer coefficient at the tube crest (top segment, 0°) for the 20 ppi sponge for different mass fluxes at saturation pressure of 2.65 MPa and a vapor quality of approximately 15%.
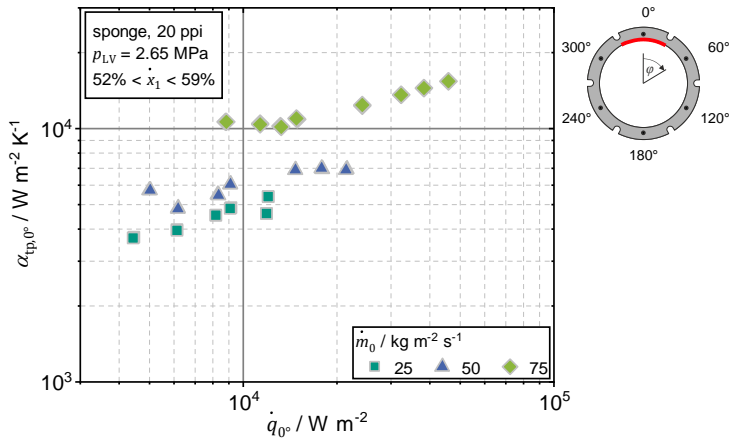
Figure 4.17: Comparison of the local heat transfer coefficient at the tube crest (top segment, 0°) for the 20 ppi sponge for different mass fluxes at saturation pressure of 2.65 MPa and a vapor quality of approximately 55%.

For a more detailed investigation, the heat transfer coefficients of the top segment and the adjacent segment (300°), $\alpha_{tp,0°}$ and $\alpha_{tp,300°}$, are compared to

Eq. (4.5). Section 2.5 explains the theoretical background of Eq. (4.5). The vapor heat transfer coefficient, α_v, for describing the heat transfer of the unwetted arc and the convective boiling contribution of the wetted arc, α_{cb}, are calculated according to the single-phase model by Bianchi et al. [5] (see Eq. (2.25)) using the homogeneous approach to adapt it to two-phase flow (see Section 4.2.2). The nucleate boiling heat transfer contribution of the wetted arc, α_{nb}, is calculated according to Cooper's model (see Eq. (2.17)). The only parameter fitted in the following is the dry fraction, $f_{dry,j}$.

$$\alpha_{tp,j} = f_{dry,j} \cdot \alpha_v + \left(1 - f_{dry,j}\right) \cdot \sqrt[3]{\alpha_{nb,j}^3 + \alpha_{cb}^3} \qquad \textbf{(4.5)}$$

Figure 4.18 and Figure 4.19 illustrate this comparison for a 20 ppi sponge insert at 26.5 MPa and a mass flux of 75 kg m^{-2} s^{-1}. In this case, Eq. (4.5) with $f_{dry} = 0$ approximates the measurement results for all vapor qualities and both the top segment (Figure 4.18) as well as the adjacent segments (Figure 4.19) reasonably. However, a slight deviation might be observed at high heat fluxes (compare also Figure 4.16).

Therefore, the time characteristic of the wall temperatures of all six segments, T_j, is analyzed in more detail. Figure 4.20 and Figure 4.21 exemplify the time characteristic for a vapor quality of 13%, similar findings are obtained at higher vapor qualities and higher mass fluxes. For $\dot{q}_{ave} = 10$ kW m^{-2} (Figure 4.20), the variations of the wall temperature of all segments are in the same order of magnitude whereas for $\dot{q}_{ave} = 50$ kW m^{-2} (Figure 4.21), the variation in the top segment exceeds the variations in the others. A dry fraction $f_{dry} < 5\%$ would be below the sensitivity limit of the comparison with Eq. (4.5), hence negligible dewetting can be assumed at $p_{LV} = 2.65$ MPa and $\dot{m} = 75$ kg m^{-2} s^{-1} and high heat fluxes. Although the heat flux affects the wetting behavior, this is neglected for the following analysis, since deviations of the dry fraction of $\pm 5\%$ are within the limits of measurement accuracy.
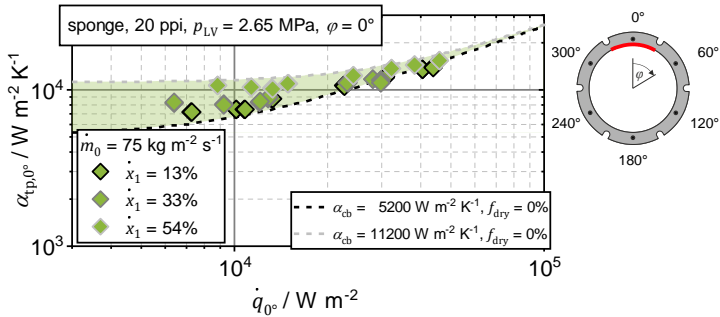
Figure 4.18: Local heat transfer coefficient in the top segment (0°) as a function of local heat flux for 20 ppi sponge inserts at 2.65 MPa. Heat transfer coefficients predicted by Eq. (4.5) are displayed.
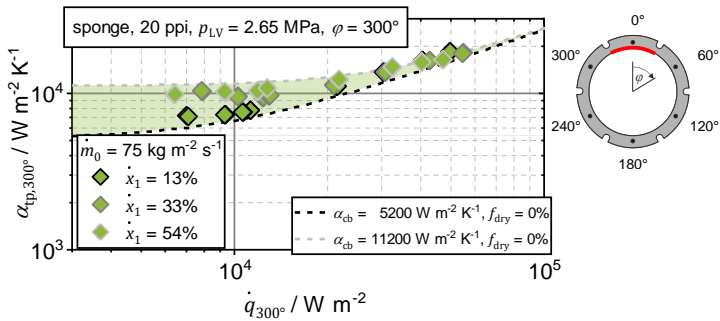

Figure 4.19: Local heat transfer coefficient in the adjacent segment (300°) as a function of local heat flux for 20 ppi sponge inserts at 2.65 MPa. Heat transfer coefficients predicted by Eq. (4.5) are displayed.
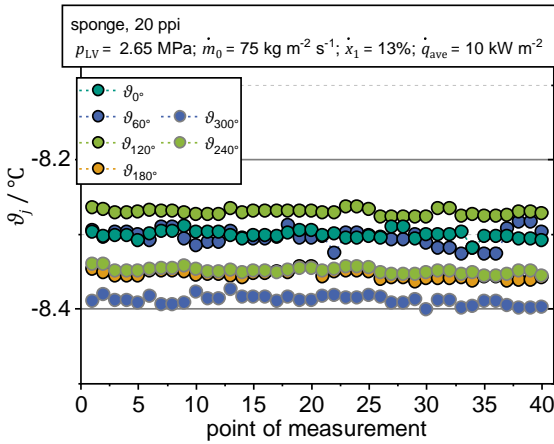
Figure 4.20: Temperature measured in the individual segments during heat transfer measurements at a heat flux of 10 kW m^{-2}. The mass flux (75 kg m^{-2} s^{-1}), the saturation pressure (2.65 MPa), and the vapor quality (13%) are kept constant. 40 points of measurement are recorded within 50 s.
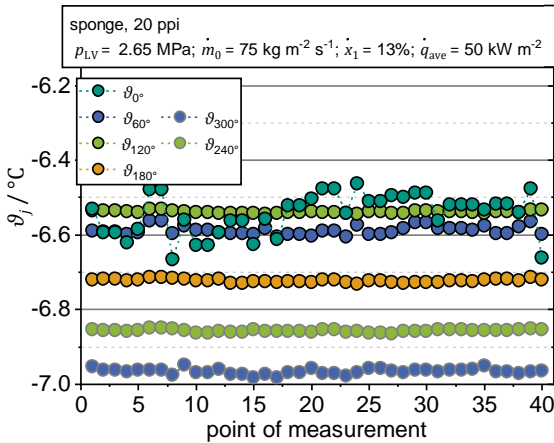
Figure 4.21: Temperature measured in the individual segments during heat transfer measurements at a heat flux of 50 kW m^{-2}. The mass flux (75 kg m^{-2} s^{-1}), the saturation pressure (2.65 MPa), and the vapor quality (13%) are kept constant and are the same as in Figure 4.20. 40 points of measurement are recorded within 50 s.

Contrary, as shown in Figure 4.22 for lower mass fluxes ($\dot{m}_0 = 25$ kg m^{-2} s^{-1}; 50 kg m^{-2} s^{-1}) and vapor qualities between 14% and 20%, using dry fractions of approximately 10% to 15% in Eq. (4.5), this equation describes well the experimental data in the top segment. The adjacent segments seem to be completely wetted. For vapor qualities between 54% and 60%, dry fractions of approximately 40% in the top segment and 15% in the adjacent segments fit well. Consequently, in case of dewetting, the vapor quality seems to influence the dry fraction more than the mass flux. However, the heat transfer coefficients are lower for lower mass fluxes. This seems to be mainly due to the lower convective boiling contribution.

Figure 4.22: Local heat transfer coefficient in the top segment (0°) as a function of local heat flux for 20 ppi sponge inserts at 2.65 MPa. Heat transfer coefficients predicted by Eq. (4.5) are displayed.
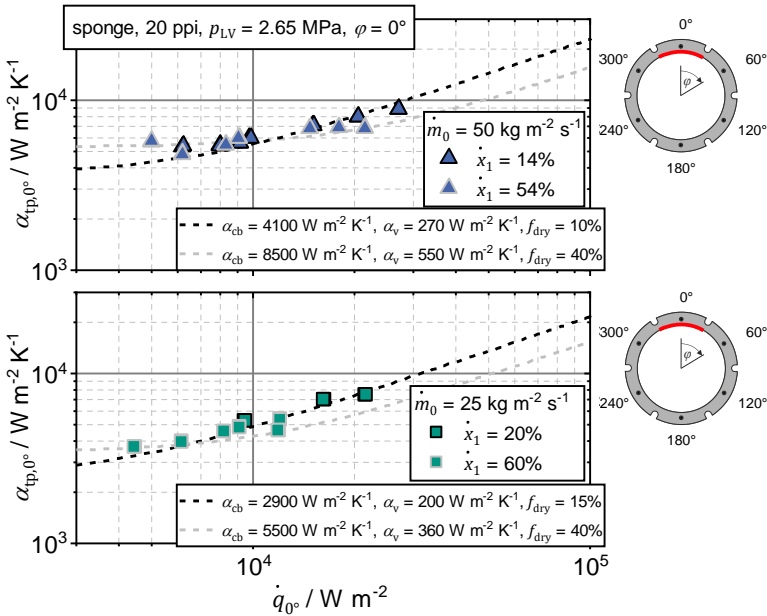
The fact that the wetting behavior nevertheless depends on the mass flux is shown in Figure 4.23 and Figure 4.24. Here, the time characteristics of the temperatures measured in the segments are plotted for $p_{LV} = 2.65$ MPa,

$\dot{m}_0 = 25$ kg m^{-2} s^{-1} and $\dot{m}_0 = 50$ kg m^{-2} s^{-1}, $\dot{x}_1 = 60\%$ resp. $\dot{x}_1 = 54\%$ and $\dot{q}_{ave} = 10$ kW m^{-2}. For both $\dot{m}_0 = 25$ kg m^{-2} s^{-1} and $\dot{m}_0 = 50$ kg m^{-2} s^{-1}, an increased variation of the temperature can be observed for the top three segments compared to the bottom segments. The amplitude and frequency of the variation depend on the mass flux, but not on the dry fraction in the respective segment. Thus, at $\dot{m}_0 = 25$ kg m^{-2} s^{-1} (Figure 4.23), both amplitude and frequency of the wall temperature at 300°, 0°, and 60° are smaller than at $\dot{m}_0 = 50$ kg m^{-2} s^{-1} (Figure 4.24).
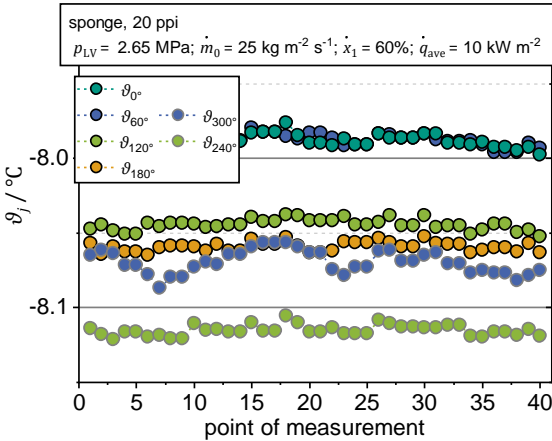
Figure 4.23: Temperature measured in the individual segments during heat transfer measurements at a mass flux of 25 kg m^{-2} s^{-1}. The saturation pressure (2.65 MPa), the vapor quality (60%), and the heat flux (10 kW m^{-2}) are kept constant. 40 points of measurement are recorded within 50 s.
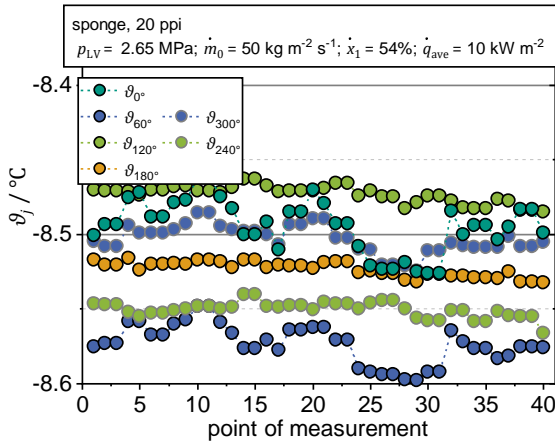
Figure 4.24: Temperature measured in the individual segments during heat transfer measurements at a mass flux of 50 kg m^{-2} s^{-1}. The saturation pressure (2.65 MPa), the vapor quality (54%), and the heat flux (10 kW m^{-2}) are kept constant and are the same as in Figure 4.23. 40 points of measurement are recorded within 50 s.

To assess the influence of the saturation pressure, the heat transfer coefficients measured at 1.2 MPa and 1.9 MPa are compared with Eq. (4.5) in Figure 4.25. The comparison reveals that the lower the saturation pressure (with otherwise constant mass flux and vapor quality), the lower the wetted area. Significant dewetting of the 300° segment (see Figure 4.26) occurs especially at low saturation pressures and mass fluxes and at the same time medium to high vapor qualities.
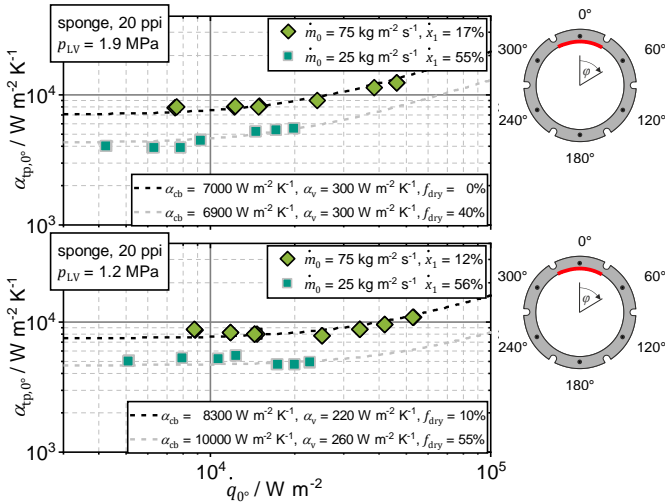
Figure 4.25: Local heat transfer coefficient in the top segment (0°) as a function of local heat flux for 20 ppi sponge inserts at 1.2 MPa and 1.9 MPa. Heat transfer coefficients predicted by Eq. (4.5) are displayed.
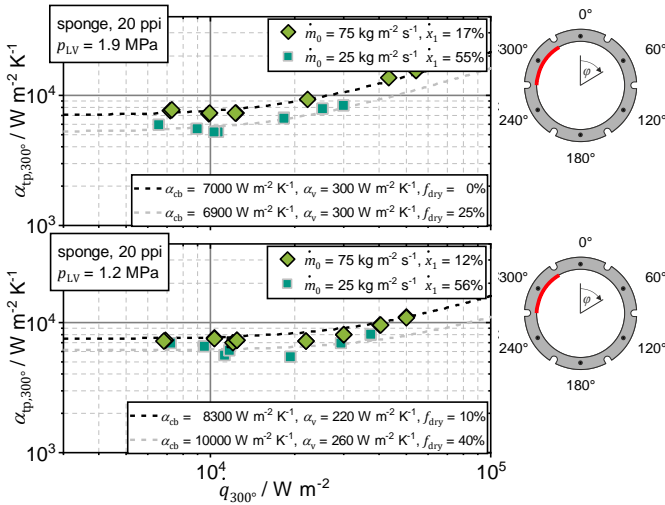
Figure 4.26: Local heat transfer coefficient in the adjacent segment (300°) as a function of local heat flux for 20 ppi sponge inserts at 1.2 MPa and 1.9 MPa. Heat transfer coefficients predicted by Eq. (4.5) are displayed.

In summary, Eq. (4.5) describes well the observed heat transfer coefficients during flow boiling in tubes with 20 ppi sponge inserts if the dry fraction is chosen appropriately. The dry fractions used in Eq. (4.5) are in line with the observations regarding the time characteristics of the wall temperature. Using Eq. (4.5), on can conclude that the dry fraction of partially wetted segments depends on vapor quality and saturation pressure rather than mass flux. This can be also illustrated by plotting the dry fraction of these segments as a function of the homogeneous den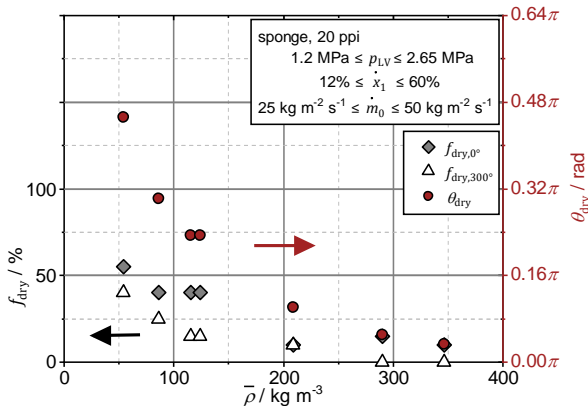sity according to Eq. (2.5) in Figure 4.27. The homogeneous density scales with vapor quality and saturation pressure (compare Eq. (2.5)). The higher the homogeneous density, the lower the dry fraction, i.e., the better the wetting of the respective segment. The dry angle is the sum of the dry fractions, $f_{\mathrm{dry},j}$, of all n segments multiplied by the arc of a segment, $2\pi \ \mathrm{rad}/n$: $\theta_{\mathrm{dry}} = \frac{2\pi \ \mathrm{rad}}{n} \cdot \sum_{j=1}^{n} f_{\mathrm{dry},j}$. The dependence of the dry angle on the homogeneous density follows a steadily declining trend. Describing these data points with a common, physically meaningful function has not been successful. However, this diagram shows that for a tube with a 20 ppi sponge, the dry angle in the case of partial wetting does not depend on the mass flux but on the homogeneous density. This contradicts the approach proposed by Lu and Zhao [3] and Zhu et al. [14] to interpolate the dry angle based on the mass flux.

Figure 4.27: Dry fractions of the top segment (0°) and the adjacent segment (300°) as well as dry angle plotted as a function of the homogeneous density according to Eq. (2.5).

For the 10 ppi sponges, measurement series obtained at $p_{LV} = 2.65$ MPa, $\dot{x}_1 = 22\%$, and 25 kg m^{-2} s^{-1} $< \dot{m}_0 < 125$ kg m^{-2} s^{-1} are compared analogously with Eq. (4.5) to verify the suitability of this equation for describing the data and to investigate the influences of the operating conditions on the dry fraction (see Figure 4.28). While the measurement series at $\dot{m}_0 = 125$ kg m^{-2} s^{-1} and $\dot{m}_0 = 100$ kg m^{-2} s^{-1} can be predicted well by Eq. (4.5) assuming complete wetting, Eq. (4.5) cannot describe the dependence on heat flux well for lower mass fluxes. This can be caused by two effects: decreasing wetting with increasing heat flux and increased convective boiling contribution in case of partial wetting. The fact that the first effect does not occur as strongly with 20 ppi sponges could be explained by the larger pore size of the 10 ppi sponges, which favors coalescence of vapor bubbles. The latter effect can be explained by a reduced film thickness compared to complete wetting. Figure 4.29 thus compares the heat transfer coefficient in case of partial wetting with Eq. (4.5) using a convective boiling contribution increased by 50%. Such an increase is within the tolerance found for completely wetted segments in the upper half of the tube (compare Figure 4.14). This assumption results in increased dry fractions, f_{dry}. Regardless of the convective boiling contribution used (α_{cb} or $1.5 \cdot \alpha_{cb}$), the dry fraction in the top segment is increased compared to the 20 ppi sponges, i.e., the wetting is worse. Figure 4.28 and Figure 4.29 show measurement series at constant saturation pressure and vapor qualities, hence constant homogeneous density. Since a dependence of the dry fraction on the mass flux can be recognized, the statement made for 20 ppi of the sole dependence of this parameter on the homogeneous density cannot be confirmed for the 10 ppi sponges.

Figure 4.28: Local heat transfer coefficient in the top segment (0°) as a function of local heat flux for 10 ppi sponges at 2.65 MPa. Heat transfer coefficients predicted by Eq. (4.5) are displayed.

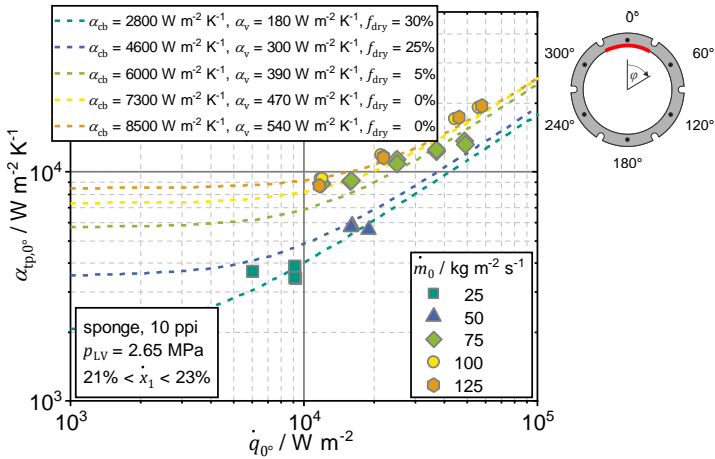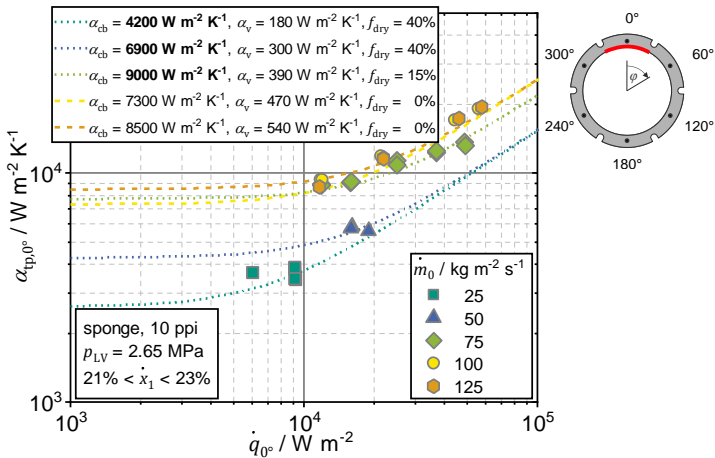**Figure 4.29:** Sensitivity analysis for low mass fluxes of the local heat transfer coefficient in the top segment (0°) as a function of local heat flux for 10 ppi sponges at 2.65 MPa. The convective boiling contribution as used in Eq. (4.5) is increased by 50% (printed in bold).

For hiTRAN® wire matrix elements, the top segment is not wetted at mass fluxes ≤ 125 kg m^{-2} s^{-1}. Figure 4.30 and Figure 4.31 therefore illustrate the comparison of the measured data with predictions according to Eq. (4.5) for the adjacent segment (300°). The convective boiling contribution and the vapor heat transfer coefficient are calculated according to the in-house correlation by CALGAVIN Ltd. [33] using the homogeneous model to calculate the two-phase Reynolds number. The homogeneous model is chosen because it demonstrated good agreement with the convective boiling contribution of the completely wetted top segments (compare Section 4.2.1). Figure 4.30 and Figure 4.31 reveal that for hiTRAN® wire matrix elements the dry fraction of the 300° segment depends on the vapor quality and the saturation pressure, but also, unlike the dry fraction for the 20 ppi sponge, depends slightly on the mass flux. Consequently, the statement that the dry angle depends on the homogeneous density for partially wetted tubes cannot be generalized for all porous insert types. The time characteristics of the wall temperature is comparable to time course observed for the sponges.
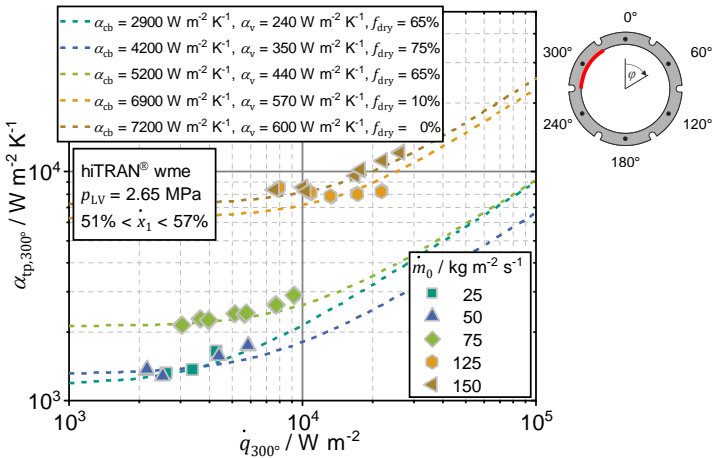
Figure 4.30: Local heat transfer coefficient in 300° adjacent segment as a function of local heat flux for hiTRAN® wire matrix elements at 2.65 MPa. Heat transfer coefficients predicted by Eq. (4.5) are displayed.
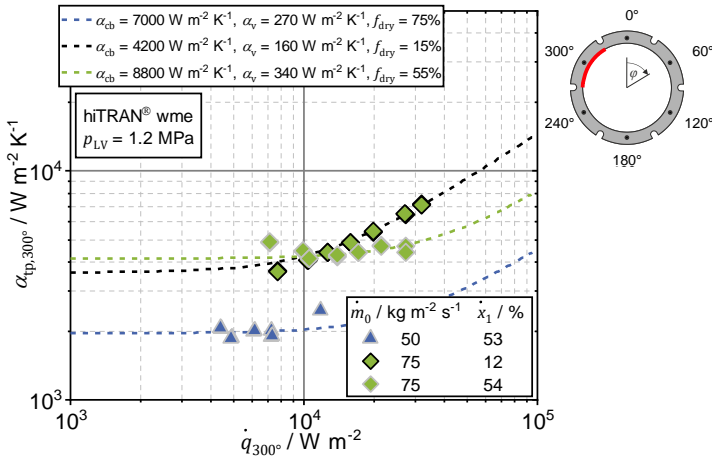
Figure 4.31: Local heat transfer coefficient in 300° adjacent segment as a function of local heat flux for hiTRAN® wire matrix elements at 1.2 MPa (right). Heat transfer coefficients predicted by Eq. (4.5) are displayed.
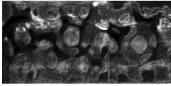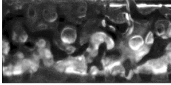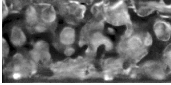
To summarize, the magnitude and the trend of the heat transfer coefficient of partially wetted segments can be described well by Eq. (4.5) calculating the vapor heat transfer coefficient and the convective boiling heat transfer coefficient by established single-phase correlations adapted to two-phase flow. Recommended single-phase correlations are the model by Bianchi et al. [5] (see Eq. (2.25)) for sponge inserts and the CALGAVIN Ltd. model [33] for hiTRAN® wire matrix elements. For all investigated inserts, using the homogeneous approach to calculate the Reynolds number leads to reasonable results for expressing the convective boiling heat transfer coefficient in the upper half of the tube. As in the case of the corresponding empty tube, the nucleate boiling heat transfer coefficient can be calculated according to Cooper's model (see Eq. (2.17)). The only fitting parameter in the presented analysis is the dry fraction. However, no physically meaningful function has been found to describe the dependency of the dry fraction and thus the dry angle on the operating parameters for all investigated inserts. The dry angle scales with the homogeneous density in case of 20 ppi sponge inserts and is independent on mass flux. This statement cannot be confirmed for 10 ppi sponges and hiTRAN® wire matrix elements.

4.3   Flow pattern

As elaborated in the preceding section, knowledge of the wetting behavior and thus the dry angle, θ_{dry}, is crucial for modeling the heat transfer coefficient in horizontal tubes. Especially in the case of wavy or intermittent flow, the correct determination of this measure is not straightforward. Either the evaluation of local heat transfer coefficients and temperature variations or high-speed video recordings can be used to determine the dry angle. The latter would be advantageous due to the lower experimental effort. Therefore, both approaches are compared in the following. The basic ideas of the following sections are published in a previous work [127].

High-speed video recordings of the flow in an adiabatic sight glass allow for assessing the movement of the phase boundary. This evaluation is supported by image processing of the high-speed video recordings (compare Section 3.4.7). The standard deviation of the pixels corresponds to the average variation intensity of the phase boundary. The flow patterns listed in Table 4.1 can be distinguished. The classification is based on the classification of flow patterns in empty tubes (compare Section 2.4.1). In contrast to the empty tube, the phase boundary of stratified flow is not parallel to the tube axis, since the liquid is attached to the insert surface due to capillarity. Instead, the immobility of the phase boundary is used as a criterion. Distracted stratified flow is a peculiarity of tubes with inserts and is most comparable to wavy flow in empty tubes. If the phase boundary occupies the entire tube cross section, annular flow is assumed. Both distracted stratified flow and annular flow are, strictly speaking, intermittent flows because the porous structures disperse and redirect the vapor bubbles. However, under some operating conditions, slug like behavior has been observed, where the flow characteristics changes at a lower frequency than the passing of individual bubbles. Such flow is described as intermittent. Mist flow and dryout were not observed under the investigated operating conditions.

Table 4.1:   Classification of flow pattern in horizontal tubes with porous inserts assessed by an-
alyzing high-speed video recordings, adapted from a previous work [127]. Symbols
are used in Figure 4.32.

flow pattern, symbol, ab-breviation	standard deviation of video frames	characteristics of phase boundary
stratified flow 🔴 (s)		distinct phase boundary, pinning of contact line, stratification
distracted stratified flow 🟢 (s*)		stratified zone with distracted phase boundary, phase boundary pinned to struts in upper part of tube
annular flow 🔵 (a)		distracted phase boundary also at tube apex
intermittent flow 🟡 (i)	not applicable	temporal variation of phase distribution with secondary frequency

The analysis of the local heat transfer coefficient and the wall temperature var-
iation, as discussed in Section 4.2.2, leads to a slightly different phenomeno-
logical classification of the flow through inserts. The analysis of the heat trans-
fer coefficient allows a distinction between completely wetted perimeter and
partially wetted perimeter. Complete wetting is assumed if, for a measurement
series (constant mass flux, saturation temperature, and vapor quality but vary-
ing heat flux), the heat transfer coefficients in the nucleate boiling regime (high
heat fluxes) coincide for all segments. If no heat transfer data in the nucleate
boiling regime are available for a measurement series, a comparison with
Eq. (4.5) is used to decide. In partially wetted segments, the heat transfer co-
efficients in the nucleate boiling regime are reduced compared to completely
wetted segments.

Investigating the wall temperature, an increased temporal variation is observed
for partially wetted segments under heated condition. If all segments are com-
pletely wetted, the variation of the wall temperature of all segments is similar.
Since wall temperature variations are more sensitive to the wetting behavior
than the heat transfer coefficient (see Figure 4.18 to Figure 4.21 in Section
4.2.2), the classification is carried out separately according to these two crite-
ria. No stationary partially wetted segments (e.g., in stratified flow in empty

tubes) are observed under the operating conditions investigated. However, such behavior is conceivable at very low mass fluxes and is characterized by decreased heat transfer coefficients of the top segments and similar temporal variations of the wall temperature in all segments. Thus, stationary partially wetted segments would also be describable with the proposed criteria. Table 4.2 summarizes the observations.

Table 4.2: Classification of flow pattern in horizontal tubes with porous inserts assessed by analyzing local heat transfer coefficients. Symbols are used in Figure 4.32.

flow pattern, symbol, abbreviation	observation	wetting behavior
partially wetted ◇ (pw)	significant reduction of heat transfer coefficient (corresponds approximately to $\theta_{dry} > 3°$) in nucleate boiling region or based on prediction according to Eq. (4.5)	part of the perimeter partially wetted
completely wetted ▷ (cw)	nucleate boiling regime: same htc over the perimeter	entire perimeter wetted
instationary ⊡ (in)	temporal variation of the wall temperature of individual segments increased, at least at high heat fluxes	part of the perimeter intermittently wetted (temporal variations)
stationary ◻ (st)	temporal variation of the wall temperature similar for all segments	entire perimeter wetted or stationary non-wetted part

Figure 4.32 shows the flow pattern maps for saturation pressures of 1.2 MPa and 2.65 MPa for sponge inserts determined according to Table 4.1 and Table 4.2. First, the results from video recordings, heat transfer characterization and wall temperature variations are considered separately to compare the methods afterwards.
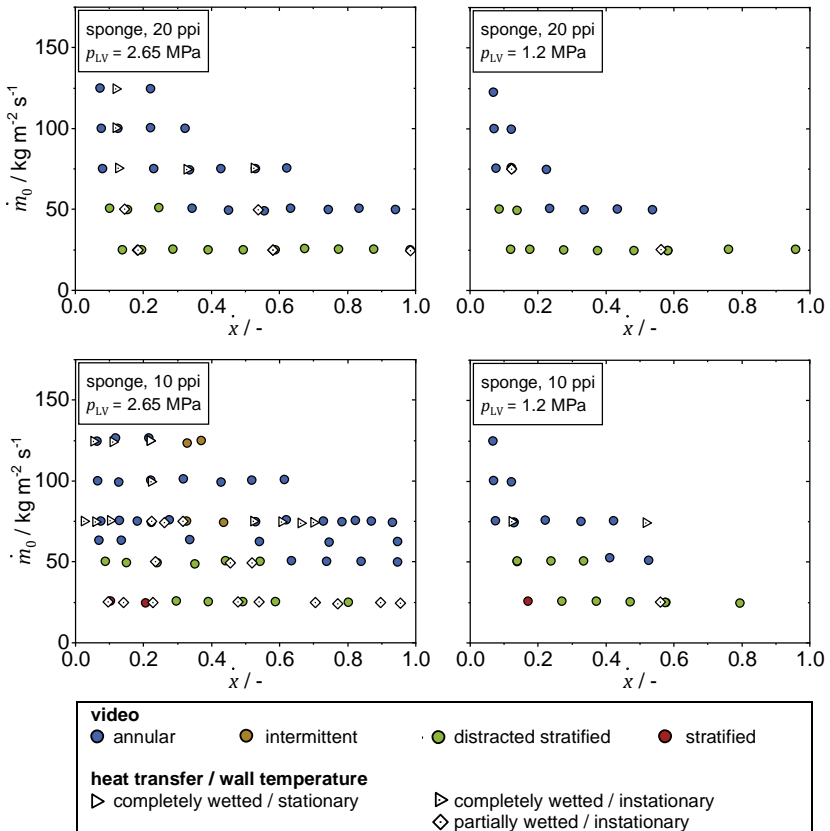
Figure 4.32: Flow pattern maps of CO_2 in a tube with a 10 ppi sponge insert (upper half) and a 20 ppi sponge (lower half) at a saturation pressure of 2.65 MPa and 1.2 MPa. Flow pattern are derived either from high-speed video recording (see Table 4.1) or from local heat transfer measurements/wall temperature variations (see Table 4.2).

By high-speed video recording, all flow patterns presented in Table 4.1 are observed for CO_2 flowing through 10 ppi and 20 ppi sponges under the operating conditions investigated. However, stratified flow is only witnessed for the 10 ppi sponge, and then only at low mass fluxes and vapor qualities. As the mass flux and the vapor quality increase, the phase boundary fluctuates more and more until, at even higher mass fluxes, the phase boundary fluctuations occupy the entire tube cross section. Intermittent flow is observed only at a few

operating conditions (for example for the 10 ppi sponge at high mass fluxes). The transitions between these flow patterns are at lower mass fluxes and vapor qualities for 20 ppi sponge compared to the 10 ppi sponge. This may be due to the smaller pore size of the 20 ppi sponges, which results in better mixing of the vapor and liquid phases. Similarly, transitions at a lower saturation pressure occur at lower mass fluxes and vapor qualities. This can be explained by a decreased vapor density, increasing the vapor velocity and thus the enhancing the mixing of the two phases.

A somewhat different result is obtained from the characterization of the heat transfer coefficient. Although wetting also increases with increasing mass flux, an increase in vapor quality does not necessarily lead to an improvement in wetting (see Figure 4.32, lower left, 10 ppi sponge at $p = 2.65$ MPa, $\dot{m}_0 = 75$ kg m^{-2} s^{-1}). Moreover, a heat transfer coefficient similar to that for complete wetting is achieved for both insert types at similar operating conditions.

A look at the characterization of the wall temperature variations reveals that only in one operating condition no increased variation of the temperature measured in the top segment can be detected (10 ppi sponge at $p = 2.65$ MPa, $\dot{m}_0 = 125$ kg m^{-2} s^{-1}, $\dot{x}_1 = 20\%$). At all other operating conditions, at least at high heat flux, this temperature varies more than in the other segments. Presumably, however, temperature variations at a higher heat flux than investigated are to be expected even for the exception mentioned.

Comparing the different approaches to classify the wetting behavior in Figure 4.32 leads to following results:
First, flows classified as stratified or distracted stratified based on the video recordings share the heat transfer characteristics of instationary partially wetted flow. Consequently, a part of the tube apex is already wetted when the phase boundary is stagnant or distracted and does not yet visibly occupy the entire tube cross section.
Second, some operating conditions classified as stratified/distracted stratified flow or annular flow exhibit the very same heat transfer and wall temperature

characteristic. Partial wetting is detected for annular flow in case of, for example, the 10 ppi sponge at $p = 2.65$ MPa, $\dot{m} = 75$ kg m^{-2} s^{-1}, and $20\% < \dot{x}_1 < 40\%$ (see Figure 4.32, top left) or for the 20 ppi sponge at $p = 2.65$ MPa, $\dot{m}_0 = 50$ kg m^{-2} s^{-1}, and $\dot{x}_1 = 55\%$ (see Figure 4.32, bottom left). Consequently, a distinction between partially wetted and completely wetted is not possible based on the distinction between distracted stratified and annular flow by video. This is attributed to the difficulty of observing a transparent liquid and vapor phase in a tube where the view is obstructed by inserts.

Third, intermittent flow (i.e., lower frequency slugs) has no effect on the heat transfer coefficient or the wall temperature variations. This is demonstrated by the observations for a 10 ppi sponge at $p_{LV} = 2.65$ MPa, $\dot{m}_0 = 75$ kg m^{-2} s^{-1}, and $20\% < \dot{x}_1 < 40\%$ (see Figure 4.32, top left).

Fourth, as already stated in Section 4.2.2, analysis of the wall temperature profile allows one to infer dewetting already at higher mass fluxes than an analysis of the heat transfer coefficient would suggest. Thus, even operating conditions that are characterized as completely wetted by the heat transfer coefficients still exhibit temperature variations. Conversely, this means that using the temperature variations to predict the heat transfer coefficient can lead to an underestimation of this measure.

Comparing the findings with the literature, Zhao and Lu [44] and Zhu et al. [89] locate the transition from intermittent to annular flow (corresponding to the transition from stratified annular to annular) at slightly higher mass fluxes (about 90 kg m^{-2} s^{-1} to 100 kg m^{-2} s^{-1} for their sponge inserts (5 ppi to 40 ppi), reduced pressure $p_r \in \{0.09; 0.15; 0.20\}$, and tube diameter, $D_i \in [7.9$ mm; 26 mm]) than observed by video recordings or heat transfer measurements in this work. The conditions studied by the aforementioned authors are comparable to the conditions investigated in this work (10 ppi/20 ppi, $p_r \in \{0.163; 0.360\}$, $D_i = 14$ mm). Only one flow pattern map is published by each group for all operating conditions. It was created from a combination of heat transfer and wall temperature characterization. Therefore, the results presented are equally susceptible to the shortcomings mentioned above. Therefore, it can be concluded that the flow patterns observed in this work do not contradict the literature.

In summary, neither the wall temperature variations nor the video recordings provide an accurate reference for deriving the heat transfer coefficient, especially the dry angle. Possibly, further experimental data could be used to find a generally applicable model to describe the transition curves for sponge inserts. This model could then be applied to predict the dry angle from the operating conditions. Since no physically meaningful correlation of the dry angle directly with the operating conditions could be found either (see Section 4.2.2), the estimation of the dry angle from experimental flow image data is still recommended as also proposed by Zhao and Lu [44]. However, this means that no established law for an *a priori* prediction could be found for the dry angle.

4.4 Averaged heat transfer coefficient

In the previous sections, the influence of wetting, convection and bubble formation on the local heat transfer coefficient was discussed in detail. Based on this, a model for predicting the circumferentially averaged heat transfer coefficient during flow boiling in horizontal tubes is presented and discussed below. The circumferentially averaged heat transfer coefficient is calculated according to Eq. (4.6) as the weighted sum of all local heat transfer coefficients in the individual segments of the test section, $\alpha_{\text{tp},j}$, in the present work $n = 6$.

$$\alpha_{\text{tp}} = \frac{1}{n} \sum_{j=1}^{n} \alpha_{\text{tp},j} \qquad\qquad \textbf{(4.6)}$$

Figure 4.33 summarizes the structure of the model for predicting the local heat transfer coefficient, $\alpha_{\text{tp},j}$.

Starting from the Rouhani drift-flux model [40] (Eq. (2.6)), which is used to determine the void fraction, the stratified dry angle, $\theta_{\text{dry,s}}$, and the Reynolds numbers, Re_{L}, for convective heat transfer in the wetted portion of the perimeter are determined. The Rouhani drift-flux model was developed for buoyancy-influenced flow through a vertical tube, but proved suitable for predicting the void fraction in a horizontal empty tube [1,42] as well as in a horizontal

tube filled with inserts [43,44]. As shown in Section 4.2.1, this is also true for the inserts and operating conditions studied in this thesis.

stratified dry angle

Biberg [100]

$\theta_{\text{dry,s}}$

void fraction

Rouhani drift-flux model [40]

A_V

$\varepsilon = \dfrac{A_V}{A_{L+V}}$

A_L

flow pattern and dry angle

- mechanistic model: to be determined,
  $f(L_{\text{insert}}, \varphi, \dot{x}, \dot{m}, p, \dot{q})$
- interim model:

$\dot{m}_0$

high-speed video recording
- annular
- distracted stratified

$\theta_{\text{dry}} = 0$

θ_{dry}: interpolation, Lu and Zhao [3]

0     $\dot{x}$ 1

Reynolds number for liquid phase

upper segments:

$Re_{\text{L,hom}} = \dfrac{\dot{m} \cdot L}{\bar{\rho} \cdot v_L}$

lower segments:

$Re_{\text{L,sep}} = \dfrac{\dot{m} \cdot (1 - \dot{x}) \cdot L}{\mu_L (1 - \varepsilon)}$

characteristic length, L, and mass flux according to single-phase heat transfer model

dry fraction of each segment

$f_{\text{dry},j} = \dfrac{\theta_{\text{dry},j}}{j}$

θ_j

$\theta_{\text{dry},j}$

Weise et al. [2]

convective boiling

single-phase heat transfer model

$Nu = f(Re_L, Pr_L)$

e.g. for sponges: Bianchi et al. [5]

$$\alpha_{\text{tp},j} = f_{\text{dry},j} \cdot \alpha_{V,j} + (1 - f_{\text{dry},j}) \cdot \sqrt[3]{\alpha_{\text{nb}}^3(\dot{q}_j) + \alpha_{\text{cb},j}^3}$$

vapor-phase heat transfer $Re_{V,\text{hom}} = \dfrac{\dot{m} \cdot L}{\bar{\rho} \cdot v_V}$

e.g. for sponges: Bianchi et al. [5]

pool boiling

Cooper [4]

Figure 4.33: Overview of the recommended structure of a mechanistic model for predicting the local heat transfer coefficient for non-uniformly heated evaporator tubes with porous inserts according to Section 4.2 to 4.3.

The calculation of the dry angle of stratified flow in an empty tube according to Biberg [100] and the determination of the dry angle, θ_{dry}, in the distracted stratified flow regime by linear interpolation as proposed by Lu and Zhao [3,90] is a good first approach to predict the wetting for the calculation of the average heat transfer coefficient. For this purpose, the flow pattern is determined by high-speed video recordings, as this is the only way to preserve the predictive nature of the model. If the heat transfer coefficient is to be determined with local resolution, a more detailed predictive model is required, which takes into account the influence of the inserts (e.g., via characteristic length and porosity), as well as the influence of the operating conditions $(p, \dot{m}, \dot{x}, \dot{q})$.

Both sponge inserts and hiTRAN® wire matrix elements increase the convective boiling contribution. The convective boiling contribution depends not only on the operating conditions, but also on the local wetting behavior. Therefore, the transfer of the heat transfer correlations developed for single-phase flow (Bianchi et al. [5] (Eq. (2.25)), CALGAVIN Ltd. [33]) is carried out separately in the upper and lower part of the tube. In the upper region, where a better mixing of the vapor and liquid phases can be assumed, the Reynolds number is taken based on the homogeneous model (Eq. (2.20)). In the lower range, where the liquid fraction is higher in relative terms, the Reynolds number is calculated based on the separated approach instead (Eq. (2.21)).

The inserts studied (not brazed to the tube wall) do not change the nucleate boiling contribution compared to the empty tube. This conclusion is also reached by studies with other inserts, e.g. most recently by Sajadi et al. [130] for wire-coil inserts. Therefore, the most suitable model for predicting the nucleate boiling contribution for the respective empty tube geometry and refrigerant should be used. In the present case, this is the Cooper equation (Eq. (2.17)).

The parity plot in Figure 4.34 illustrates the good description of the data by this simplified model approach, which does not require any fit factor. More than 90% of all data are described with an error of less than 30%. The deviations between model and experiment can be reduced if the description of the

wetting behavior and the description of the Reynolds number as a function of the wetting behavior are further improved. As shown in a previous work [127], no previously published model for describing the heat transfer in horizontal tubes with porous inserts is able to describe the experimental data available to date comparably well.

	10 ppi	20 ppi	hiTRAN
MPE	-7.5%	-2.2%	0.0%
MAPE	13.1%	9.4%	9.0%
APE < 30%	92.3%	93.6%	98.3%
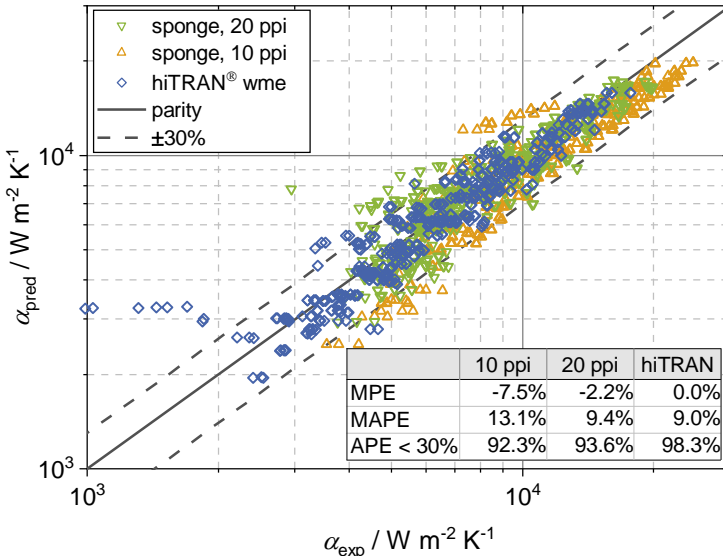
Figure 4.34 Parity plot of predicting the experimental heat transfer coefficient by the model described above for 10 ppi and 20 ppi sponge inserts as well as hiTRAN® wire matrix elements. The mean absolute percentage error (MAPE), the mean percentage error (MPE) and the absolute percentage error (APE) are defined in Appendix A. Figure adapted from a previous work [127].

5 Conclusion and outlook

Reliable predictive models for both heat transfer and pressure drop are required to evaluate the benefits of integrating porous structures into evaporator tubes and to design efficient heat exchangers. Most of the models suggested in literature require fitting parameters to adapt them to measurement data. However, only models that rely on established relationships and do not need fitting parameters can be transferred to inserts or operating conditions other than experimentally tested. In view of the large number of possible inserts, a prediction based on such a universal model is of great value. Consequently, the aim of this thesis was to test the following hypothesis:

The heat transfer and pressure drop of flow boiling in a horizontal tube with porous inserts can be described by physically reasonable combination of established models from the fields of "single-phase flow" and "boiling in empty tubes" - without using fitting parameters.

The hypothesis is accepted if the proposed models can describe more than 80% of the experimental data with an absolute percentage error of less than 30% and can additionally explain observed trends and influencing mechanisms.

Consequently, pressure drop and heat transfer tests were carried out with three different porous inserts at the flow boiling test facility at the Institute of Thermal Process Engineering (Karlsruhe Institute of Technology, KIT) using a newly designed test section. The horizontal test section (inner diameter 14 mm) measures the circumferentially resolved heat transfer coefficient at constant wall temperature. A sight glass combined with a high-speed camera enables the observation of the phase distribution of the investigated two-phase flow. Conclusions about the phase distribution can also be drawn from the variation of the wall temperature and the local heat transfer coefficient. This special design of the test section allows to test the hypothesis. Two sponge inserts with different cell sizes, approximately 10 ppi (pores per inch) and 20 ppi, and a wire matrix element (hiTRAN® by CALGAVIN Ltd. [33]) were investigated.

The realized operating conditions include saturation pressures from 1.2 MPa to 2.65 MPa (corresponding to saturation temperatures between -35 °C and -10 °C and to reduced pressures between 0.16 and 0.36), mass fluxes from 25 kg m^{-2} s^{-1} to 200 kg m^{-2} s^{-1}, vapor qualities from 5% to 98%, and temperature differences of up to 5 K (sponge inserts) and 7 K (hiTRAN® wire matrix elements). CO_2 was chosen as the experimental fluid.

The **pressure drop** of the two-phase flow in a tube with porous inserts was investigated under adiabatic and diabatic conditions. Investigating the dependence of the pressure drop on the operating conditions leads to following results:

- The dependence of the *adiabatic pressure* drop on the mass flux can be described well by a 2nd order polynomial ($b_1 \cdot \dot{m}_0 + b_2 \cdot \dot{m}_0{}^2$). This can be seen as a parallel to the Darcy-Forchheimer equation ($-dp/dz = \nu \cdot K^{-1} \cdot \dot{m}_0 + \beta \cdot \rho^{-1} \cdot \dot{m}_0^2$) describing the pressure drop of single-phase flow in porous media. It suggests that a suitable adaption of the single-phase law to two-phase flow may lead to a model without fitting parameter.

- Insufficient data are available for the exact determination of the linear term of the 2nd order polynomial. To minimize the influence of this term on the polynomial, only data measured at high mass fluxes were considered for further evaluation. In this range, the influence of the vapor quality, the saturation pressure, and the structure can be described by applying a homogeneous model approach to the quadratic Forchheimer term. This is implemented describing the density of the fluid with the homogeneous density, $\bar{\rho} = (\dot{x} \cdot \rho_V + (1 - \dot{x}) \cdot \rho_L)^{-1}$. The resulting Eq. (5.1). describes the dependence of the pressure drop on the single-phase Forchheimer coefficient, β, the vapor density, ρ_V, the liquid density, ρ_L, the vapor quality, $\dot{x}$, and the mass flux related to the empty tube cross-section, $\dot{m}_0$.

$$\left.\frac{dp}{dL}\right|_{tp,pm,ad} \approx \left.\frac{dp}{dL}\right|_{hom} = \beta \cdot \frac{1}{\bar{\rho}} \cdot \dot{m}_0^2 \tag{5.1}$$

For sponge inserts, this model can describe all experimental data at high mass fluxes ($\dot{m}_0 \geq 50$ kg m^{-2} s^{-1}) with an absolute percentage error (APE) of less than 30%. More than 88% of all experimental data for hiTRAN®

wire matrix elements and $\dot{m}_0 \geq 75 \text{ kg m}^{-2} \text{ s}^{-1}$ can be described with an APE < 30%. Consequently, for modeling the adiabatic pressure drop, the hypothesis is accepted in the stated parameter range.

- With an approach suggested by Storek and Brauer [60] for the pressure drop of two-phase flow in empty tubes, an even better description of the adiabatic pressure drop data of tubes with inserts could be achieved. Storek and Brauer multiplied the pressure drop calculated with the homogeneous model by an empirical correction function, Ω, according to Eq. (5.2).

$$\frac{dp}{dL} = \Omega \cdot \frac{dp}{dL}\bigg|_{\text{hom}} \qquad \textbf{(5.2)}$$

However, this correction function differs for empty tubes and tubes with inserts, since the use of an insert appears to minimize the deviation of the pressure drop from the homogeneous model. For porous inserts, the correction function is $\Omega \in [0.70; 1.15]$, while the correction function for the empty tube takes values between 0.30 and 2.10 for comparable operating conditions. Result of the present thesis indicate that the correction function for tubes with inserts probably depends mainly on the vapor quality, yet further experimental data of other geometries and operating conditions are needed for a statistically reliable support of this guess and to develop a reliable model.

- As in empty tubes, the additional pressure drop observed under *diabatic conditions* is proportional to the heat input between the pressure taps. However, the homogeneous empty tube model for the acceleration component of the pressure drop, Eq. (5.3), cannot explain the magnitude of the proportionality constant, which depends on the insert geometry. In addition to the mass flux, $\dot{m}_0$, the liquid density, ρ_{L}, the vapor density, ρ_{V}, the heat flux between the pressure taps, $\dot{q}^*$, the enthalpy of vaporization, Δh_{LV}, and the tube diameter, D_{i}, Eq. (5.3) takes into account the porosity of the inserts, ψ_{o}. Other geometric properties, such as the window diameter, are not considered but could potentially describe the magnitude of the proportionality

constant. For modeling the additional pressure drop under diabatic conditions, the hypothesis is thus rejected. Further investigations are needed to understand the underlying mechanisms and to propose sound models.

$$-\left(\frac{\mathrm{d}p}{\mathrm{d}z}\right)_{\mathrm{tp,et,acc}} = \frac{\dot{m}_0}{\psi_0^2} \cdot \left(\frac{1}{\rho_{\mathrm{L}}} - \frac{1}{\rho_{\mathrm{V}}}\right) \cdot \frac{4\,\dot{q}^*}{\Delta h_{\mathrm{LV}} \cdot D_{\mathrm{i}}} \qquad \text{(5.3)}$$

The **heat transfer coefficient** was measured locally in six segments distributed around the perimeter of the test section. The segments were electrically heated independently of each other. A constant wall temperature boundary condition was realized. Evaluation of the local heat transfer coefficient of the individual segment as a function of the local heat flux allows the influence of wetting to be distinguished from changes in the heat transfer mechanisms. The so obtained insight into the wetting behavior was compared to the variation of the wall temperature and to high-speed video recordings. For the latter, an image processing tool using MATLAB® was developed to determine the intensity of the phase boundary fluctuations which is difficult otherwise due to the transparency of both liquid and fluid phase. The following conclusions can be drawn from the analysis of the heat transfer and phase distribution measurements:

- For completely wetted segments, all structures and empty tubes behave similar for the same refrigerant at comparable operating conditions: the local heat transfer coefficients asymptotically approach the nucleate boiling contribution at *high heat fluxes,* described best by Cooper's model [4] for pool boiling in the form given in Eq. (5.4).

$$\frac{\alpha_{\mathrm{nb},j}}{\mathrm{W\,m^{-2}K^{-1}}} = 55 \cdot p_{\mathrm{r}}^{0.12} \cdot [-\log_{10} p_{\mathrm{r}}]^{-0.55} \cdot \left(\frac{\tilde{M}}{\mathrm{g\,mol^{-1}}}\right)^{-0.5} \cdot \left(\frac{\dot{q}_j}{\mathrm{W\,m^{-2}}}\right)^{0.67} \quad \text{(5.4)}$$

The accordance to Cooper's model is observed for all investigated operating conditions. Consequently, the inserts barely seem to influence the nucleate boiling contribution of the flow boiling heat transfer of completely wetted segments. The well-established Cooper's model can thus be used to

describe the flow boiling heat transfer coefficient in tubes with inserts at high heat fluxes.

- In contrast, the inserts increase the local heat transfer coefficient of completely wetted segments *at low heat fluxes* compared to the empty tube. This can be explained by an enhanced convective heat transfer. Single-phase heat transfer correlations describing the heat transfer at the tube wall with the respective inserts can describe the convective boiling contribution if adapted to two-phase flow. For sponge inserts, the model by Bianchi et al. [5] was successfully used to describe the experimental data. For hi-TRAN® wire matrix elements, a confidential inhouse correlation by CAL-GAVIN Ltd. [33] is suitable. The single-phase model by Bianchi et al. [5], Eq. (5.5), considers the window diameter of the insert, d_w, as well as the Reynolds number, Re, and Prandtl number, Pr, of the fluid flow.

$$Nu = \frac{\alpha \, d_w}{\lambda} = 1.97 + 0.09 \, (Re \cdot Pr)^{0.73} \qquad \textbf{(5.5)}$$

The adaption is achieved by using the liquid thermal conductivity, λ_L, the liquid Prandtl number, Pr_L, and a two-phase Reynolds number instead of the single-phase Reynolds number. Different approaches were tested. For the studied inserts, a homogeneous model approach ($Re_{tp,L,hom} = \dot{m}_0 \cdot \psi_o^{-1} \cdot L \cdot \bar{\rho}^{-1} \cdot v_L^{-1}$) best describes the convective contribution in the top segments, while a separated model approach ($Re_{tp,L,sep} = \dot{m}_0 \cdot \psi_o^{-1} \cdot (1 - \dot{x}) \cdot L \cdot \mu_L^{-1} \cdot (1 - \varepsilon)^{-1}$) is appropriate for the convective contribution in the bottom segments. This observation can be explained by the phase distribution and thus intrinsic velocities depending on the insert. Consequently, a physically meaningful adaption of single-phase laws can describe the heat transfer coefficient of flow boiling in tubes with porous inserts at low heat fluxes.

- The magnitude and trends observed for the heat transfer coefficient of a completely wetted segment, $\alpha_{tp,cw,j}$, in tubes with inserts can be described well by a cubic superposition of the nucleate boiling contribution, α_{nb}, and the convective boiling contribution, α_{cb}, according to Eq. (5.6).

$$\alpha_{\text{tp,cw},j} = \sqrt[3]{\alpha_{\text{nb}}(\dot{q}_j)^3 + \alpha_{\text{cb}}(Re_{\text{L,hom/sep},j})^3} \qquad \text{(5.6)}$$

The cubic superposition was suggested by Steiner and Taborek [98] for flow boiling heat transfer in vertical tubes and since then frequently applied to flow boiling heat transfer models of flow boiling in horizontal empty tubes [1,2,42,94].

- The heat transfer coefficient of partially wetted segments can be described by weighting the heat transfer coefficient of a dry arc, $\alpha_{\text{tp,dry},j}$, and the heat transfer coefficient of a completely wetted segment, $\alpha_{\text{tp,cw},j}$, according to Eq. (4.5). The heat transfer coefficient of the dry arc is described by the vapor heat transfer coefficient calculated using the same single-phase correlation as the convective boiling contribution, adjusted to two-phase flow using the homogeneous Reynolds number for the vapor phase ($Re_{\text{tp,V,hom}} = \dot{m} \cdot L \cdot \bar{\rho}^{-1} \cdot \nu_{\text{V}}^{-1}$). The dry fraction, $f_{\text{dry},j}$, depends on the insert structure and the operating conditions.

$$\alpha_{\text{tp,pw},j} = f_{\text{dry},j} \cdot \alpha_{\text{tp,dry},j} + \left(1 - f_{\text{dry},j}\right) \cdot \alpha_{\text{tp,cw},j} \qquad \text{(5.7)}$$

- The dependence of the dry fraction, and thus the dry angle, on the operating conditions is different for all investigated structures. In case of 20 ppi sponge inserts, the dry angle decreases with increasing homogeneous density and is independent on mass flux. This statement cannot be confirmed for 10 ppi sponges and hiTRAN® wire matrix elements. For the latter structures, no clear dependence of the dry angle on the operating conditions was found. In order to be able to describe these observations with a predictive model, further measurements with different inserts are necessary. Based on the experimental data of this thesis, the hypothesis thus cannot be accepted for the *local heat transfer coefficient* since the dry fraction, $f_{\text{dry},j}$, still needs to be fitted to the experimental results.

- The modeling approach derived from the preceding considerations to describe the *circumferentially averaged heat transfer coefficient* is summarized in Figure 4.33. In the absence of a mechanistic model, which should be established by future research, the approach proposed by Lu and Zhao [3] to predict the dry fraction, $f_{\mathrm{dry},j}$, was chosen. For this purpose, it is necessary to determine the stratified dry angle according to Biberg [100] and the void fraction according to the Rouhani drift-flux model [40]. The approach by Lu and Zhao [3] further relies on video observations to estimate the transition from partially to completely wetted circumference. The averaged dry angle is then interpolated based on the mass flux between the condition of stratified flow and completely wetted perimeter. To calculate the convective boiling contribution to the heat transfer coefficient along the wetted perimeter, α_{cb}, the single-phase heat transfer correlations describing the heat transfer coefficient at the tube wall adjacent to the insert is adapted to two-phase flow by applying either a homogeneous Reynolds number or a separated Reynolds number depending on the position at the tube perimeter. The nucleate boiling contribution to the heat transfer coefficient along the wetted perimeter, α_{nb}, is determined according to the model valid in the empty tube for the refrigerant used, in this case Cooper's model [4]. The vapor-phase heat transfer coefficient, $\alpha_{\mathrm{tp,v},j}$, which describes the heat transfer of the unwetted perimeter, $\alpha_{\mathrm{tp,dry},j}$, is modeled in a similar way as the convective contribution of the wetted perimeter, using the appropriate single-phase heat transfer correlation adapted to two-phase flow. Comparing the experimental data to the model reveals that more than 90% of all data are described with an error of less than 30% using this simplified model approach, which does not require any fitting parameter. Consequently, the hypothesis can be accepted for the circumferentially averaged heat transfer coefficient. Attention should be paid to high vapor qualities and heat fluxes because no model has been included that predicts the dryout and the departure from nucleate boiling.

In summary, the possibility was demonstrated to develop model approaches that are composed of the respective single-phase and empty tube concepts through appropriate adaptation. For this, only the single-phase correlations for pressure drop and wall heat transfer as well as the correlation for the nucleate

boiling heat transfer in the empty tubes have to be known. Open questions remain about the modeling of the additional pressure drop due to heating and the dry fraction to describe the local heat transfer coefficient.

Since the developed models are based on established concepts and refrain from the use of fitting parameters, transferability to other porous structures, tube diameters, refrigerants, and operating conditions can be anticipated. In addition to predicting flow boiling characteristics for the purpose of evaporator design or revamp, the models presented can also be applied to provide general predictions of the benefits of porous inserts.

6 References

[1]   N. Kattan, J.R. Thome, D. Favrat, Flow boiling in horizontal tubes: Part 3–Development of a new heat transfer model based on flow pattern, Journal of Heat Transfer (1998) 156–165. https://doi.org/10.1115/1.2830039.

[2]   S. Weise, B. Dietrich, T. Wetzel, Flow-pattern based prediction of flow boiling heat transfer in horizontal tubes with circumferentially varying heat flux, International Journal of Heat and Mass Transfer 148 (2020) 119018. https://doi.org/10.1016/j.ijheatmasstransfer.2019.119018.

[3]   W. Lu, C.Y. Zhao, Numerical Modelling of Flow Boiling Heat Transfer in Horizontal Metal-Foam Tubes, Adv. Eng. Mater. 11 (2009) 832–836. https://doi.org/10.1002/adem.200900139.

[4]   M.G. Cooper, Saturation nucleate pool boiling - A simple correlation, in: First U.K. National Conference on Heat Transfer, Pergamon, 1984, pp. 785–793.

[5]   E. Bianchi, G. Groppi, W. Schwieger, E. Tronconi, H. Freund, Numerical simulation of heat transfer in the near-wall region of tubular reactors packed with metal open-cell foams, Chem. Eng. J. 264 (2015) 268–279. https://doi.org/10.1016/j.cej.2014.11.055.

[6]   R.L. Webb, Performance evaluation criteria for use of enhanced heat transfer surfaces in heat exchanger design, Int. J. Heat Mass Transfer 24 (1981) 715–726. https://doi.org/10.1016/0017-9310(81)90015-6.

[7]   S. Liu, M. Sakr, A comprehensive review on passive heat transfer enhancements in pipe exchangers, Renewable and Sustainable Energy Reviews 19 (2013) 64–81. https://doi.org/10.1016/j.rser.2012.11.021.

[8]   C.Y. Zhao, Review on thermal transport in high porosity cellular metal foams with open cells, Int. J. Heat Mass Transfer 55 (2012) 3618–3632. https://doi.org/10.1016/j.ijheatmasstransfer.2012.03.017.

[9]   P. Drögemüller, The Use of hiTRAN Wire Matrix Elements to Improve the Thermal Efficiency of Tubular Heat Exchangers in Single and Two-Phase Flow, Chemie Ingenieur Technik 87 (2015) 188–202. https://doi.org/10.1002/cite.201400081.

[10]   A.E. Bergles, ExHFT for fourth generation heat transfer technology, Experimental Thermal and Fluid Science 26 (2002) 335–344. https://doi.org/10.1016/S0894-1777(02)00145-0.

[11]   G. Ribatski, F.T. Kanizawa, Chapter 1: Heat Transfer Enhancement Techniques Applied to Evaporation Processes, in: J.R. Thome, J. Kim (Eds.), Encyclopedia of Two-Phase Heat Transfer and Flow II: Boiling using Enhanced Surfaces, Plate Heat Exchangers and Two-Phase Devices, World Scientific Publishing Co. Pte. Ltd., 2015, pp. 1–51.

[12]   B. Madani, L. Tadrist, F. Topin, Experimental analysis of upward flow boiling heat transfer in a channel provided with copper metallic foam, Appl. Therm. Eng. 52 (2013) 336–344. https://doi.org/10.1016/j.applthermaleng.2012.11.046.

[13]   Y. Zhu, H. Hu, S. Sun, G. Ding, Flow boiling of refrigerant in horizontal metal-foam filled tubes: Part 2 – A flow-pattern based prediction method for heat transfer, Int. J. Heat Mass Transfer 91 (2015) 502–511. https://doi.org/10.1016/j.ijheatmasstransfer.2015.07.099.

[14]   Y. Zhu, H. Hu, S. Sun, G. Ding, Heat transfer measurements and correlation of refrigerant flow boiling in tube filled with copper foam, Int. J. Refrig. 38 (2014) 215–226. https://doi.org/10.1016/j.ijrefrig.2013.04.012.

[15]   G. Bamorovat Abadi, C. Moon, K.C. Kim, Flow boiling visualization and heat transfer in metal-foam-filled mini tubes – Part II: Developing predictive methods for heat transfer coefficient and pressure drop, Int. J. Heat Mass Transfer 98 (2016) 868–878. https://doi.org/10.1016/j.ijheatmasstransfer.2016.03.042.

[16]   K.N. Agrawal, H.K. Varma, S. Lal, Heat Transfer During Forced Convection Boiling of R-12 Under Swirl Flow, Journal of Heat Transfer 108 (1986) 567–573. https://doi.org/10.1115/1.3246972.

[17] M.A. Akhavan-Behabadi, R. Kumar, A. Mohammadpour, M. Jamali-Asthiani, Effect of twisted tape insert on heat transfer and pressure drop in horizontal evaporators for the flow of R-134a, International Journal of Refrigeration 32 (2009) 922–930. https://doi.org/10.1016/j.ijrefrig.2008.11.004.

[18] B. Madani, F. Topin, L. Tadrist, Influence du contact mousse-paroi sur les écoulements et les transferts de chaleur en ébullition convective, in: Annales du Congrès Annuel de la Société Française de Thermique, 2004.

[19] F. Topin, J.-P. Bonnet, B. Madani, L. Tadrist, Experimental Analysis of Multiphase Flow in Metallic foam: Flow Laws, Heat Transfer and Convective Boiling, Adv. Eng. Mater. 8 (2006) 890–899. https://doi.org/10.1002/adem.200600102.

[20] X. Ji, J. Xu, Experimental study on the two-phase pressure drop in copper foams, Heat Mass Transfer 48 (2012) 153–164. https://doi.org/10.1007/s00231-011-0860-2.

[21] H. Hu, Y. Zhu, G. Ding, S. Sun, Effect of oil on two-phase pressure drop of refrigerant flow boiling inside circular tubes filled with metal foam, Int. J. Refrig. 36 (2013) 516–526. https://doi.org/10.1016/j.ijrefrig.2012.10.037.

[22] H. Hu, Y. Zhu, H. Peng, G. Ding, S. Sun, Effect of tube diameter on pressure drop characteristics of refrigerant–oil mixture flow boiling inside metal-foam filled tubes, Appl. Therm. Eng. 62 (2014) 433–443. https://doi.org/10.1016/j.applthermaleng.2013.09.051.

[23] S. Weise, S. Meinicke, T. Wetzel, B. Dietrich, Modelling the pressure drop of two-phase flow through solid porous media, International Journal of Multiphase Flow 112 (2019) 13–26. https://doi.org/10.1016/j.ijmultiphaseflow.2018.12.005.

[24] A.E. Schael, Über das Strömungsverdampfen von CO_2 im glatten und innen berippten Rohr - Hydrodynamik, Wärmeübergang, Druckverlust, Ph.D. Thesis, Universität Fridericiana Karlsruhe (TH), Karlsruhe, 2009.

[25] J. Banhart, Manufacture, characterisation and application of cellular metals and metal foams, Progress in Materials Science 46 (2001) 559–632. https://doi.org/10.1016/S0079-6425(00)00002-5.

[26] A.N. Leonov, M.M. Dechko, Theory of design of foam ceramic filters for cleaning molten metals, Refractories and Industrial Ceramics 40 (1999) 537–542. https://doi.org/10.1007/BF02762637.

[27] B. Dietrich, Thermische Charakterisierung von keramischen Schwammstrukturen für verfahrenstechnische Apparate, Dissertation, Fakultät für Chemieingenieurwesen und Verfahrenstechnik des Karls-ruher Instituts für Technologie (KIT), 2010.

[28] P. Kumar, F. Topin, The geometric and thermohydraulic characteriza-tion of ceramic foams: An analytical approach, Acta Materialia 75 (2014) 273–286. https://doi.org/10.1016/j.actamat.2014.04.061.

[29] A. Inayat, H. Freund, T. Zeiser, W. Schwieger, Determining the spe-cific surface area of ceramic foams: The tetrakaidecahedra model revis-ited, Chem. Eng. Sci. 66 (2011) 1179–1188. https://doi.org/10.1016/j.ces.2010.12.031.

[30] D20 Committee, Test Method for Cell Size of Rigid Cellular Plastics, ASTM International, West Conshohocken, PA.

[31] P. Quadbeck, Fraunhofer Institute for Manufacturing Technology and Advanced Materials IFAM IFAM, Metallographic images, email, 2015.

[32] T. Lott, Micrographs of investment casted sponge struts, bachelor the-sis, 2016.

[33] CALGAVIN Ltd., hiTRAN® Thermal Systems, 2020, https://www.calgavin.com/products-and-software/hitran-thermal-sys-tems, accessed 10 November 2020.

[34] Y. Taitel, D. Barnea, Chapter 7 - The Drift Flux Model, in: J.R. Thome (Ed.), Encyclopedia of Two-Phase Heat Transfer and Flow I: Funda-mentals and methods, World Scientific Publishing Co. Pte. Ltd., 2015, pp. 185–194.

[35] Y. Taitel, D. Barnea, Chapter 6 - The Two Fluid Model, in: J.R. Thome (Ed.), Encyclopedia of Two-Phase Heat Transfer and Flow I: Fundamentals and methods, World Scientific Publishing Co. Pte. Ltd., 2015, pp. 131–184.

[36] Y. Taitel, D. Barnea, Chapter 2 - Basic Definitions of Two-Phase Flow Parameters, in: J.R. Thome (Ed.), Encyclopedia of Two-Phase Heat Transfer and Flow I: Fundamentals and methods, World Scientific Publishing Co. Pte. Ltd., 2015, pp. 9–14.

[37] M.A. Woldesemayat, A.J. Ghajar, Comparison of void fraction correlations for different flow patterns in horizontal and upward inclined pipes, International Journal of Multiphase Flow 33 (2007) 347–370. https://doi.org/10.1016/j.ijmultiphaseflow.2006.09.004.

[38] A. Cioncolini, J.R. Thome, Void fraction prediction in annular two-phase flow, International Journal of Multiphase Flow 43 (2012) 72–84. https://doi.org/10.1016/j.ijmultiphaseflow.2012.03.003.

[39] D. Steiner, Wärmeübertragung beim Sieden gesättigter Flüssigkeiten, in: VDI Wärmeatlas, 6th ed., VDI Verlag, Düsseldorf, 1991, Hbb.

[40] S.Z. Rouhani, Modified correlations for void fraction and two-phase pressure drop., RTV-841 p. 1/10, AB Atomenergi Sweden, 1969.

[41] N. Zuber, J.A. Findlay, Average Volumetric Concentration in Two-Phase Flow Systems, Journal of Heat Transfer 87 (1965) 453–468. https://doi.org/10.1115/1.3689137.

[42] L. Wojtan, T. Ursenbacher, J.R. Thome, Investigation of flow boiling in horizontal tubes: Part II–Development of a new heat transfer model for stratified-wavy, dryout and mist flow regimes, Int. J. Heat Mass Transfer 48 (2005) 2970–2985. https://doi.org/10.1016/j.ijheatmasstransfer.2004.12.013.

[43] F.T. Kanizawa, G. Ribatski, Two-phase flow patterns and pressure drop inside horizontal tubes containing twisted-tape inserts, International Journal of Multiphase Flow 47 (2012) 50–65. https://doi.org/10.1016/j.ijmultiphaseflow.2012.07.003.

[44] C.Y. Zhao, W. Lu, S.A. Tassou, Flow Boiling Heat Transfer in Horizontal Metal-Foam Tubes, J. Heat Transfer 131 (2009) 121002. https://doi.org/10.1115/1.3216036.

[45] J.R. Thome, A. Cioncolini, Chapter 6 - Two-Phase Pressure Drop: I: Fundamentals and methods, in: J.R. Thome (Ed.), Encyclopedia of Two-Phase Heat Transfer and Flow I: Fundamentals and methods, World Scientific Publishing Co. Pte. Ltd., 2015, pp. 143–176.

[46] F.T. Kanizawa, R.S. Hernandes, A. Moraes, G. Ribatski, A New Correlation for Single and Two-Phase Flow Pressure Drop in Round Tubes with Twisted-Tape Inserts, Journal of the Brazilian Society of Mechanical Sciences and Engineering 33 (2011) 243–250. https://doi.org/10.1590/S1678-58782011000500006.

[47] D.A. Nield, A. Bejan, Convection in Porous Media, Springer International Publishing, Cham, 2017.

[48] B. Niezgoda-Żelasko, Heat Transfer and Pressure Drop Measurements During Boiling in Vertical Tubes with Coiled-Wire Inserts, Heat Transfer Engineering 65 (2018) 1–16. https://doi.org/10.1080/01457632.2018.1480880.

[49] S. Whitaker, The Forchheimer equation: A theoretical development, Transport in Porous Media 25 (1996) 27–61.

[50] D.D. Joseph, D.A. Nield, G. Papanicolaou, Nonlinear equation governing flow in a saturated porous medium, Water Resour. Res. 18 (1982) 1049–1052. https://doi.org/10.1029/WR018i004p01049.

[51] J.-L. Auriault, On the domain of validity of Brinkman's equation, Transp Porous Med 79 (2009) 215–223. https://doi.org/10.1007/s11242-008-9308-7.

[52] N. Dukhan, M. Ali, Strong wall and transverse size effects on pressure drop of flow through open-cell metal foam, International Journal of Thermal Sciences 57 (2012) 85–91.

[53] G.S. Beavers, E.M. Sparrow, Compressible gas flow through a porous material, Int. J. Heat Mass Transfer 14 (1971) 1855–1859.

[54] D. Edouard, M. Lacroix, C.P. Huu, F. Luck, Pressure drop modeling on solid foam: State-of-the art correlation, Chem. Eng. J. 144 (2008) 299–311. https://doi.org/10.1016/j.cej.2008.06.007.

[55] P. Kumar, F. Topin, State-of-the-Art of Pressure Drop in Open-Cell Porous Foams: Review of Experiments and Correlations, J. Fluids Eng 139 (2017) 111401. https://doi.org/10.1115/1.4037034.

[56] P. Kumar, F. Topin, Influence of Morphology on Flow Law Characteristics in Open-Cell Foams: An Overview of Usual Approaches and Correlations, Journal of Fluids Engineering 139 (2017) 1–12. https://doi.org/10.1115/1.4036160.

[57] S. Woudberg, J.P. Du Plessis, An analytical Ergun-type equation for porous foams, Chem. Eng. Sci. 148 (2016) 44–54. https://doi.org/10.1016/j.ces.2016.03.013.

[58] A. Inayat, M. Klumpp, M. Lämmermann, H. Freund, W. Schwieger, Development of a new pressure drop correlation for open-cell foams based completely on theoretical grounds: Taking into account strut shape and geometric tortuosity, Chemical Engineering Journal 287 (2016) 704–719. https://doi.org/10.1016/j.cej.2015.11.050.

[59] B. Dietrich, W. Schabel, M. Kind, H. Martin, Pressure drop measurements of ceramic sponges—Determining the hydraulic diameter, Chem. Eng. Sci. 64 (2009) 3633–3640. https://doi.org/10.1016/j.ces.2009.05.005.

[60] H. Storek, H. Brauer, Reibungsdruckverlust der adiabaten Gas/Flüssigkeit-Strömung in horizontalen und vertikalen Rohren, Verein Deutscher Ingenieure: VDI-Forschungsheft 599, VDI-Verlag, Düsseldorf, 1980.

[61] H. Blasius, Das Aehnlichkeitsgesetz bei Reibungsvorgängen, Sonderabdruck aus der Zeitschrift des Vereines deutscher Ingenieure (1912) 639.

[62] P.K. Konakov, A New Correlation for the Friction Coefficient in Smooth Tubes, Berichte der Akademie der Wissenschaften der UdSSR LI (1946) 503–506.

[63] W.H. McAdams, Heat Transmission, 2nd ed., McGraw-Hill, New York, 1942.

[64] R.W. Lockhart, R.C. Martinelli, Proposed correlation of data for isothermal two-phase, two-component flow in pipes.

[65] L. Friedel, Improved friction pressure drop correlations for horizontal and vertical two phase pipe flow: Verbesserte Reibungsdruckabfallbeziehungen für horizontale und vertikale Gas-Dampf-Flüssigkeits-Rohrströmung, 3R International 18. Jahrgang (1979) 485–491.

[66] M. Wetzel, Influence of fully miscible lubrication oil on flow boiling of CO_2 inside horizontal evaporator tubes, PhD thesis, Karlsruher Institut für Technologie, Karlsruhe, 2017.

[67] H. Müller-Steinhagen, K. Heck, A simple friction pressure drop correlation for two-phase flow in pipes, Chem. Eng. Process 20 (1986) 297–308.

[68] J.G. Collier, J.R. Thome, Convective boiling and condensation, 3. ed. in paperback, repr ed., Oxford science publications 38, Clarendon Press, Oxford, 2001.

[69] A.E. Bergles, Recent developments in enhanced heat transfer, Heat Mass Transfer 47 (2011) 1001–1008. https://doi.org/10.1007/s00231-011-0872-y.

[70] P. Forchheimer, Wasserbewegung durch Boden, Zeitschrift des Vereins deutscher Ingenieure 45 (1901) 1736–1788.

[71] L. Tadrist, M. Miscevic, O. Rahli, F. Topin, About the use of fibrous materials in compact heat exchangers, Exp. Therm Fluid Sci. 28 (2004) 193–199. https://doi.org/10.1016/S0894-1777(03)00039-6.

[72] A. Inayat, J. Schwerdtfeger, H. Freund, C. Körner, R.F. Singer, W. Schwieger, Periodic open-cell foams: Pressure drop measurements and modeling of an ideal tetrakaidecahedra packing, Chem. Eng. Sci. 66 (2011) 2758–2763. https://doi.org/10.1016/j.ces.2011.03.031.

[73] K.N. Agrawal, H.K. Varma, S. Lal, Pressure Drop During Forced Convection Boiling of R-12 Under Swirl Flow, Journal of Heat Transfer 104 (1982) 758–762. https://doi.org/10.1115/1.3245196.

[74] M.K. Jensen, M. Pourdashti, H.P. Bensler, Two-phase pressure drop with twisted-tape swirl generators, International Journal of Multiphase Flow 11 (1985) 201–211.

[75] S. Weise, S. Klein, T. Wetzel, B. Dietrich, Pressure drop data of two-phase flow in a horizontal tube filled with metal sponge, KITopen repository, 2018, https://publikationen.bibliothek.kit.edu/1000085053.

[76] L. Wojtan, T. Ursenbacher, J.R. Thome, Investigation of flow boiling in horizontal tubes: Part I–A new diabatic two-phase flow pattern map, Int. J. Heat Mass Transfer 48 (2005) 2955–2969. https://doi.org/10.1016/j.ijheatmasstransfer.2004.12.012.

[77] Z. Wu, B. Sundén, Heat Transfer Correlations for Elongated Bubbly Flow in Flow Boiling Micro/Minichannels, Heat Transfer Engineering 37 (2016) 985–993. https://doi.org/10.1080/01457632.2015.1098269.

[78] S.G. Kandlikar, W.J. Grande, Evolution of Microchannel Flow Passages--Thermohydraulic Performance and Fabrication Technology, Heat Transfer Engineering 24 (2003) 3–17. https://doi.org/10.1080/01457630304040.

[79] W. Li, Z. Wu, A general criterion for evaporative heat transfer in micro/mini-channels, International Journal of Heat and Mass Transfer 53 (2010) 1967–1976. https://doi.org/10.1016/j.ijheatmasstransfer.2009.12.059.

[80] T. Harirchian, S.V. Garimella, A comprehensive flow regime map for microchannel flow boiling with quantitative transition criteria, International Journal of Heat and Mass Transfer 53 (2010) 2694–2702. https://doi.org/10.1016/j.ijheatmasstransfer.2010.02.039.

[81] L. Cheng, G. Ribatski, J. Moreno Quibén, J.R. Thome, New prediction methods for CO_2 evaporation inside tubes: Part I–A two-phase flow pattern map and a flow pattern based phenomenological model for two-

phase flow frictional pressure drops, Int. J. Heat Mass Transfer 51 (2008) 111–124. https://doi.org/10.1016/j.ijheatmasstransfer.2007.04.002.

[82] G. E. Alves, Co-current liquid-gas flow in a pipe-line contactor, Chemical Engineering Progress 50 (1954) 449–456.

[83] Y. Taitel, A.E. Dukler, A model for predicting flow regime transitions in horizontal and near horizontal gas-liquid flow, AIChE J. 22 (1976) 47–55. https://doi.org/10.1002/aic.690220105.

[84] N. Kattan, J.R. Thome, D. Favrat, Flow boiling in horizontal tubes: Part 1–Development of a diabatic two-phase flow pattern map, Journal of Heat Transfer (1998) 140–147. https://doi.org/10.1115/1.2830037.

[85] J.R. Thome, J. El Hajal, Two-phase flow pattern map for evaporation in horizontal tubes: Latest version, Heat Transfer Engineering 24 (2003) 3–10. https://doi.org/10.1080/714044410.

[86] R. Mastrullo, A.W. Mauro, J.R. Thome, D. Toto, G.P. Vanoli, Flow pattern maps for convective boiling of CO2 and R410A in a horizontal smooth tube: Experiments and new correlations analyzing the effect of the reduced pressure, International Journal of Heat and Mass Transfer 55 (2012) 1519–1528. https://doi.org/10.1016/j.ijheatmasstransfer.2011.11.003.

[87] G. Bamorovat Abadi, C. Moon, K.C. Kim, Flow boiling visualization and heat transfer in metal-foam-filled mini tubes – Part I: Flow pattern map and experimental data, Int. J. Heat Mass Transfer 98 (2016) 857–867. https://doi.org/10.1016/j.ijheatmasstransfer.2016.03.043.

[88] P. Drögemüller, M. Gough, Values and Benefits of Improving the Performance of Existing Heat Exchangers used in the Hydrocarbon Processing Industries, Chemical Engineering Transactions 61 (2017). https://doi.org/10.3303/CET1761312.

[89] Y. Zhu, H. Hu, S. Sun, G. Ding, Flow boiling of refrigerant in horizontal metal-foam filled tubes: Part 1 – Two-phase flow pattern visualization, Int. J. Heat Mass Transfer 91 (2015) 446–453. https://doi.org/10.1016/j.ijheatmasstransfer.2015.07.096.

[90] W. Lu, Investigations of heat transfer in metal-foam tubes, PhD thesis, Brunel University, London, 2008.

[91] VDI-Gesellschaft Verfahrenstechnik und Chemieingenieurwesen (Ed.), VDI-Wärmeatlas, 11th ed., Springer Berlin Heidelberg, Berlin, Heidelberg, 2013.

[92] H.D. Baehr, K. Stephan, Wärme- und Stoffübertragung, 8th ed., Springer, Berlin, Heidelberg, 2013.

[93] M. Kind, Strömungssieden: H3, in: VDI-Gesellschaft Verfahrenstechnik und Chemieingenieurwesen (Ed.), VDI Wärmeatlas, 11th ed., Springer Vieweg, Berlin, Heidelberg, 2013, pp. 895–1010.

[94] L. Cheng, G. Ribatski, L. Wojtan, J.R. Thome, New flow boiling heat transfer model and flow pattern map for carbon dioxide evaporating inside horizontal tubes, Int. J. Heat Mass Transfer 49 (2006) 4082–4094. https://doi.org/10.1016/j.ijheatmasstransfer.2006.04.003.

[95] J.R. Thome, J. El Hajal, Flow boiling heat transfer to carbon dioxide–General prediction method, Int. J. Refrig. 27 (2004) 294–301. https://doi.org/10.1016/j.ijrefrig.2003.08.003.

[96] S. Weise, S. Klein, R. Orias Calvo, F. Müller-Trefzer, T. Wetzel, B. Dietrich, Heat transfer data of two-phase flow in a horizontal tube filled with metal sponge, KITopen repository, 2019, https://publikationen.bibliothek.kit.edu/1000096098.

[97] F.W. Dittus, L.M.K. Boelter, Heat transfer in automobile radiators of the tubular type, University of California publications in engineering 2,13, Berkeley Univ. of California Press, 1930.

[98] D. Steiner, J. Taborek, Flow boiling heat transfer in vertical tubes correlated by an asymptotic model, Heat Transfer Engineering 13 (1992) 43–69.

[99] M.G. Cooper, Heat flow rates in saturated nucleate pool boiling - a wide-ranging correlation using reduced properties, Acvances in Heat Transfer 16 (1984) 157–239. https://doi.org/10.1016/S0065-2717(08)70205-3.

[100] D. Biberg, An explicit approximation for the wetted angle in two-Phase stratified pipe flow, The Canadian Journal of Chemical Engineering 77 (1999) 1221–1224. https://doi.org/10.1002/cjce.5450770619.

[101] J. El Hajal, J.R. Thome, A. Cavallini, Condensation in horizontal tubes: Part 1–Two-phase flow pattern map, Int. J. Heat Mass Transfer 46 (2003) 3349–3363. https://doi.org/10.1016/S0017-9310(03)00139-X.

[102] A. Žukauskas, Heat Transfer from Tubes in Crossflow, in: J.P. Hartnett, T.F. Irvine (Eds.), Advances in Heat Transfer, Elsevier, 1972, pp. 93–160.

[103] V.V. Calmidi, R.L. Mahajan, Forced Convection in High Porosity Metal Foams, American Society of Mechanical Engineers 122 (2000) 557–565.

[104] S. Meinicke, Understanding transport phenomena in consolidated, highly porous media a pore-scale CFD approach, PhD thesis, Karlsruhe Institute of Technology, Karlsruhe, 2019.

[105] M.A. Akhavan-Behabadi, R. Kumar, M. Jamali, Investigation on heat transfer and pressure drop during swirl flow boiling of R-134a in a horizontal tube, International Journal of Heat and Mass Transfer 52 (2009) 1918–1927. https://doi.org/10.1016/j.ijheatmasstransfer.2008.09.034.

[106] M.A. Akhavan-Behabadi, S.G. Mohseni, H. Najafi, H. Ramazanzadeh, Heat transfer and pressure drop characteristics of forced convective evaporation in horizontal tubes with coiled wire inserts, International Communications in Heat and Mass Transfer 36 (2009) 1089–1095. https://doi.org/10.1016/j.icheatmasstransfer.2009.07.009.

[107] L.T. Fan, S.T. Lin, N.Z. Azer, Augmentation of the rate of forced flow boiling heat transfer by means of in-line static mixers, Letters in Heat

and Mass Transfer 4 (1977) 425–428. https://doi.org/10.1016/0094-4548(77)90101-1.

[108] J. Lan, P.J. Disimile, J. Weisman, Two phase flow patterns and boiling heat transfer in tubes containing helical wire inserts: Part II - Critical heat flux studies, Journal of Enhanced Heat Transfer 4 (1997) 283–296. https://doi.org/10.1615/JEnhHeatTransf.v4.i4.40.

[109] J. Lan, P.J. Disimile, J. Weisman, Two phase flow patterns and boiling heat transfer in tubes containing helical wire inserts. Part I - Flow patterns and boiling heat transfer coefficients, Journal of Enhanced Heat Transfer 4 (1997) 269–281. https://doi.org/10.1615/JEnhHeatTransf.v4.i4.30.

[110] R.M. Manglik, A.E. Bergles, Characterization of Twisted-Tape-Induced Helical Swirl Flows for Enhancement of Forced Convective Heat Transfer in Single-Phase and Two-Phase Flows, Journal of Thermal Science and Engineering Applications 5 (2013) 21010.

[111] M. Shafaee, F. Alimardani, S.G. Mohseni, An empirical study on evaporation heat transfer characteristics and flow pattern visualization in tubes with coiled wire inserts, International Communications in Heat and Mass Transfer 76 (2016) 301–307. https://doi.org/10.1016/j.icheatmasstransfer.2016.06.001.

[112] R. Yun, J.-S. Hwang, J.T. Chung, Y. Kim, Flow boiling heat transfer characteristics of nitrogen in plain and wire coil inserted tubes, International Journal of Heat and Mass Transfer 50 (2007) 2339–2345. https://doi.org/10.1016/j.ijheatmasstransfer.2006.10.038.

[113] V.D. Zimparov, P.J. Penchev, Performance Evaluation of Some Tube Inserts as Heat Transfer Enhancement Techniques, Heat Transfer Engineering 27 (2006) 39–46. https://doi.org/10.1080/01457630600793988.

[114] J. Hammerschmidt, S. Scholl, Experimentelle Untersuchungen zum Einsatz von Drahtgestrickeinbauten und berippten Rohren in Naturumlaufverdampfern, Chemie Ingenieur Technik 84 (2012) 1939–1947. https://doi.org/10.1002/cite.201200016.

[115] H. Hu, Y. Zhu, H. Peng, G. Ding, S. Sun, Influence of tube diameter on heat transfer characteristics of refrigerant-oil mixture flow boiling in metal-foam filled tubes, Int. J. Refrig. 41 (2014) 121–136. https://doi.org/10.1016/j.ijrefrig.2014.01.005.

[116] Y. Zhu, H. Hu, G. Ding, S. Sun, Y. Jing, Influence of metal foam on heat transfer characteristics of refrigerant-oil mixture flow boiling inside circular tubes, Appl. Therm. Eng. 50 (2013) 1246–1256. https://doi.org/10.1016/j.applthermaleng.2012.06.045.

[117] G. Bamorovat Abadi, K.C. Kim, Enhancement of phase-change evaporators with zeotropic refrigerant mixture using metal foams, Int. J. Heat Mass Transfer 106 (2017) 908–919. https://doi.org/10.1016/j.ijheatmasstransfer.2016.10.039.

[118] H.Y. Li, K.C. Leong, Experimental and numerical study of single and two-phase flow and heat transfer in aluminum foams, Int. J. Heat Mass Transfer 54 (2011) 4904–4912. https://doi.org/10.1016/j.ijheatmasstransfer.2011.07.002.

[119] R.F. Lopina, A.E. Bergles, Heat Transfer and Pressure Drop in Tape - Generated Swirl Flow of Single-Phase Water, ASME Journal of Heat Transfer 91 (1969) 434–441. https://doi.org/10.1115/1.3580212.

[120] Gherhardt Ribatski, Fabio Toshio Kanizawa, Encyclopedia of Two-Phase Heat Transfer and Flow II: Chapter 1: Heat Transfer Enhancement Techniques Applied to Evaporation Processes, World Scientific Publishing Co. Pte. Ltd., 5 Toh Tuck Link, Singapore 596224, 2005.

[121] K.C. Leong, H.Y. Li, L.W. Jin, J.C. Chai, Convective Heat Transfer in Graphite Foam Heat Sinks With Baffle and Stagger Structures, JOURNAL OF HEAT TRANSFER-TRANSACTIONS OF THE ASME 133 (2011). https://doi.org/10.1115/1.4003449.

[122] A. Diani, S. Mancin, L. Doretti, L. Rossetto, Low-GWP refrigerants flow boiling heat transfer in a 5 PPI copper foam, International Journal of Multiphase Flow 76 (2015) 111–121. https://doi.org/10.1016/j.ijmultiphaseflow.2015.07.003.

[123] M. Niederkrüger, Strömungssieden von reinen Stoffen und binären ze-
otropen Gemischen im waagerechten Rohr bei mittleren und hohen
Drücken, PhD thesis, 1991.

[124] P. Quadbeck, Open cell metal foams, http://www.ifam.fraunho-
fer.de/content/dam/ifam/en/documents/dd/In-
fobl%C3%A4tter/open_cell_metal_foams_fraunhofer_ifam_dres-
den.pdf.

[125] Joint Committee for Guides in Metrology, Evaluation of measurement
data—Guide to the expression of uncertainty in measurement, GUM
1995 with minor corrections, https://www.bipm.org/utils/common/doc-
uments/jcgm/.

[126] R. Span, W. Wagner, A new equation of state for carbon dioxide cover-
ing the fluid region from the triple-point temperature to 1100 K at pres-
sures up to 800 MPa, J. Phys. Chem. Ref. Data 25 (1996) 1509–1596.
https://doi.org/10.1063/1.555991.

[127] S. Weise, T. Wetzel, B. Dietrich, Influence of porous inserts on flow
boiling heat transfer in horizontal tubes, Int. J. Heat Mass Transfer 171
(2021) 121087. https://doi.org/10.1016/j.ijheatmasstrans-
fer.2021.121087.

[128] V. Gnielinski, Durchströmte Rohre: G1, in: VDI-Gesellschaft Verfah-
renstechnik und Chemieingenieurwesen (Ed.), VDI Wärmeatlas, 11th
ed., Springer Vieweg, Berlin, Heidelberg, 2013, pp. 785–792.

[129] V. Gnielinski, On heat transfer in tubes, Int. J. Heat Mass Transfer 63
(2013) 134–140. https://doi.org/10.1016/j.ijheatmasstrans-
fer.2013.04.015.

[130] B. Sajadi, M.M. Najafizadeh, M. Soleimani, M.A. Akhavan Behabadi,
J. Naserinejad, The effect of wire-coil inserts on the heat transfer and
pressure drop of R1234yf flow boiling, Applied Thermal Engineering
152 (2019) 615–623. https://doi.org/10.1016/j.ap-
plthermaleng.2019.02.115.

[131] A. Bejan, G. Tsatsaronis, M. Moran, Thermal design and optimization, John Wiley & Sons, New York, Chichester, Brisbane, Toronto, Singapore, 1996.

[132] S.M. Zubair, P.V. Kadaba, R.B. Evans, Second-law-based thermoeconomic optimization of two-phase heat exchangers, Journal of Heat Transfer 109 (1987) 287–294. https://doi.org/10.1115/1.3248078.

[133] D.V. Schroeder, An introduction to thermal physics, Pearson Education Limited, Edinburgh, 2014.

[134] A. Bejan, Entropy generation minimization: The method of thermodynamic optimization of finite-size systems and finite-time processes, Advanced topics in mechanical engineering series, CRC Press, Boca Raton, Fla., 1996.

[135] K. Manjunath, S.C. Kaushik, Second law thermodynamic study of heat exchangers: A review, Renewable and Sustainable Energy Reviews 40 (2014) 348–374. https://doi.org/10.1016/j.rser.2014.07.186.

[136] A. Cavallini, J.S. Brown, D. Del Col, C. Zilio, In-tube condensation performance of refrigerants considering penalization terms (exergy losses) for heat transfer and pressure drop, Int. J. Heat Mass Transfer 53 (2010) 2885–2896. https://doi.org/10.1016/j.ijheatmasstransfer.2010.02.007.

[137] J. Steven Brown, C. Zilio, R. Brignoli, A. Cavallini, Heat transfer and pressure drop penalization terms (exergy losses) during flow boiling of refrigerants, Int. J. Energy Res. 37 (2013) 1669–1679. https://doi.org/10.1002/er.2989.

[138] T.S. Mogaji, F.T. Kanizawa, E.P. Bandarra Filho, G. Ribatski, Experimental study of the effect of twisted-tape inserts on flow boiling heat transfer enhancement and pressure drop penalty, Int. J. Refrig. 36 (2013) 504–515. https://doi.org/10.1016/j.ijrefrig.2012.10.008.

Appendix A   Calculation of error

The following error definitions apply for use in the error statistics. $\alpha_{\text{pred},k}$ is the predicted heat transfer coefficient at the operating condition k while $\alpha_{\text{exp},k}$ is the experimentally determined heat transfer coefficient. n is the number of different operating conditions. The same definitions are valid for the pressure drop per unit length, $\Delta p / \Delta L$.

percentage error (PE)

$$PE = \frac{\alpha_{\text{pred},k} - \alpha_{\text{exp},k}}{\alpha_{\text{exp},k}} \tag{A.8}$$

mean percentage error (MPE)

$$MPE = \frac{1}{n} \sum_{k=1}^{n} \frac{\alpha_{\text{pred},k} - \alpha_{\text{exp},k}}{\alpha_{\text{exp},k}} \tag{A.9}$$

absolute percentage error (APE)

$$APE = \left| \frac{\alpha_{\text{pred},k} - \alpha_{\text{exp},k}}{\alpha_{\text{exp},k}} \right| \tag{A.10}$$
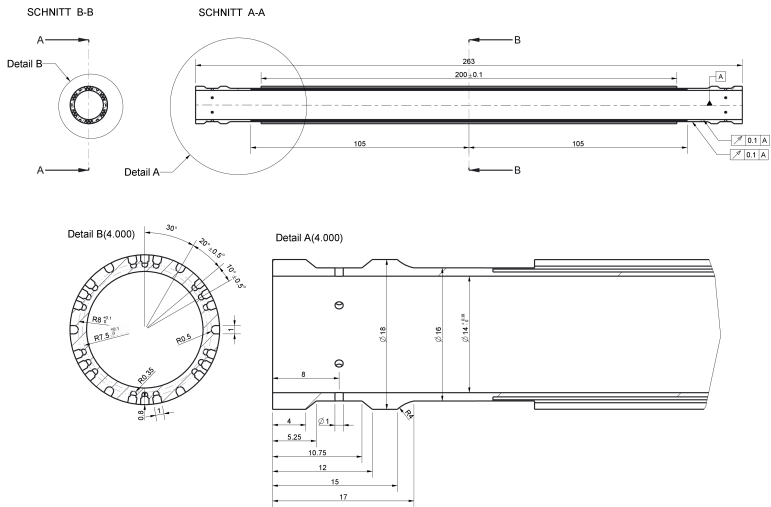
mean absolute percentage error (MAPE)

$$MAPE = \frac{1}{n} \sum_{k=1}^{n} \left| \frac{\alpha_{\text{pred},k} - \alpha_{\text{exp},k}}{\alpha_{\text{exp},k}} \right| \tag{A.11}$$
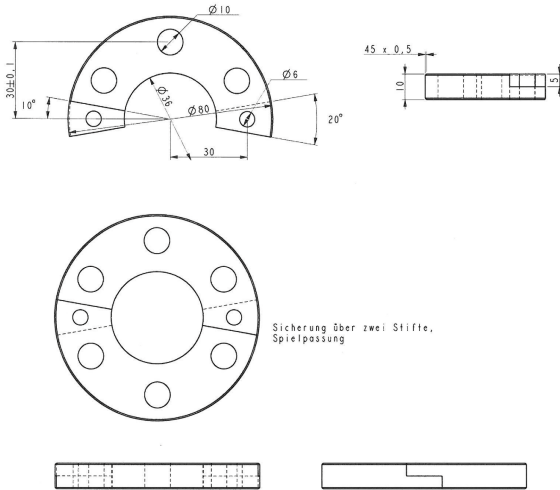
Appendix B   Test section and inserts

## B.1   Technical drawing of test section

Figure B.1: Longitudinal section as well as cross section of the test tube. Measuring tube is made of brass CuZn39Pb3. Overall tolerance: ISO 2768-f.
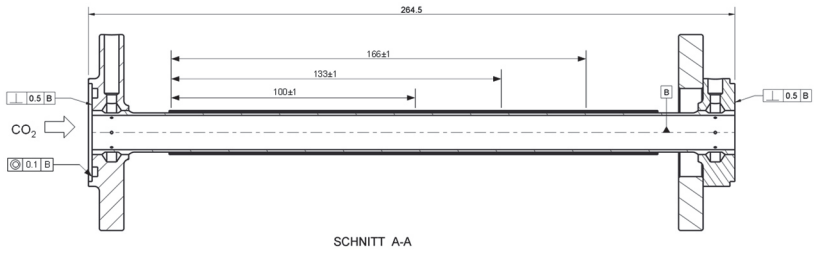
Figure B.2: Pressure tap soldered to test tube made of stainless steel. Overall tolerance: ISO 2768-f.

Figure B.3: Separable loose flange made of stainless steel. Overall tolerance: ISO 2768-f.
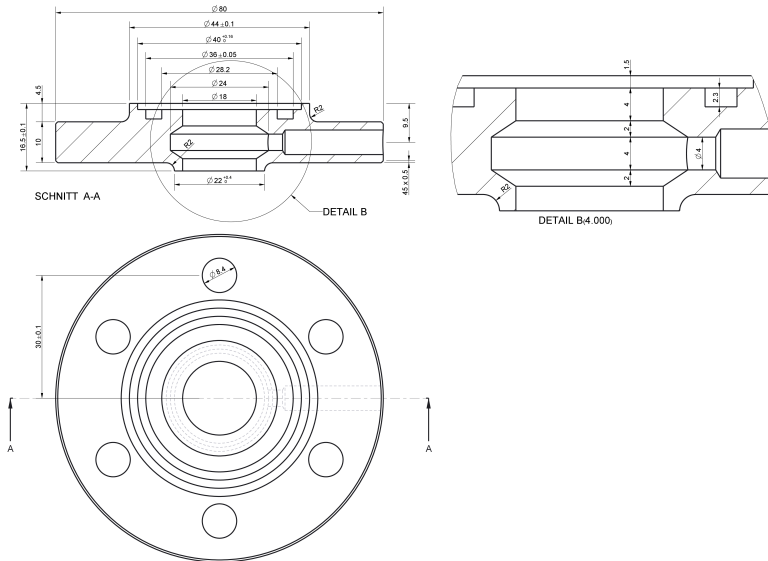
Figure B.4: Pressure tap and fixed flange soldered to test tube made of stainless steel. Overall tolerance: ISO 2768-f.

Figure B.5: Test section assembly with fixed flange at the inlet and loose flange at the outlet of the test section.

B.2 Thermal conductivity of brass

The thermal conductivity of the test section, λ_{ts}, is necessary for calculating the wall temperature from the temperature measured by the thermocouples (compare Eq. (3.4) in Section 3.4.5). To determine the thermal conductivity of the brass used for the test section, a sample of the same brass batch was examined. The thermal conductivity was determined indirectly by measuring the thermal diffusivity, κ, the specific heat capacity, c_p, and density, ρ, of the sample. The functional correlation between these measures is given by Eq. (B.1).

$$\lambda_{ts} = \kappa \cdot c_p \cdot \rho \qquad \textbf{(B.1)}$$

The thermal diffusivity is measured by laser flash analysis at the Institute of Applied Materials at Karlsruhe Institute of Technololgy for temperatures between 21 °C and 45 °C, compare Figure B.6.
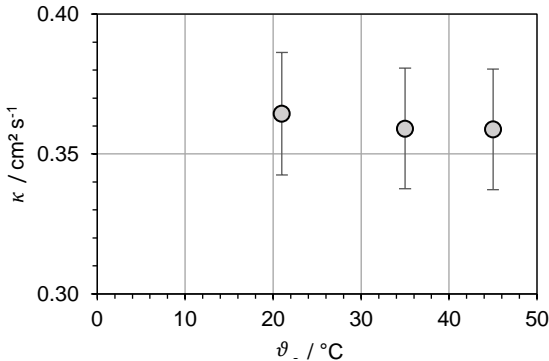
Figure B.6: Thermal diffusivity of brass test section as a function of the temperature. The error bars indicate the standard uncertainty of 10 individual measurements at the respective temperature.

The specific heat capacity is measured by differential scanning calorimetry (DSC Q2000 by TA Instruments) at the Institute of Thermal Process Engineering at Karlsruhe Institute of Technology for temperatures between -40 °C and 46 °C, compare Figure B.7.
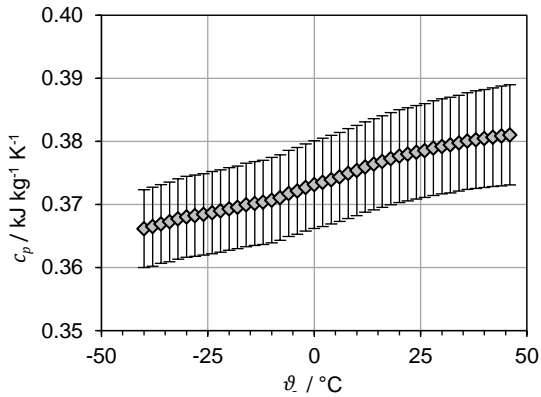
Figure B.7: Specific heat capacity of brass test section as a function of the temperature. The error bars indicate the standard uncertainty of 3 individual measurements at the respective temperature.

The density of the brass sample was measured by means of a hydrostatic measuring principle using the analytical balance CPA 225 D by Sartorius. It is 8272.4 kg m^{-3} $\pm$ 0.3 kg m^{-3} (measurement uncertainty, $k = 1$) at 23.5 °C. The temperature dependence is estimated.

The resulting thermal conductivity of the test section is 113.5 W m^{-1} K^{-1} at 23.5 °C with an estimated measurement uncertainty ($k = 1$) of 7.2 W m^{-1} K^{-1}.

# B.3   Measurement uncertainty of wall temperature

The measurement uncertainty of the inner wall temperature is influenced by the temperature inhomogeneity at the tube wall and the deviation of the mean inner tube wall temperature from the estimation by one-dimensional heat conduction in a cylindrical shell segment, compare Eq. (3.4). To estimate the order of magnitude of these two contributions to the measurement uncertainty, a 2D heat conductivity simulation of the test section cross-section is performed using Simcenter STAR-CCM+ (version 9.04.009).

Figure B.7 illustrates the simulated cross section as well as the most important features of the simulation. The complete cross section is simulated to be able to set boundary conditions as a function of the segment as it will be encountered in two-phase heat transfer coefficient measurements. The solder and the thermocouple influence the temperature field due to their thermal conductivity differing from that of the brass tube. The solder and the thermocouples are thus simulated as well. The mesh was generated using the polyhedral mesher and the surface remesher. The basis cell size of the solder and the thermocouples is much smaller than that of the brass tube. The cell size and the abortion criterion (energy minimum = 1E-6) were determined by mesh independence studies allowing the results to differ less than 0.005 K.
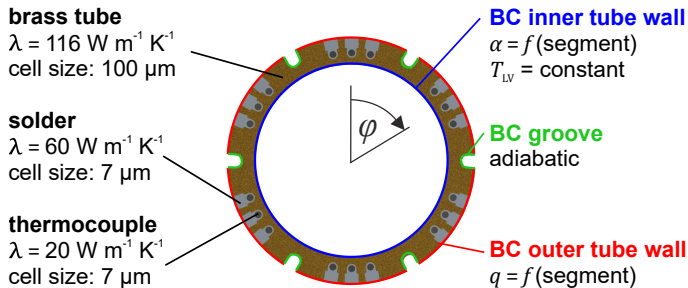
Figure B.8: Material and mesh properties of simulated standard 2D model of the test section as well as illustration of boundary conditions (BC) at inner and outer tube wall.

To assess the extent of the two influences explained at the beginning of this section, the difference between the wall temperature calculated from the simulation results according to Eq. (3.4), T_{calc}, and the wall temperature resulting from the boundary condition, T_{bc}, is determined. T_{bc} is considered to be the correct wall temperature and T_{calc} simulates the value determined by measurement. The heat fluxes set in four different representative two-phase heat transfer measurements (#1 to #4) as well as the heat transfer coefficients reported there are used as boundary conditions in the simulation and to calculate T_{bc}. The fluid temperature is set to -10 °C, however, the results are independent of the temperature level. Figure B.9 illustrates that this temperature difference is independent of the heat flux. This can be explained by the fact that it is dominated by the temperature inhomogeneity, which also depends on the temperature profile of the neighboring segment. To account for this effect, a mean standard uncertainty (k =1) of 0.13 K is assumed in the measurement uncertainty analysis according to the GUM [125].
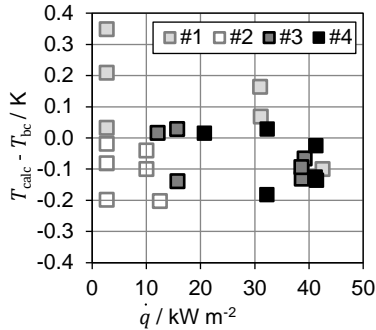

Figure B.9: Difference between the inner wall temperature calculated by Eq. (3.4) and inner wall temperature as defined by the boundary condition as a function of the local heat flux.

137

Appendix C   Single-phase heat transfer measurements

Figure C.1 shows the comparison between the experimental single-phase Nusselt number, Nu, characterizing the heat transfer at the wall of a tube with a 20 ppi sponge insert and the correlation by Bianchi et al. [5]. The experimental procedure corresponds to the experimental procedure of the single-phase validation experiments as explained in Section 3.5 (determination of heat input by method A). The correlation by Bianchi et al. [5] is explained in Section 2.5.2.
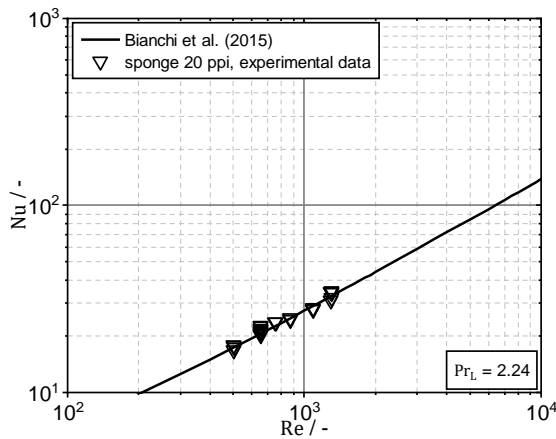
Figure C.1: Comparison of experimentally determined single-phase Nusselt number characterizing the heat transfer at a tube wall with 20 ppi sponge inserts with the correlation by Bianchi et al. [5], Eq. (2.25).

Appendix D Performance enhancement criteria for flow boiling

D.1 Entropy generation

In order to optimize the total cost of a heat exchanger, several authors [131,132] propose to model the operating and capital expenses depending on the rate of entropy generation, $\dot{S}_{\mathrm{gen}}$, and the entropy lost to the environment. This approach is called thermo-economic optimization. [131]

Entropy is a measure for the multiplicity, i.e., the number of possible microstates for one macrostate. Entropy always increases (second law of thermodynamics) for a closed, adiabatic system. [133] The rate of entropy generation, $\dot{S}_{\mathrm{gen}}$, is a measure for the system's departure from reversibility. In a heat exchanger entropy is generated due to heat transfer and pressure drop and lost by parasitic heat transfer to the environment. [134]

The operating expenses due to generated entropy, C_S^O, of a heat exchanger with streams A and B can be described e.g. by Eq. (D.1) [132]. Here n_h is the expected number of operating hours, T_0 the ambient temperature, $\dot{S}_{\mathrm{gen},i}$ the generated entropy associated with mechanism i, and $c_{\mathrm{S},i}$ the unit cost of lost exergy ($T_0\,\dot{S}_{\mathrm{gen}}$).

$$C_S^O \;=\; n_h\,T_0\big(c_{\mathrm{S},\Delta T}\dot{S}_{\mathrm{gen},\Delta T} + c_{\mathrm{S},\Delta P_\mathrm{A}}\dot{S}_{\mathrm{gen},\Delta P_\mathrm{A}} + c_{\mathrm{S},\Delta P_\mathrm{B}}\dot{S}_{\mathrm{gen},\Delta P_\mathrm{B}}\big) \qquad \textbf{(D.1)}$$

One should thus bear in mind that the optimization of a subsystem does not correspond to the optimization of the overall system [131], the cost-optimal design does not necessarily match the design with a minimum entropy generation rate [131], and the specific costs attributed to entropy generation due to heat transfer or pressure drop do not have to be the same [132], although this

is a common assumption [131]. Consequently, the analysis of entropy gener-
ated in a subsystem should not be used for a general evaluation of an enhance-
ment method. However, such an analysis may give an indication of possible
optimization measures, e.g., if the expenses due to irreversibility are signifi-
cant, minimizing them may also lead to minimized overall costs.

Different "Performance Enhancement Criteria (PEC)" were thus defined to
evaluate the influence of heat transfer and pressure drop, see e.g. a review by
Manjunath [135]. The criteria can be classified into simple relations most no-
tably the "Enhancement Parameter" and 2nd law criteria such as "Entropy
Generation Minimization", "Exergy analysis" and "Total Temperature Penali-
zation". In the following, these concepts will be discussed.

The generated entropy due to heat transfer and pressure drop in an evaporator
tube is calculated by approach following the example of Bejan [134].
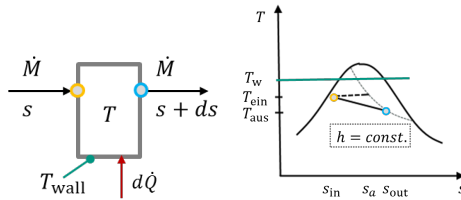
Figure D.1: Balance boundaries of infinitesimal small element of evaporator tube (steady state),
and illustration of the inlet and outlet state in the T-s-diagram. Also shown is an
auxiliary state with the inlet temperature but the outlet enthalpy.

For steady state, the mass balance and the energy balance for an infinitesimal
small volume of an evaporator tube can be written as follows:

$$d\dot{M} = 0 \tag{D.2}$$

$$\frac{dH}{dz} = \dot{M}\frac{dh}{dz} = \frac{d\dot{Q}}{dz} \tag{D.3}$$

The generated entropy rate is the entropy leaving the system minus the entropy
entering the system due to heat transfer or mass flux.

$$\frac{d\dot{S}_{\text{gen}}}{dz} = -\frac{1}{T_{\text{w}}}\frac{d\dot{Q}}{dz} + \dot{M}\frac{ds}{dz} \tag{D.4}$$

Using the fundamental thermodynamic relation Eq. (D.5), the change of state can be modeled as Eq. (D.6). This equation can be viewed as the description of two processes: the first at constant pressure, the second at constant enthalpy.

$$ds = \frac{1}{T}dh - \frac{v}{T}dP \tag{D.5}$$

$$\frac{d\dot{S}_{\text{gen}}}{dz} = -\frac{d\dot{Q}\ (T_{\text{w}} + T)}{T_{\text{w}} \cdot T} + \dot{M}\left(\frac{1}{T}\frac{dh}{dz} - \frac{v}{T}\frac{dP}{dz}\right) \tag{D.6}$$

Now, substituting Eq. (D.3) into Eq. (D.6) and combining the first two terms of Eq. (D.6) leads to Eq. (D.7). Now, the first term describes the entropy generated due to the temperature difference between the wall and the bulk. The second term is related to the pressure drop inside the volume element.

$$\frac{d\dot{S}_{\text{gen}}}{dz} = \frac{(T_{\text{w}} - T)}{T_{\text{w}} \cdot T}\frac{d\dot{Q}}{dz} - \dot{M}\frac{v}{T}\frac{dP}{dz} \tag{D.7}$$

The specific volume at constant enthalpy, v, can be expressed by the specific volume $\tilde{v}$ of the two-phase flow by Eq. (D.8). Here, a small inaccuracy is introduced as the vapor quality changes slightly with changing pressure at constant enthalpy.

$$v = v_{\text{L}} + (\dot{x} + d\dot{x})v_{\text{VL}} \tag{D.8}$$

The temperature difference between the wall and the bulk fluid is denoted with $\Delta T_{\dot{Q}}$. As $\Delta T \ll T$, a common simplification is to write $T_{\text{w}} \cdot T \approx T^2$.

$$\frac{d\dot{S}_{\text{gen}}}{dz} = \frac{\Delta T_{\dot{Q}}}{T^2}\frac{d\dot{Q}}{dz} - \dot{M}\frac{v}{T}\frac{dP}{dz} \tag{D.9}$$

In case of a constant wall temperature in the direction of the mass flux, Bejan [134] integrates Eq. (D.9). Note that the specific volume is evaluated at the inlet pressure, P_{in}, and the outlet vapor quality, $\dot{x}_{\text{out}}$.

$$\dot{S}_{\text{gen}} = \dot{Q}\frac{\Delta T_{\dot{Q}}}{T^2} - \dot{M}\frac{\tilde{v}(P_{\text{in}}, \dot{x}_{\text{out}})}{T}\Delta P \tag{D.10}$$

Another notation can be gained if the pressure drop is substituted by a linearized Clausius-Clapeyron Equation (D.11) and complete evaporation ($\dot{x}_{\text{in}} = 0$; $\dot{x}_{\text{out}} = 1$).

$$\frac{dP}{dT} \approx \frac{\Delta P}{\Delta T} = \frac{\Delta h^{\text{LV}}}{v^{\text{VL}} \cdot T} \approx \frac{\Delta h^{\text{LV}}}{v^{\text{V}} \cdot T} \tag{D.11}$$

$$\dot{S}_{\text{gen}} = \frac{\dot{Q}}{T^2} (\Delta T_{\dot{Q}} + \Delta T_{\Delta P}) \tag{D.12}$$

However, integrating at constant wall temperature for complete evaporation but weighing the pressure drop with the respective specific volume of each infinitesimal volume element leads to Eq. (D.13), which is similar to Eq. (D.12), but differs by a factor $a < 1$, depending on the pressure drop characteristics.

$$\dot{S}_{\text{gen}} = \frac{\dot{Q}}{T^2} (\Delta T_{\dot{Q}} + a\, \Delta T_{\Delta P}) \tag{D.13}$$

Such an expression is used e.g. by Cavallini et al. [136], Brown et al. [137] or Zubair et al. [132] with $a = 0.5$. Cavallini et al. call this performance enhancement criterium "Total Temperature Penalization".

To evaluate the merit of a heat transfer augmentation technique, Bejan and Pfister suggest the comparison of the rate of entropy generation of the heat exchange apparatuses before ($\dot{S}_{\text{gen,o}}$) and after ($\dot{S}_{\text{gen,a}}$) the implementation of the augmentation technique. The "Augmentation Entropy Generation Number" is defined by Eq. (D.14).

$$N_{s,a} = \frac{\dot{S}_{\text{gen,a}}}{\dot{S}_{\text{gen,o}}} \tag{D.14}$$

D.2 Enhancement parameter

An example of the other class of Performance Enhancement Criteria is the enhancement parameter $\varepsilon = \varepsilon_{\dot{Q}} / \varepsilon_{\Delta P}$, e.g. used by Webb (1994), Agrawal and

Varma (1990) apud Mogaji et al. [138]. The "Enhancement Factor", ε_q, [136,138] is defined as

$$\varepsilon_q = EF = \left.\frac{\alpha}{\alpha_{\text{empty tube}}}\right|_{\dot{x},\dot{m},\dot{q}} \tag{D.15}$$

The "Pressure Penalization" or "Pressure Drop Penalty" [136,138] is defined as

$$\varepsilon_p = PP = \left.\frac{\frac{\Delta p}{\Delta L}}{\left(\frac{\Delta p}{\Delta L}\right)_{\text{empty tube}}}\right|_{\dot{x},\dot{m},\dot{q}} \tag{D.16}$$

If the Enhancement Parameter is larger than unity, the effectivity measure to enhance the heat transfer is typically rated positive. Comparing these criteria with the "Entropy Generation Minimization" and the "Total Temperature Penalization", one can recognize that such an assumption can only be valid if the entropy generated by heat transfer is in the same order of magnitude than the entropy generated by pressure drop. According to Bejan [134], the irreversibility distribution ratio ($\phi = \dot{S}_{\text{gen},\Delta P}/\dot{S}_{\text{gen},\dot{Q}}$) has a theoretical optimum at 0.168. However, according to Zubair et al. [132], the lost work due to a finite temperature difference of a two-phase heat exchanger is generally much larger than the values for the two-phase pressure drop.

Own publications and conference contributions

Quotable publications

S. Weise, T. Wetzel, B. Dietrich, Influence of porous inserts on flow boiling heat transfer in horizontal tubes, Int. J. Heat Mass Transfer 171 (2021) 121087. https://doi.org/10.1016/j.ijheatmasstransfer.2021.121087.

S. Weise, B. Dietrich, T. Wetzel, Flow-pattern based prediction of flow boiling heat transfer in horizontal tubes with circumferentially varying heat flux, Int. J. Heat Mass Transfer 148 (2020) 119018. https://doi.org/10.1016/j.ijheatmasstransfer.2019.119018.

S. Weise, S. Meinicke, T. Wetzel, B. Dietrich, Modelling the pressure drop of two-phase flow through solid porous media, Int. J. Multiphase Flow 112 (2019) 13–26. https://doi.org/10.1016/j.ijmultiphaseflow.2018.12.005.

S. Weise, S. Klein, R. Orias Calvo, F. Müller-Trefzer, T. Wetzel, B. Dietrich, Heat transfer data of two-phase flow in a horizontal tube filled with metal sponge, KITopenData, Karlsruhe, 2019, https://publikationen.bibliothek.kit.edu/1000096098.

S. Weise, S. Klein, T. Wetzel, B. Dietrich, Pressure drop data of two-phase flow in a horizontal tube filled with metal sponge, KITopenData, Karlsruhe, 2018, https://publikationen.bibliothek.kit.edu/1000085053.

S. Weise, T. Wetzel, B. Dietrich, Experimental investigation of two-phase flow boiling inside porous media, in: Proc. of the 16th International Heat Transfer Conference, Peking, 2018 (IHTC16-23421)

S. Weise, M. Wetzel, B. Dietrich, T. Wetzel, Influence of fully miscible lubricating oil on the pressure drop during flow boiling of CO_2 inside an enhanced tube, Exp. Therm. Fluid Sci. 81 (2017) 223-233. https://doi.org/10.1016/j.expthermflusci.2016.09.018.

S. Weise, M. Wetzel, M. Hornberger, B. Dietrich, T. Wetzel, Experimental investigation of the influence of lubricating oil on the flow boiling heat transfer and pressure drop of CO_2 inside an enhanced tube, in: Proc. 24th International Congress of Refrigeration, Yokohama, 2015, 910-917.

B. Dietrich, M. Wetzel, **S. Weise**, T. Wetzel. Strömungssieden von CO_2-Öl-Gemischen im glatten und innenstrukturierten Rohr, in Proc. Deutsche Kälte-Klima-Tagung, 2014.

Conference contributions

S. Weise, S. Klein, F. Müller-Trefzer, T. Wetzel, B. Dietrich (2019) Strömungssieden von CO_2 in offenporigen Strukturen - Strömungsform, Wärmeübergang und Druckverlust, ProcessNet-Fachgruppe Wärme- und Stoffübertragung, Essen, 18.-19. März 2019 (poster).

S. Weise, T. Wetzel, B. Dietrich (2018) Experimental investigation of two-phase flow boiling inside porous media, 16th International Heat Transfer Conference, Peking, 2018 (poster).

S. Weise, M. Wetzel, T. Wetzel, B. Dietrich (2018) Strömungssieden von CO_2 – Einfluss von Öl und porösen Strukturen auf Strömungsform, Wärmeübergang und Druckverlust, DKV-Kolloquium „CO_2 – aktuelle Beiträge aus Forschung und Industrie", Stuttgart, 17. April 2018 (talk).

S. Weise, T. Wetzel, B. Dietrich (2018) Strömungssieden von CO_2 in metallischen Schwämmen – Strömungsform, Wärmeübergang und Druckverlust, ProcessNet-Fachgruppe Wärme- und Stoffübertragung, Bremen, 6.-7. März 2018 (talk).

S. Weise, B. Dietrich, T. Wetzel (2017), Strömungssieden von CO_2 in porösen Systemen, Deutsche Kälte-Klimatagung, Bremen, 22.- 24. November 2017 (talk).

S. Weise, A. Matz, J. Heimann, S. Meinicke, N. Jost, T. Wetzel, B. Dietrich (2017) Generalized modelling and experimental validation of stagnant thermal conductivity of porous material, 9th International Conference on Porous Media & Annual Meeting, Rotterdam, 8.- 11. Mai 2017 (poster).

S. Weise, A. Matz, J. Heimann, S. Meinicke, N. Jost, T. Wetzel, B. Dietrich (2017) Experimental investigation of two-phase flow with phase change inside porous media, 9th International Conference on Porous Media & Annual Meeting, Rotterdam, 8.- 11. Mai 2017 (poster).

S. Weise, S. Meinicke, B. Dietrich (2016) Experimental and numerical investigations on conjugate heat transfer in open cellular structures, 4th Cellular Materials CellMAT, Dresden, 7.- 9. Dezember 2016 (talk).

S. Weise, M. Wetzel, B. Dietrich, T. Wetzel (2016) Druckverlust beim Strömungssieden von CO_2 - Einfluss von POE-Öl im horizontalen innenstrukturierten Rohr, Deutsche Kälte-Klimatagung, Kassel, 17.- 18. November 2016 (talk).

S. Weise, T. Wetzel, B. Dietrich (2016) Strömungssieden in metallischen Schwammstrukturen – Einflussfaktoren und Charakterisierung, ProcessNet-Fachgruppe Wärme- und Stoffübertragung, Kassel, 1.- 2. März 2016 (poster).

S. Weise, M. Wetzel, M. Hornberger, B. Dietrich, T. Wetzel (2015), Experimental Investigation of of the influence of lubricating oil on the flow boiling heat transfer and pressure drop of CO_2 inside an enhanced tube, 24th IIR International Congress of Refrigeration, Yokohama, 2015 (talk).

S. Weise, B. Dietrich, T. Wetzel (2015) Messstrecke zur Untersuchung des Wärmeübergangs und Druckverlusts beim Strömungssieden in festen Schwämmen, ProcessNet-Fachgruppe Wärme- und Stoffübertragung, Leipzig, 4.-6. März 2015 (poster).

B. Dietrich, M. Wetzel, **S. Weise**, T. Wetzel (2014) Strömungssieden von CO_2-Öl-Gemischen im glatten und innenstrukturierten Rohr, Deutsche Kälte-Klimatagung, Düsseldorf, 20.- 21. November 2014 (talk).

Reliable predictive models for heat transfer and pressure drop are required to evaluate the advantages of integrating porous structures into evaporator tubes. Consequently, the aim of this thesis was to verify or falsify the following hypothesis:

The heat transfer and pressure drop of flow boiling in a horizontal tube with porous inserts can be described by physically reasonable combination of established models from the fields of "single-phase flow" and "boiling in empty tubes" - without using fitting parameters.

Pressure drop and heat transfer tests with three different porous inserts were carried out using a newly designed test section. The hypothesis can be verified for the modeling of the adiabatic pressure drop at high mass fluxes, as well as for the modeling of the heat transfer coefficient in the investigated parameter range. Transferability to other porous structures, tube diameters, cooling media and operating conditions can be expected.